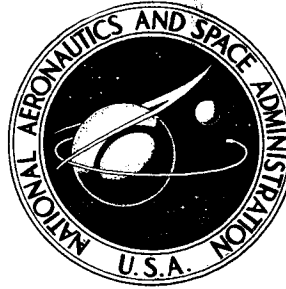


NASA CONTRACTOR REPORT



NASA CR-594

NASA CR-594

FACILITY FORM 602	N67 12098 (ACCESSION NUMBER)	(THRU)
	210 (PAGE)	1 (CODE)
	CR-594 (NASA CR OR TMX CR AD NUMBER)	21 (CATEGORY)

EVALUATION OF A SEMI-ACTIVE GRAVITY GRADIENT SYSTEM

VOLUME II: APPENDICES

by *P. C. Wheeler, R. G. Nishinaga,
J. G. Zaremba, and H. L. Williams*

ESTIMATED PRICE(S) \$ 3.75

HARD COPY (HC) 1.25

MICROFILME (MF)

HARD COPY OF

Prepared by
TRW SYSTEMS
Redondo Beach, Calif.
for Goddard Space Flight Center

EVALUATION OF A SEMI-ACTIVE GRAVITY GRADIENT SYSTEM

VOLUME II: APPENDICES

By P. C. Wheeler, R. G. Nishinaga, J. G. Zaremba,
and H. L. Williams

Distribution of this report is provided in the interest of information exchange. Responsibility for the contents resides in the author or organization that prepared it.

Prepared under Contract No. NAS 5-9640 by
TRW SYSTEMS
Redondo Beach, Calif.

for Goddard Space Flight Center

NATIONAL AERONAUTICS AND SPACE ADMINISTRATION

For sale by the Clearinghouse for Federal Scientific and Technical Information
Springfield, Virginia 22151 - Price \$3.75

TABLE OF CONTENTS

	<u>Page</u>
I. Acquisition Performance Evaluations	I-1
II. SAGS Acquisition Simulation	II-1
III. Reaction Wheel Control System Design Studies	III-1
IV. Roll/Yaw Fine Control Study	IV-1
V. Roll/Yaw Frequency Response Program	V-1
VI. SAGS Disturbance Torque Analyses	VI-1
VII. Implementation Evaluations	VII-1

LIST OF FIGURES

<u>Figure</u>		<u>Page</u>
I-1a	Roll/Yaw Acquisition with Baseline Parameters (89° initial roll error): a_{22} v. Orbits	I-9
I-1b	Roll/Yaw Acquisition with Baseline Parameters (89° initial roll error): ω_x v. Orbits	I-9
I-1c	Roll/Yaw Acquisition with Baseline Parameters (89° initial roll error): ω_y v. Orbits	I-10
I-1d	Roll/Yaw Acquisition with Baseline Parameters (89° initial roll error): ω_z v. Orbits	I-10
I-1e	Roll/Yaw Acquisition with Baseline Parameters (89° initial roll error): γ v. Orbits	I-11
I-2	Roll/Yaw Acquisition with Baseline Parameters (89° initial yaw error): a_{22} v. Orbits	I-11
I-3	Roll/Yaw Acquisition with Baseline Parameters (179° initial roll error): a_{22} v. Orbits	I-13
I-4	Roll/Yaw Acquisition with Gimbal Stop at 45°: a_{22} v. Orbits	I-14
I-5	Roll/Yaw Acquisition with Gimbal Stop at 20°: a_{22} v. Orbits	I-14
I-6	Roll/Yaw Acquisition with Twice Baseline Damping Coefficient (89° initial roll error): a_{22} v. Orbits	I-16
I-7	Roll/Yaw Acquisition with Ten Times Baseline Spring Constant (89° initial roll error): a_{22} v. Orbits	I-16
I-8	Roll/Yaw Acquisition with Zero Initial Angular Momentum (89° initial roll error): a_{22} v. Orbits	I-18
I-9	Conical Horizon Scanner Geometry	I-18
I-10	Conditioned Attitude Error Signal with "Sin θ " Processing	I-22
I-11	Conditioned Attitude Error Signal with "Sin2 θ " Processing	I-22
I-12	Conditioned Attitude Error Signal with Blanking at + 90°	I-23

LIST OF FIGURES (continued)

<u>Figure</u>		<u>Page</u>
I-13	Conditioned Attitude Error Signal with Blanking at $\pm(90 - \rho_0)$	I-23
I-14	Pitch Capture with "Sin 2 θ " Processing ($T_m = 5$ in-oz, $H_D = 1$ ft-lb-sec)	I-26
I-15	Pitch Capture with "Sin 2 θ " Processing ($T_m = 2$ in-oz, $H_D = 1$ ft-lb-sec)	I-27
I-16	Pitch Capture with Blanking at $\pm(90 - \rho_0)$ ($T_m = 5$ in-oz, $H_D = 1$ ft-lb-sec)	I-29
I-17	Turnover Maneuver with "Sin θ " Processing ($T_m = 5$ in-oz, $H_D = 1$ ft-lb-sec)	I-31
II-1	Reaction Wheel Control Law in SAGS Acquisition Simulation	II-7
II-2	Horizon Scanner Processing Logic	II-10
III-1	Reaction Wheel Control System	III-2
III-2	Pulse Ratio Modulator Mechanization	III-3
III-3	Static Wheel Speed Offsets due to Disturbance Torque and Windage	III-9
III-4	Attitude Error as a Function of Tachometer Gain	III-9
III-5	Momentum Storage Requirements as a Function of Tachometer Gain	III-11
III-6	Reaction Wheel Loop Characteristic Frequencies as a Function of Tachometer Gain	III-11
III-7	Transient Response of Baseline System	III-18
III-8	Effect of Lead-Lag Network upon Transient Response	III-18
III-9	Transient Response as a Function of Initial Reaction Wheel Momentum	III-20
III-10	Effect of Motor Windage Level upon Transient Response	III-20

LIST OF FIGURES (continued)

<u>Figure</u>		<u>Page</u>
III-11	Transient Response with Integral Tachometer Feedback	III-22
IV-1	Gimballed Reaction Wheel Configurations	IV-3
IV-2	Recommended Values of Spring Constant and Damping Coefficient (Orbital Attitude = 750 n. mi.)	IV-10
IV-3a	Roll Error/Roll Torque Gain (Roll-Yaw Gimbal Configuration): as a Function of Yaw Spring Constant	IV-14
IV-3b	Roll Error/Yaw Torque Gain (Roll-Yaw Gimbal Configuration): as a Function of Yaw Spring Constant	IV-14
IV-3c	Roll Error/Pitch Torque Gain (Roll-Yaw Gimbal Configuration): as a Function of Yaw Spring Constant	IV-15
IV-3d	Yaw Error/Pitch Torque Gain (Roll-Yaw Gimbal Configuration): as a Function of Yaw Spring Constant	IV-15
IV-3e	Yaw Error/Roll Torque Gain (Roll-Yaw Gimbal Configuration): as a Function of Yaw Spring Constant	IV-16
IV-3f	Yaw Error/Yaw Torque Gain (Roll-Yaw Gimbal Configuration): as a Function of Yaw Spring Constant	IV-16
IV-4a	Roll Error/Roll Torque Gain (Single Gimbal Configurations)	IV-18
IV-4b	Roll Error/Yaw Torque Gain (Single Gimbal Configurations)	IV-18
IV-4c	Roll Error/Pitch Torque Gain (Single Gimbal Configurations)	IV-19
IV-4d	Yaw Error/Pitch Torque Gain (Single Gimbal Configurations)	IV-19
IV-4e	Yaw Error/Roll Torque Gain (Single Gimbal Configurations)	IV-20

LIST OF FIGURES (continued)

<u>Figures</u>		<u>Page</u>
IV-4f	Yaw Error/Yaw Torque Gain (Single Gimbal Configurations)	IV-20
IV-5a	Roll Error/Roll Torque Gain (Roll Gimbal System): as a Function of Spring Constant	IV-21
IV-5b	Roll Error/Yaw Torque Gain (Roll Gimbal System): as a Function of Spring Constant	IV-21
IV-5c	Yaw Error/Roll Torque Gain (Roll Gimbal System): as a Function of Spring Constant	IV-22
IV-5d	Yaw Error/Yaw Torque Gain (Roll Gimbal System): as a Function of Spring Constant	IV-22
IV-5e	Gimbal Error/Roll Torque Gain (Roll Gimbal System): as a Function of Spring Constant	IV-23
IV-5f	Gimbal Error/Yaw Torque Gain (Roll Gimbal System): as a Function of Spring Constant	IV-23
IV-6a	Roll Error/Roll Torque Gain (Roll Gimbal System): as a Function of Damping Coefficient	IV-24
IV-6b	Roll Error/Yaw Torque Gain (Roll Gimbal System): as a Function of Damping Coefficient	IV-24
IV-6c	Yaw Error/Roll Torque Gain (Roll Gimbal System): as a Function of Damping Coefficient	IV-25
IV-6d	Yaw Error/Yaw Torque Gain (Roll Gimbal System): as a Function of Damping Coefficient	IV-25
IV-6e	Gimbal Error/Roll Torque Gain (Roll Gimbal System): as a Function of Damping Coefficient	IV-26
IV-6f	Gimbal Error/Yaw Torque Gain (Roll Gimbal System): as a Function of Damping Coefficient	IV-26
IV-7a	Roll Error/Roll Torque Gain (Roll Gimbal System): as a Function of Wheel Momentum	IV-27
IV-7b	Roll Error/Yaw Torque Gain (Roll Gimbal System): as a Function of Wheel Momentum	IV-27
IV-7c	Yaw Error/Roll Torque Gain (Roll Gimbal System): as a Function of Wheel Momentum	IV-28

LIST OF FIGURES (continued)

<u>Figures</u>		<u>Page</u>
IV-7d	Yaw Error/Yaw Torque Gain (Roll Gimbal System): as a Function of Wheel Momentum	IV-28
IV-7e	Gimbal Error/Roll Torque Gain (Roll Gimbal System): as a Function of Wheel Momentum	IV-29
IV-7f	Gimbal Error/Yaw Torque Gain (Roll Gimbal System): as a Function of Wheel Momentum	IV-29
IV-8	RSS Roll Torque Versus Frequency (Case I: Sun in Orbit Plane)	IV-33
IV-9	RSS Pitch Torque Versus Frequency (Case I: Sun in Orbit Plane)	IV-33
IV-10	RSS Yaw Torque Versus Frequency (Case I: Sun in Orbit Plane)	IV-34
IV-11	RSS Roll Torque Versus Frequency (Case II: Sun Normal to Orbit Plane)	IV-34
IV-12	RSS Pitch Torque Versus Frequency (Case II: Sun Normal to Orbit Plane)	IV-35
IV-13	RSS Yaw Torque Versus Frequency (Case II: Sun Normal to Orbit Plane)	IV-35
IV-14	RSS Torque Due to Control Axis Misalignments and Orbital Eccentricity (Case I: Sun in Orbit Plane)	IV-37
IV-15	RSS Torque Due to Control Axis Misalignments and Orbital Eccentricity (Case II: Sun Normal to Orbit Plane)	IV-37
V-1	Computer Flow Diagram	V-11
VI-1	Spacecraft Dimensions	VI-2
VI-2	Spacecraft Mass Distribution	VI-3
VI-3	Coordinate Frames	VI-3

LIST OF FIGURES (continued)

<u>Figures</u>		<u>Page</u>
VII-1	Conceptual View of SAGS Controller	VII-2
VII-2	Controller Design with Hysteresis Damper and Case-Mounted Bolometer	VII-6
VII-3	Controller Design with Eddy Current Damper and Wheel-Mounted Bolometer	VII-7
VII-4	Suspension System	VII-14
VII-5	Conceptual View of Hysteresis Damper	VII-23
VII-6	Eddy Current Damper Weight as a Function of Damping Coefficient	VII-23
VII-7	Field-of-View Geometry	VII-32
VII-8	Signal Processing and Control Electronics	VII-35

LIST OF TABLES

<u>Table</u>		<u>Page</u>
I-1	Baseline Roll/Yaw Acquisition Parameters	I-8
I-2	Summary of Representative Roll/Yaw Acquisition Runs	I-19
III-1	Baseline Parameter Values for Analog Study	III-16
III-2	Steady-State Performance	III-19
IV-1	Roll/Yaw Gain Expressions at Zero Frequency	IV-6
IV-2	Roll/Yaw Gain Expressions at Orbital Frequency	IV-7
IV-3	Steady-State Roll/Yaw Errors	IV-39
IV-4	Effect Upon Roll/Yaw Performance of Representative System Changes	IV-41
VI-1	SAGS System Constants	VI-4
VI-2	Summary of Solar Pressure Torques	VI-14
VI-3	Summary of Thermal Boom Bending Torques	VI-18
VI-4	Summary of Magnetic Torque (Sun in Orbit Plane)	VI-24
VI-5	Summary of Magnetic Torque (Sun Normal to Orbit Plane)	VI-25
VI-6	Summary of Torques Due to Control Axes/ Principal Axes Misalignment	VI-28
VI-7	Summary of Torques Due to Orbital Eccentricity	VI-29
VII-1	Summary of Controller Performance Characteristics	VII-8
VII-2	Reaction Wheel Motor Characteristics	VII-10
VII-3	Summary of Wire Flexure Analysis	VII-16
VII-4	Wire and Blade Comparison	VII-21
VII-5	Summary of Damper System Analysis	VII-25

APPENDIX I

ACQUISITION PERFORMANCE STUDIES

A. INTRODUCTION

Acquisition, the attainment of the nominal spacecraft attitude orientation following orbital injection, consists (for the SAGS control configuration) of three phases:

- (i) Rate Damping - during which the initial angular velocities following injection are removed.
- (ii) Roll/Yaw Acquisition - during which the pitch axis is aligned normal to the orbit plane.
- (iii) Pitch Acquisition - during which the yaw axis of the spacecraft is aligned with the local vertical.

The rate damping phase commences when the spacecraft separates from the final injection stage. The precise character of this mode of operation will depend upon the nature of the injection; if the vehicle is injected by a spinning stage one of the several of the available despin mechanisms for spinning vehicles may be used, while if the injection stage is fully stabilized, the rate removal mechanism (if one is required) may consist of three rate gyros and a low-capacity three-axis pneumatic system. In either case, when, following rate damping, the solar array and the inertia mast are deployed, the angular velocities of the vehicle should be less than orbit rate.

Roll/yaw acquisition will begin when the reaction wheel bias is initiated. This may be prior to the rate damping phase or at its conclusion; however, in the former case roll/yaw acquisition will not be particularly effective until the attainment of small rates following deployment. Under the influence of the wheel-induced gyroscopic effects and of gravity-gradient torques, the total angular momentum of the system will eventually be aligned normal to the orbit plane, and the wheel axis and the pitch spacecraft axis will be aligned with the momentum vector. At the conclusion of roll/yaw acquisition, only a decoupled pitch motion will persist.

Pitch acquisition will be initiated when the roll/yaw motion has been removed, thus assuring that the horizon scanner is giving valid pitch error indications. Removal of the residual pitch motion will be accomplished by cycling the reaction wheel speed alternately between its upper and lower limits at a frequency of two cycles per revolution, in response to the horizon scanner output. The motion can terminate with the yaw axis either toward the earth or away from it; in the latter case a turnover maneuver must be executed, again by cycling the reaction wheel (either automatically or by ground command).

Although the rate removal phase has been considered during the present study (Reference 1), the terminal acquisition phases have received primary emphasis, since they alone are unique to the SAGS control configuration. These investigations are reported below.

B. ROLL/YAW ACQUISITION STUDIES

Roll/yaw acquisition has been approached both analytically and via simulation. Unfortunately, the former attack has been singularly unrewarding.

For analytical purposes a first step is to consider the vehicle as a rigid body containing a rigidly attached, constant-speed rotor but with no specific dissipation mechanism. This problem has been treated in the literature, but with several important restrictions; specifically, authors have either assumed that the wheel axis corresponds to a vehicle axis of inertial symmetry (which results in an invariant component of angular momentum and conclusions similar to those concerning the libration of a symmetric spinning satellite) as in Reference I-1 or they have concerned themselves with small excursions of the rotor axis from the orbital momentum vector (resulting in linear periodic equations, which may be treated by Floquet theory - see Reference I-2). Unfortunately, neither approach is applicable to the present study, the former because the rotor axis is normal to what is (essentially) the axis of inertial symmetry, and the latter because it does not face the basic issue of locating all possible stationary motions. An analytical demonstration of the transition from tumbling to pure pitch rotation about the orbital momentum vector is clearly a formidable task for the SAGS configuration.

Simulator studies of roll/yaw acquisition, utilizing the digital simulation described in Appendix II, have been productive. In this case consideration has been limited to the single (roll) gimbal configuration (preferable for small error control and also from a

mechanization standpoint) with a proportional damper; furthermore, the effect of energy dissipation in the boom has been neglected (a pessimistic omission) and only the case in which the wheel speed is constant during roll/yaw acquisition was considered. Notwithstanding these simplifications, this simulation has given a strong indication of the feasibility of acquisition with the SAGS control configuration and, furthermore, has shown that the parameter values selected for fine-control will yield very acceptable acquisition performance.

1. Equations of Motion

The roll/yaw acquisition equations are derived in Appendix II. In the case of a constant wheel speed the dynamic equations become

$$\begin{aligned}
 I_x \dot{\omega}_x + (I_z - I_y) \omega_y \omega_z &= 3\omega_o^2 (I_z - I_y) a_{23} a_{33} - H_c (\omega_y \sin\gamma - \omega_z \cos\gamma) \\
 I_y \dot{\omega}_y + (I_x - I_z) \omega_x \omega_z &= 3\omega_o^2 (I_x - I_z) a_{13} a_{33} - H_c (\dot{\gamma} + \omega_x) \sin\gamma \\
 I_z \dot{\omega}_z + (I_y - I_x) \omega_x \omega_y &= 3\omega_o^2 (I_y - I_x) a_{13} a_{23} - H_c (\dot{\gamma} + \omega_x) \cos\gamma \\
 c \dot{\gamma} + f(\gamma) + H_c (\omega_y \sin\gamma - \omega_z \cos\gamma) &= 0
 \end{aligned} \tag{I.1}$$

where γ is the gimbal angle, ω_o is the orbit rate, and H_c is the pitch wheel momentum ($H_c < 0$). The attitude of the vehicle relative to the rotating (x_r, y_r, z_r) orbital reference frame is defined by the direction cosine matrix A, with elements a_{ij} . In particular, a_{13} , a_{23} and a_{33} represent the projections of the local vertical upon the roll, pitch and yaw axis, respectively. The kinematical equations describing the variation of A are stated (in terms of Euler parameters) in Appendix II. It is important to note that

the a_{ij} can vary even when $\omega_x = \omega_y = \omega_z = 0$, since the direction cosine matrix is defined relative to a reference frame which is itself rotating in inertial space at orbital rate.

A discussion of the singular (equilibrium) conditions for these equations was presented in the First Quarterly Report (Reference 1) with pitch control considered. It was shown that only one equilibrium orientation relative to the (x_r, y_r, z_r) frame could be stable - that is, the one with A, an identity matrix. This demonstration was equivalent to formulating the dynamic potential function (Ref. I-3)*

$$\begin{aligned}
 V = & \frac{3}{2} \omega_o^2 [(I_y - I_z) a_{23}^2 + (I_x - I_z) a_{13}^2] + \int_0^\gamma f(x) dx \\
 & - \frac{1}{2} \omega_o^2 (I_x a_{12}^2 + I_y a_{22}^2 + I_z a_{32}^2) \\
 & - \frac{1}{2} J_w [\Omega - \omega_o (a_{22} \cos \gamma + a_{32} \sin \gamma)]^2 \quad (I.2)
 \end{aligned}$$

and showing that the only singular point relative to which this function is positive-definite corresponds to $A = I$, for the inertia distribution in question (in this instance $I_x = I_y \gg I_z$) and an appropriate pitch control law (i.e., one which makes the "upside-down" orientation unstable). Consider, for example, small perturbations ϕ , θ and ψ from the equilibria with $a_{33} = 1$, and (i) $a_{22} = +1$ and (ii) $a_{22} = -1$. Then, with $f(\gamma) = k \gamma$, V can be written as:

* Ω = wheel speed relative to the spacecraft; J_w = wheel moment of inertia. Note that Ω is negative.

$$v = [\phi \ r \ \psi \ \theta] \begin{bmatrix} \beta_{11} & \beta_{12} & 0 & 0 \\ \beta_{12} & \beta_{22} & 0 & 0 \\ 0 & 0 & \beta_{33} & 0 \\ 0 & 0 & 0 & \beta_{44} \end{bmatrix} \begin{bmatrix} \phi \\ r \\ \psi \\ \theta \end{bmatrix} \quad (\text{I.3})$$

where

$$\beta_{11} = 4\omega_o^2 (I_y - I_z) - \omega_o H_c u$$

$$\beta_{12} = -\omega_o H_c u$$

$$\beta_{22} = k - \omega_o H_c u$$

$$\beta_{33} = \omega_o^2 (I_y - I_x) - \omega_o H_c u$$

$$\beta_{44} = 3\omega_o^2 (I_x - I_z)$$

and $u = +1$ for equilibrium (i), $u = -1$ for equilibrium (ii). In the foregoing $|\Omega| \gg \omega_o$ is assumed. In order for V to be positive-definite, the Sylvester inequalities (Ref. I-4) must be satisfied. This yields the following stability conditions:

$$\begin{aligned} 4\omega_o^2 (I_y - I_z) - \omega_o H_c u &> 0 \\ 4\omega_o^2 (I_y - I_z) k - \omega_o H_c u [k + 4\omega_o^2 (I_y - I_z)] &> 0 \\ \omega_o^2 (I_y - I_x) - \omega_o H_c u &> 0 \\ 3\omega_o^2 (I_x - I_z) &> 0 \end{aligned} \quad (\text{I.4})$$

It is clear that (with $I_x = I_y$) $H_c u < 0$ must be insured so that, with H_c negative, $u = 1$ defines a stable equilibrium ($a_{22} = +1$) while the equilibrium $u = -1$ ($a_{22} = -1$) is unstable.

There is another type of singular condition which, while of no practical significance, is worth mentioning. This occurs when the angular rates of the body relative to inertial space ($\omega_x, \omega_y, \omega_z$) are all zero, with the gimbal undeflected, and with the z_r axis (local vertical) in the pitch-roll plane of the vehicle. Under these circumstances, if the pitch and roll inertias are identically equal, there will be neither gravitational nor gyroscopic torques on the spacecraft, and its attitude will remain fixed in inertial space. However, this case is of academic interest only, because I_x and I_y will never be identically equal, nor will the angular velocities be exactly zero.

2. Simulation Results

A number of runs were made to study roll/yaw acquisition performance; a representative set of these is presented here.

As a basic ground rule, only parameter values found to be reasonable for both fine control and mechanization were considered. In addition, an effective rate damping phase was assumed so that the initial rates were set equal to zero (except in a few cases). These restrictions were necessary in order to impose a reasonable limit upon the number of runs.

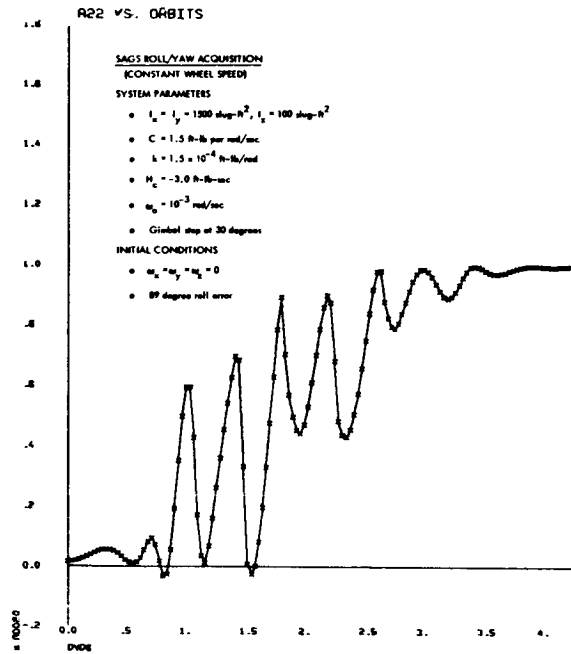
The parameter values of Table I.1 were used as the baseline system. The normalized version of these parameters is included

because, as is shown in Appendix II, the acquisition equations are amenable to normalization in terms of ω_o and I_y . This means that having obtained results for one particular orbit rate and pitch inertia combination, these results (notably, the number of orbits required to converge) can be extended to any other situation in which the normalized system parameters are the same; the results, then, are of general significance and not limited to the specific numerical case presently considered.

Parameter	Baseline Value	
	Normalized	Numerical
ω_o (rad/sec)	ω_o	0.001
I_y (slug-ft ²)	I_y	1500.
I_x (slug-ft ²)	I_y	1500.
I_z (slug-ft ²)	$.067 I_y$	100.
H_c (ft-lb-sec)	$- 2\omega_o I_y$	-3.0
c (ft-lb per rad/sec)	$\omega_o I_y$	1.5
k (ft-lb/rad)	$0.1 \omega_o^2 I_y$	1.5×10^{-4}
γ_s (deg)	--	30°

Table I-1 Baseline Roll/Yaw Acquisition Parameters

Figure I-1 shows the acquisition response of the baseline system for zero initial angular velocities and an initial roll error of 89° (singular cases such as 90 or 180 degree initial errors were avoided unless initial roll/yaw rates were present).



• Figure I-1a Roll/Yaw Acquisition with Baseline Parameters (89° initial roll error): a_{22} v. Orbits

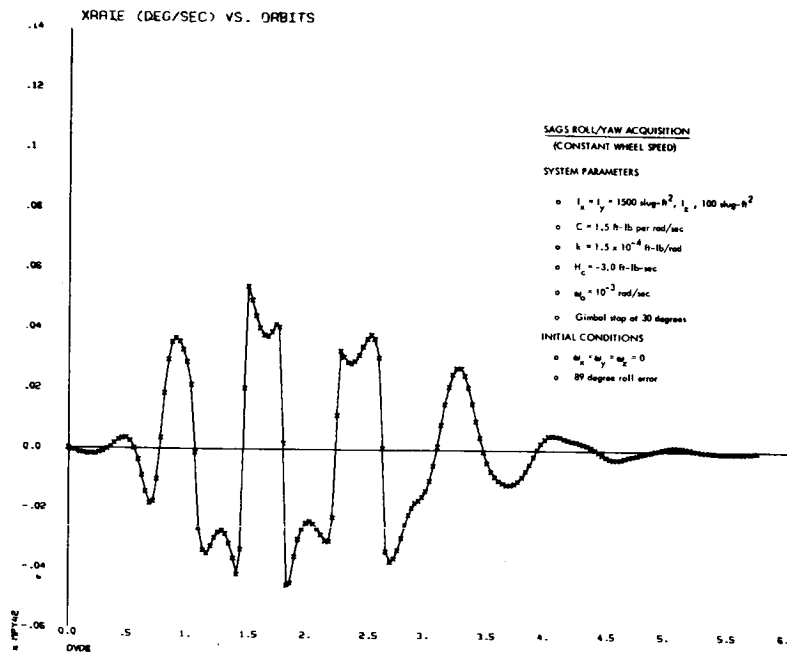


Figure I-1b Roll/Yaw Acquisition with Baseline Parameters (89° initial roll error): ω_x v. Orbits

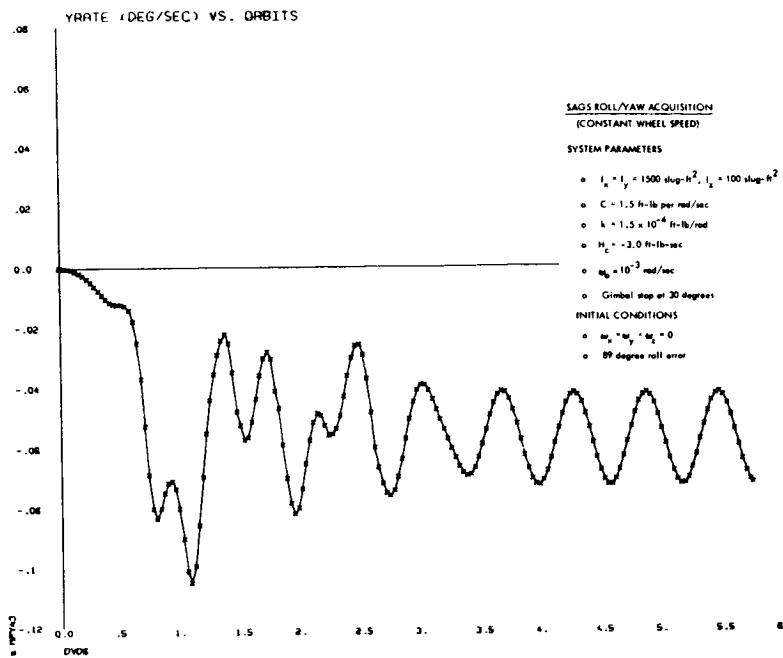


Figure I-1c Roll/Yaw Acquisition with Baseline Parameters (89° initial roll error): ω_y v. Orbits

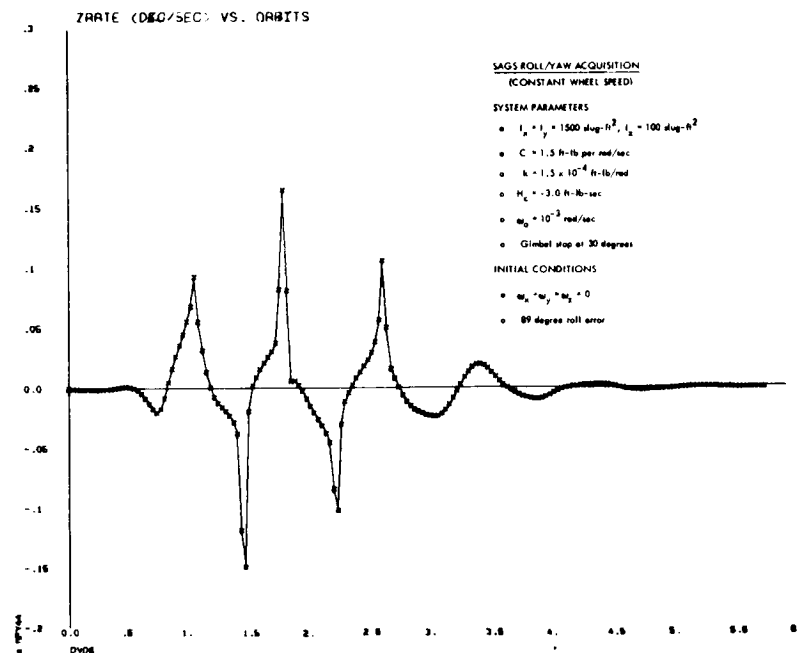


Figure I-1d Roll/Yaw Acquisition with Baseline Parameters (89° initial roll error): ω_z v. Orbits

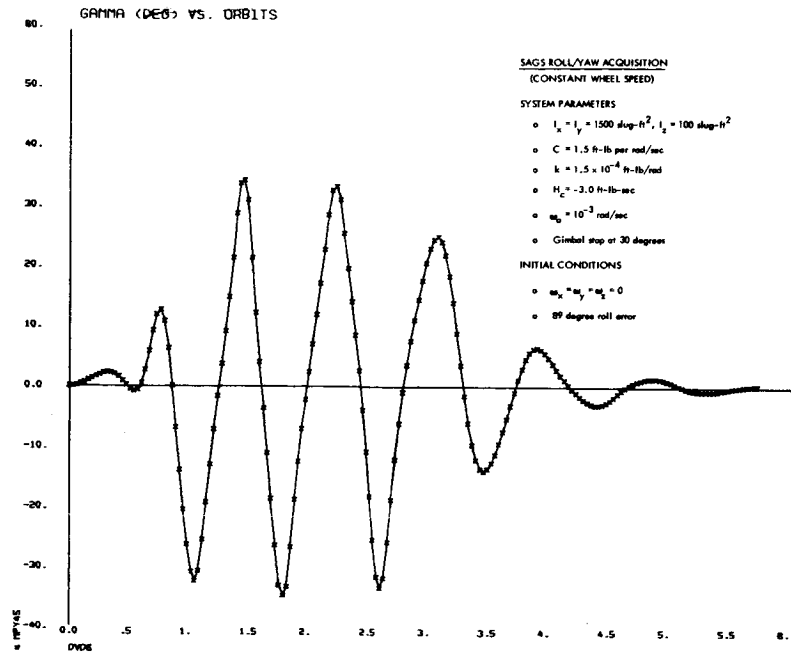


Figure I-1e Roll/Yaw Acquisition with Baseline Parameters (89° initial roll error): γ v. Orbits

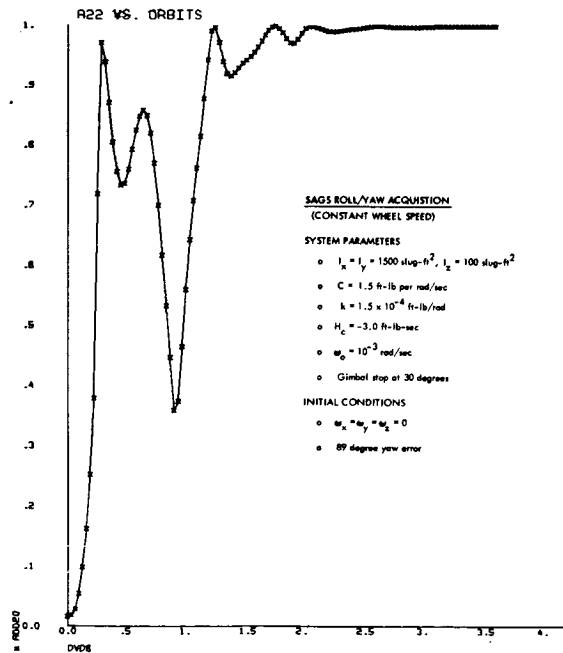


Figure I-2 Roll/Yaw Acquisition with Baseline Parameters (89° initial yaw error): a_{22} v. Orbits

The time to acquire, here defined as that time necessary to make a_{22} permanently greater than 0.95, is 3.3 orbits. The motion terminates in bounded pitch oscillations, as indicated by the terminal motion of ω_y (which is oscillating about its nominal value of $-\omega_0$); in this case, the terminal oscillation was in the "upside-down" condition, requiring a turnover maneuver. Notice that the gimbals did reach the stop angle γ_s (motion in excess of this value occurs because a soft stop is employed).

Figures I-2 and I-3 represent additional runs with the baseline system. The latter case is particularly interesting in that it demonstrates acquisition from a nearly "upside-down" initial attitude. Acquisition ($a_{22} > .95$) required approximately 7.9 orbits, making this the longest observed acquisition. This longer than usual convergence time can be related to the behavior during the fifth revolution when a_{22} hovered near unity. The motion during this period was nearly periodic with the gimbals oscillating against the stop and the inertial pitch rate near zero. However, owing to a steady secular term in ω_y this motion did not persist and the roll/yaw acquisition terminated in "right-side-up" pitch oscillations.

It is apparent that the gimbals stops contributed significantly to the unique behavior observed in Figure I-3. The data presented in Figures I-4 and I-5 shows the effect of altering the gimbals stop, γ_s .* In the first case, the stops were placed at 45° and, in the latter case, γ_s was 20° . During both solutions the gimbals

*In these two runs $I_x = I_y = 1000 \text{ slug-ft}^2$. The normalized values of the system parameters are the same as those of the baseline system. In these runs $\omega_x(0) = \omega_0$ and there is a 90° initial roll error.

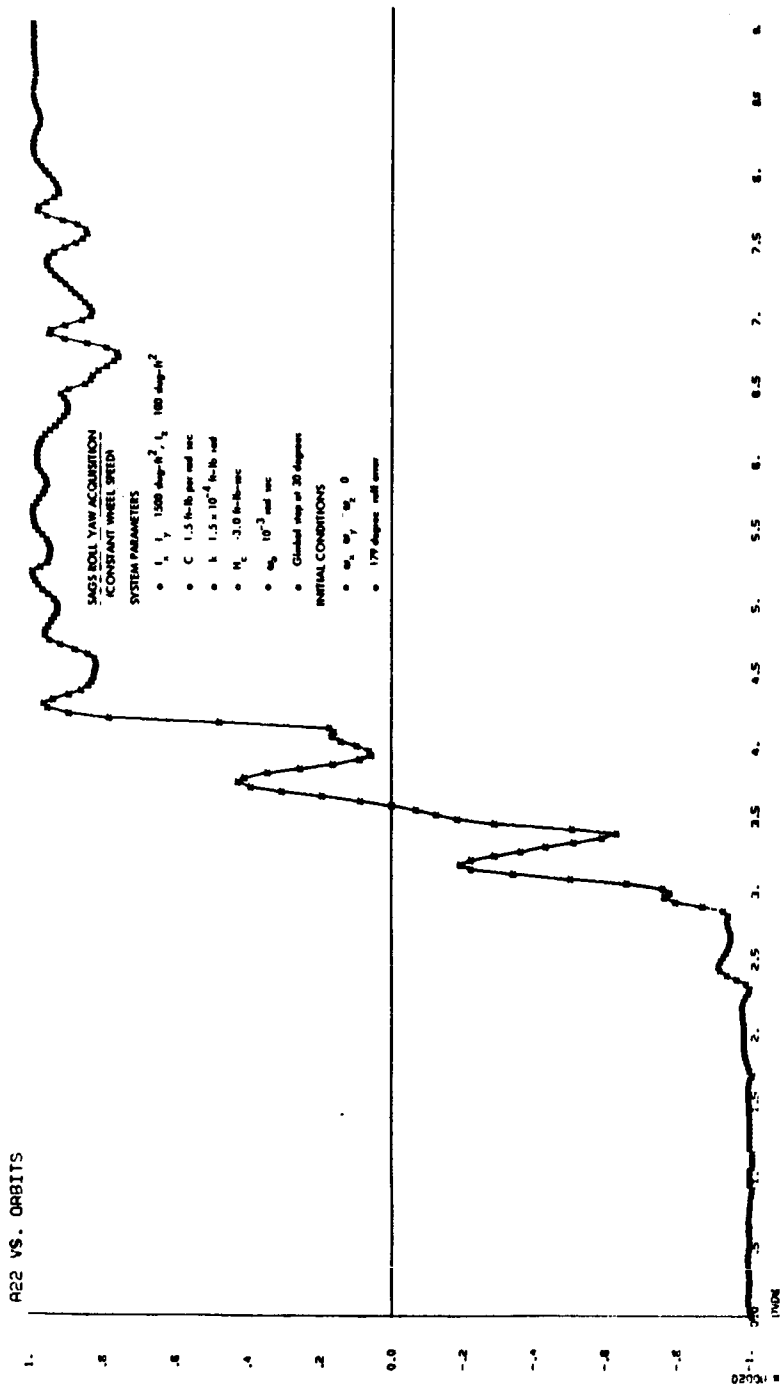


Figure I-3 Roll/Yaw Acquisition with Baseline
Parameters (179° initial roll error):
8-22 V. Orbits

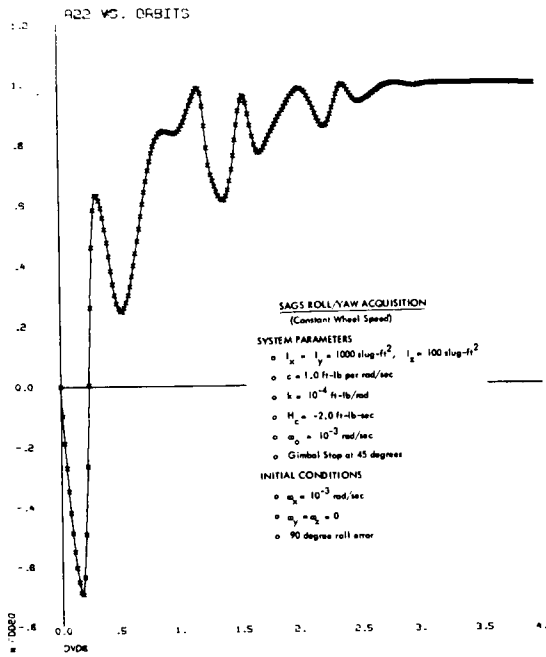


Figure I-4 Roll/Yaw Acquisition with Gimbal Stop at 45° : a_{22} v. Orbits

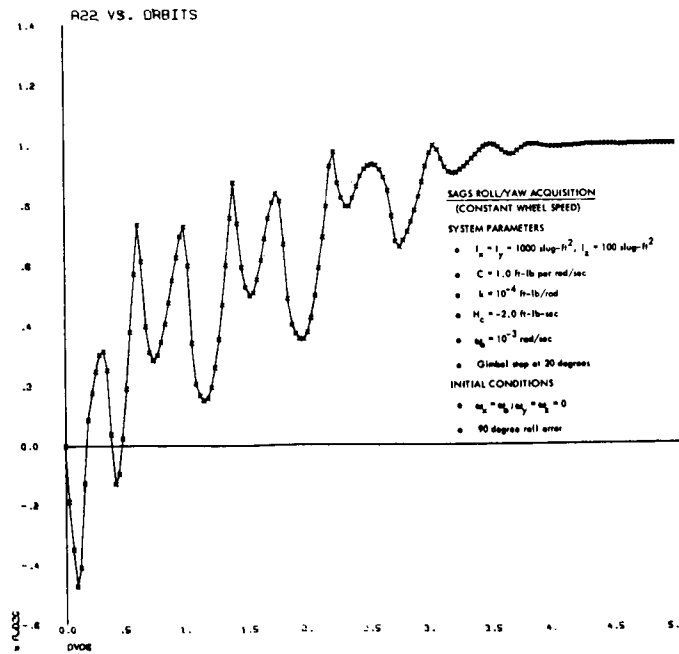


Figure I-5 Roll/Yaw Acquisition with Gimbal Stop at 20° : a_{22} v. Orbits

did hit its stops; however, the effect of the more severe restriction upon the gimbal motion was relatively slight, increasing the acquisition time from 2.5 to 3.4 revolutions. Lessening the allowed deflections did have a considerable effect upon the qualitative character of the motion as may be seen by noticing the increased oscillation frequency in Figure I-5.

The degree of damping in the gimbals can have a significant influence upon the time required for acquisition. Figure I-6 shows the effect upon the baseline system of doubling the damping coefficient, c (this run is directly comparable with Figure I-1). Acquisition requires 3.3 revolutions, essentially equivalent to the baseline case. In contrast, reducing the damping to one-half the nominal value resulted in a convergence time of 5.0 revolutions and a motion which was considerably more oscillatory. Although a detailed initial condition search was not performed, it is clear that the baseline damping value is a reasonable choice. Lower values yield poorer performance and larger damping levels will result in a heavier mechanism.

The effect of a stiffer spring is, at least up to a point, not critical, as is shown in Figure I-7 where the spring constant is an order of magnitude larger than its nominal value. Although the motion is somewhat more oscillatory than in Figure I-1, the convergence time (4 orbits) is still reasonable. This result parallels the relative insensitivity to spring stiffness observed for fine control.

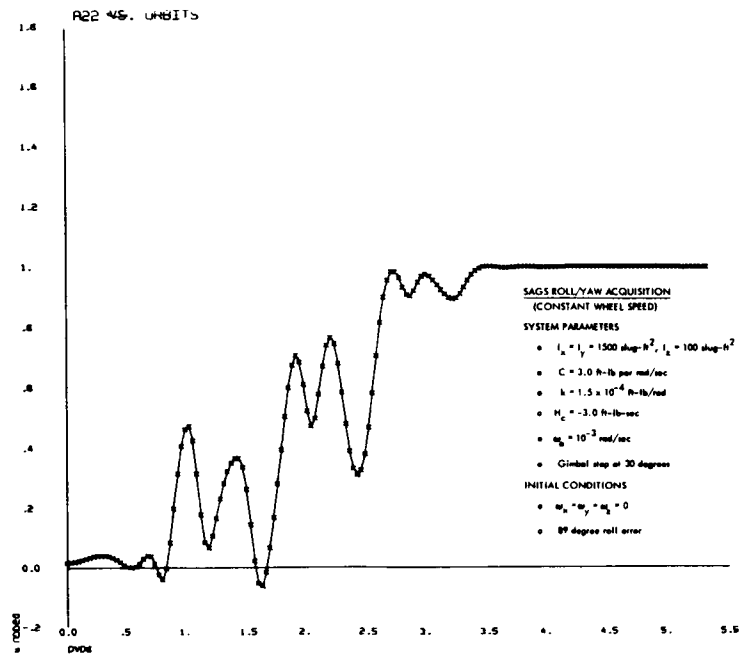


Figure I-6 Roll/Yaw Acquisition with Twice Baseline Damping Coefficient (89° initial roll error): a_{22} v. Orbits

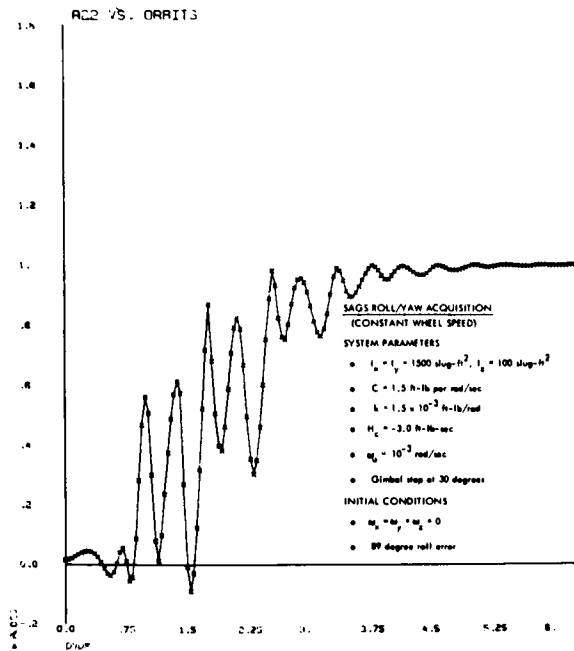


Figure I-7 Roll/Yaw Acquisition with Ten Times Baseline Spring Constant (89° initial roll error): a_{22} v. Orbits

In each of the above cases the total initial momentum of the system was H_c (the wheel momentum) corresponding to the case in which the wheel is activated (i.e., its speed control loop only) prior to the rate damping phase. If the wheel were spun-up following rate removal and rod deployment, the net initial momentum of the system would be zero and it might seem that the acquisition problem would be alleviated. Such is not the case, as shown in Figure I-8, a run equivalent to Figure I-1, except that the initial spacecraft momentum was made equal to zero by an appropriate choice of the initial pitch rate. Although too limited to be conclusive, these results indicate that there is nothing to be gained by delaying wheel run-up until after deployment.

Several cases were examined with non-nominal values of wheel momentum; however, no clear trend appeared. Because the choice of H_c is established primarily by fine control requirements, the important question (here answered in the affirmative) is whether the fine control values of H_c provide acceptable acquisition performance.

The computer runs presented here are summarized in Table I-2.

C. PITCH ACQUISITION

Following the completion of roll/yaw acquisition, the spacecraft will be either tumbling or oscillating about the pitch axis; in the former case the primary pitch acquisition requirement is the conversion of the tumbling motion to an oscillatory motion. Pitch acquisition can be accomplished by cycling the reaction wheel between its minimum and maximum allowed speed in response to the

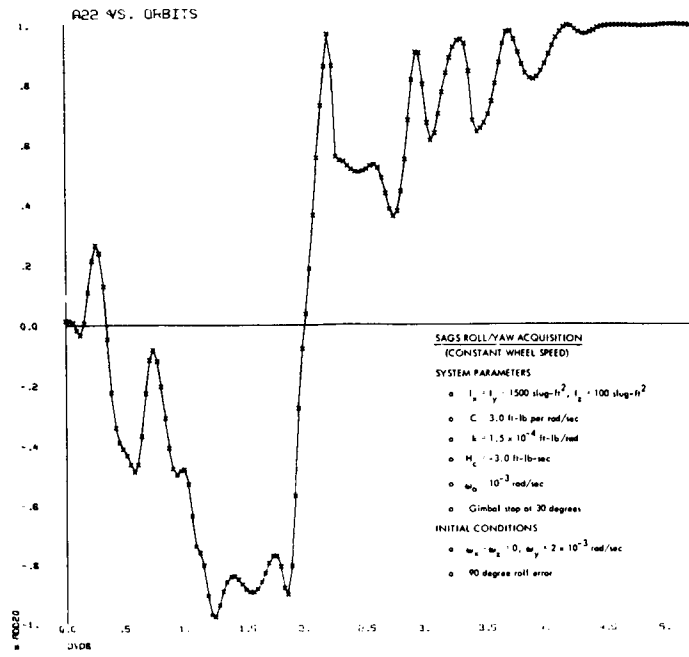


Figure I-8 Roll/Yaw Acquisition with Zero Initial Angular Momentum (89° initial roll error): a_{22} v. Orbits

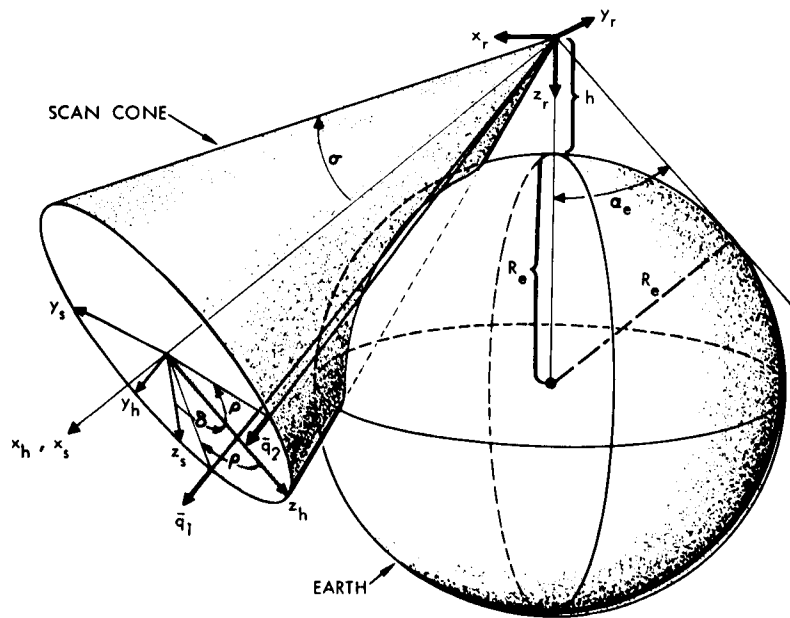


Figure I-9 Conical Horizon Scanner Geometry

Run No.	Fig.	Convergence Time ($a_{22} > 0.95$)	Terminal Pitch Motion*	Remarks
1	I-1	3.3 revs.	Bounded pitch oscillations ($a_{33} < 0$)	Baseline parameter values; 89° initial roll error.
2	I-2	1.5 revs.	Bounded pitch oscillations ($a_{33} > 0$)	Baseline parameter values; 89° initial yaw error.
3	I-3	7.9 revs.	Bounded pitch oscillations ($a_{33} > 0$)	Baseline parameter values; 179° initial roll error.
4	I-4	2.5 revs.	Bounded pitch oscillations ($a_{33} < 0$)	Gimbal stop at 45°; compare with Run 5
5	I-5	3.4 revs.	Bounded pitch oscillations ($a_{33} > 0$)	Gimbal stop at 20°; compare with Run 4
6	I-6	3.3 revs.	Bounded pitch oscillations ($a_{33} < 0$)	Effect of twice baseline damping; compare with Runs 1 and 7
7	---	5.0 revs.	Bounded pitch oscillations ($a_{33} < 0$)	Effect of one-half baseline damping; compare with Runs 1 and 6
8	I-7	4.0 revs.	Bounded pitch oscillations ($a_{33} < 0$)	Effect of 10 times baseline spring constant; compare with Run 1.
9	I-8	4.1 revs.	Bounded pitch oscillations ($a_{33} < 0$)	Effect of zero net initial angular momentum; compare with Run 1.

** $a_{33} < 0$ indicates "upside-down" pitch attitude

Table I-2 Summary of Representative Roll/Yaw Acquisition Runs

processed horizon scanner output. The rapidity with which pitch acquisition will be accomplished depends upon such factors as the motor torque level, the allowable speed range of the motor, and the manner in which the horizon scanner information is processed.

1. Horizon Scanner Signal Processing

The horizon scanner processing scheme selected can have a considerable influence upon pitch acquisition. Before discussing several of the processing alternatives, it is well to review the operation of the scanner, as described in the SAGS First Quarterly Report (Reference 1).

Figure I-9 illustrates the geometry associated with a conical horizon scanner (the type considered in this study). During each scan cycle the scanner line-of-sight sweeps out the indicated scan cone. Depending upon the orientation of the scan cone relative to the (x_p, y_p, z_p) geocentric coordinate frame, the cone may (or may not) intersect the earth. In the event that it does, an output pulse of width 2ρ will be generated. The location of this pulse on the scan cone is defined relative to the vertical reference axis, z_s , by the angle δ ; this angle is a measure of scan cone rotation about the x_s axis.* For purposes of signal processing additional auxiliary markers can be generated electronically; using these markers together with the vertical reference marker, various processing alternatives can be mechanized.

*Because pitch attitude errors are to be measured by the SAGS scanner, the x_s axis will coincide to the pitch axis and the z_s axis will be aligned with the yaw spacecraft axis (with the gimbal undeflected).

Consider first the case in which the scan cone is unblanked (i.e., the scanner is sensitive to earth pulses occurring in any portion of the scan cone), and assume that the vertical reference marker and three auxiliary markers partition the scan cone into four equal quadrants. Two processing techniques are immediately apparent:

- (i) sin θ processing for which the outputs of quadrants 1 and 2 are subtracted from those of quadrants 3 and 4.
- (ii) sin 2θ processing for which the outputs of quadrants 1 and 3 are subtracted from those of quadrants 2 and 4.

Figures I-10 and I-11 show the resulting error signals (where the roll and yaw attitude errors and the gimbal deflection have been assumed equal to zero).

These processing methods require that no part of the scan cone intersects any part of the vehicle; very often this is not the case, and portions of the scan cone must be electronically "blanked" (i.e., assumed to have zero output during processing). Figure I-12 is the result of omitting quadrants 2 and 3 from consideration in either of the above processing schemes. Figure I-13 shows the effect of blanking all but that portion of the cone lying within $90-\rho_0$ degrees of the vertical reference axis (where ρ_0 is the constant half-width of the earth pulse for pure pitch motion).* In the latter instance the required field of view is less than 100 degrees.

*In the cases shown here, $\rho_0 = 41.5^\circ$, corresponding to an orbital altitude of 750 nautical miles and a scan cone angle (σ) of 50 degrees.

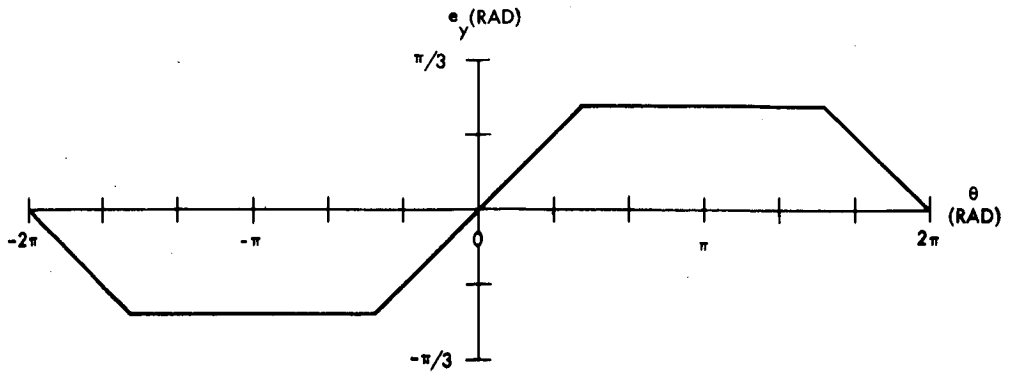


Figure I-10 Conditioned Attitude Error Signal with "Sin θ " Processing

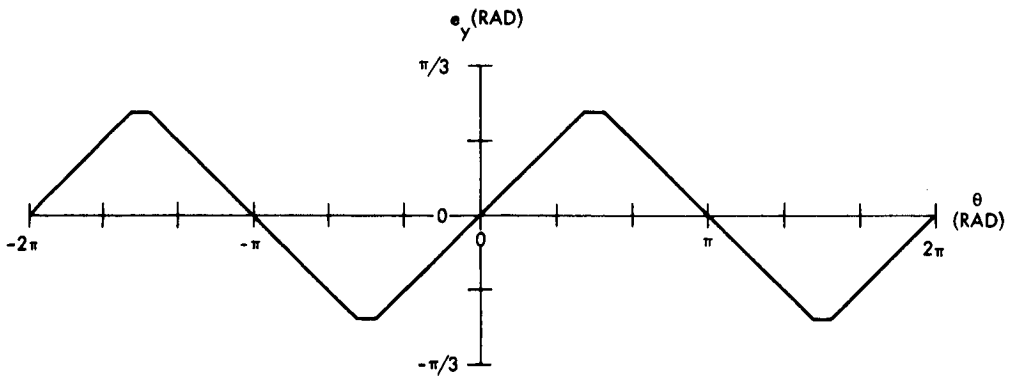


Figure I-11 Conditioned Attitude Error Signal with "Sin 2θ " Processing

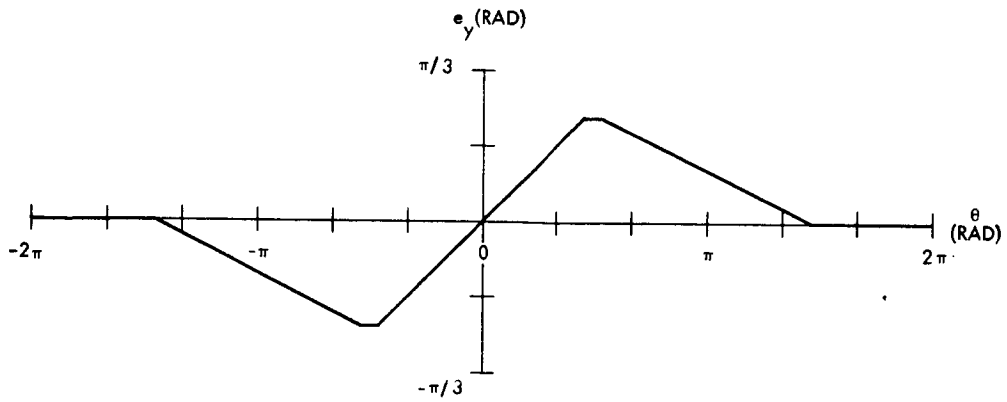


Figure I-12 Conditioned Attitude Error Signal with Blanking at $\pm 90^\circ$

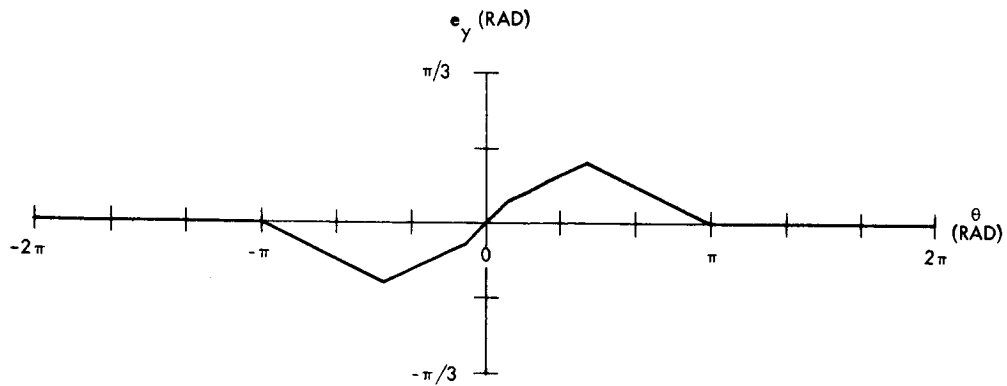


Figure I-13 Conditioned Attitude Error Signal with Blanking at $\pm(90 - \rho_0)$

It is apparent from examining Figures I-10 through I-13 that any of these processing techniques will yield equivalent small-error pitch performance. Clearly, the primary factors to be considered in selecting the method to be used are: (i) whether blanking is necessitated by the vehicle geometry, and (ii) pitch acquisition performance.

2. Pitch Acquisition Analysis

The motion of the spacecraft during pitch acquisition is described by

$$I_y \ddot{\theta} + \frac{3}{2} \omega_o^2 (I_x - I_y) \sin 2\theta = - \dot{H}_c \quad (I.5)$$

where a circular orbit is assumed and disturbance torques are neglected. The fact that the wheel speed must be biased (for both roll/yaw control and horizon scanning) means that the wheel momentum (H_c) will be restricted by a speed control loop to lie within a range given by

$$H_B - H_D \leq H_c \leq H_B + H_D \quad (I.6)$$

The usable momentum range is $2H_D$, while H_B is the nominal bias momentum.

The pitch control loop includes a pulse modulator with a small deadband (approximately one degree) and tachometer feedback (biased) for damping and wheel speed limiting. For purposes of evaluating pitch capture the tachometer loop can be neglected and on-off operation of the motor can be assumed. Then:

$$\dot{H}_c = \begin{cases} T_m, e_y > 0 \text{ and } H_c - H_B < H_D \\ 0, e_y > 0 \text{ and } H_c - H_B \geq H_D \\ 0, e_y = 0 \\ 0, e_y < 0 \text{ and } H_c - H_B \leq -H_D \\ -T_m, e_y < 0 \text{ and } H_c - H_B > -H_D \end{cases} \quad (\text{I.7})$$

Thus whenever e_y goes through zero a torque pulse will be generated and will persist until the wheel speed reaches its opposite limit.

Figure I-14 shows the pitch motion during acquisition with $\sin 2\theta$ processing of the scanner output. The wheel speed is cycled twice during each revolution of the spacecraft, resulting in a reduction of the vehicle's energy. Finally, as the motion crosses the separatrix, tumbling gives way to oscillation and capture has been effected. In this instance, an upside-down capture is shown and a subsequent turn-over maneuver (to be discussed in a later section) is required. Figure I-15 indicates the effect of reducing the motor torque from 5 in-oz to 2 in-oz. Notice that more than twice as many revolutions of the vehicle are required before capture occurs. The speed of capture depends strongly upon H_D , as well, as was shown in the First Quarterly Report under the assumption of infinite motor torque; the present phase trajectories correspond to $H_D = 1 \text{ ft-lb-sec}$.

This acquisition procedure is successful because the cyclic wheel activity during a half-revolution transfers the vehicle motion from its original trajectory to a trajectory corresponding to a lower level of spacecraft energy. It is clear, from examining the

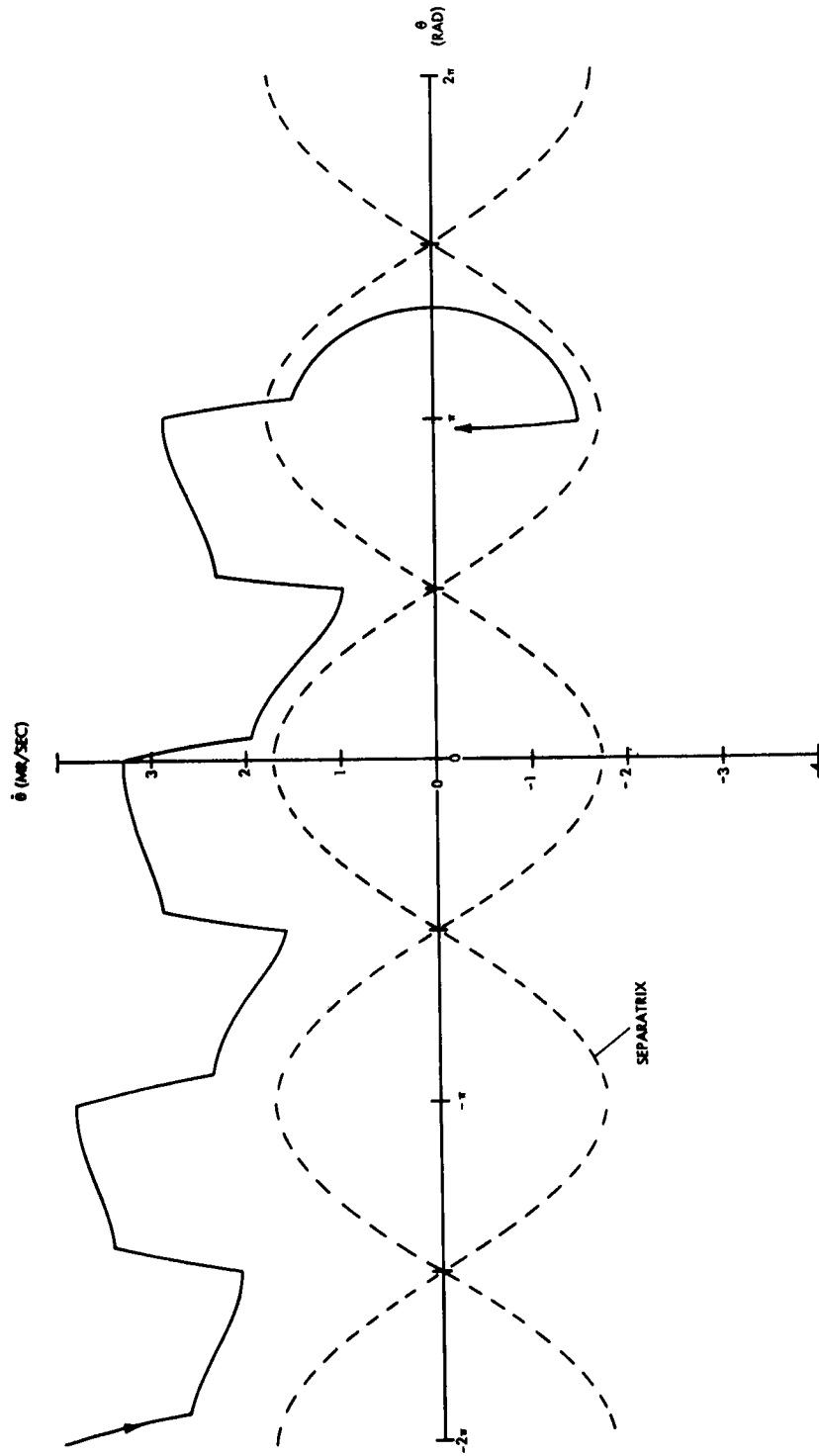


Figure I-14 Pitch Capture with "Sin 2θ " Processing
 ($T_m = 5$ in-oz, $H_D = 1$ ft-lb-sec)

autonomous (uncontrolled) phase trajectories, that $\sin\theta$ processing will not permit capture from larger tumbling rates because, during the single vehicle revolution required to cycle the wheel, no net change in the vehicle energy occurs; the tumbling motion will persist.

For successful pitch acquisition the scanner output must have a "second-harmonic" component so that wheel run-up and run-down events will occur approximately one quarter of a revolution apart. As expected, then, the blanked characteristic of Figure I-13 will give successful capture, but with considerably less speed than $\sin 2\theta$ processing (Figure I-16). This result is of considerable significance for cases in which the vehicle geometry imposes severe blanking requirements. (Note that in this case tachometer feedback causes the wheel to return to its bias speed when the error signal goes to zero at $\theta = -3\pi/2$; this effect is shown approximately in Figure I-16).

Although larger values of T_m and H_D will expedite pitch capture, these considerations must be traded against other factors; for example, scanner output processing requirements and roll/yaw stability considerations can limit the speed range of the wheel. In order to properly weigh all of the factors which influence selection of T_m and H_D , some specification must be placed upon the time allowed for acquisition; lacking such information, reasonable design values for the vehicle considered here are:

$$H_D : 0.5 - 1.0 \text{ ft-lb-sec}$$

$$H_B : - 3.0 \text{ ft-lb-sec}^*$$

$$T_m : 5 \text{ in-oz}$$

*Derived from small-error considerations (see Appendix IV).

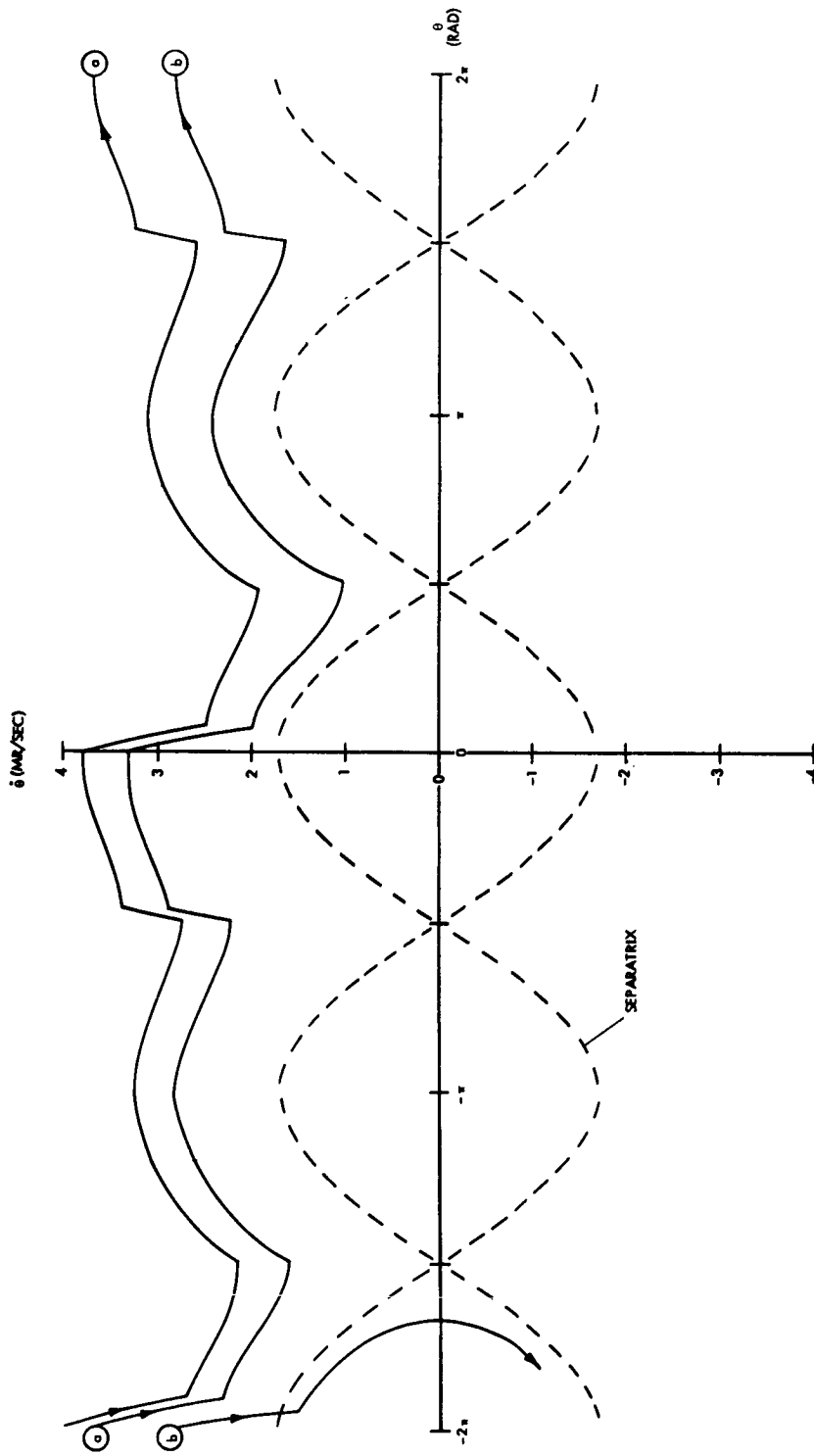


Figure I-16 Pitch Capture with Blanking
 at $+(90 - \rho_0)^0$ ($T_m = 5$ in-oz, $H_D = 1$ ft-lb-sec)

3. Turnover

As noted previously, capture can occur with the vehicle upside-down. In such an event a turnover maneuver must be executed. The reaction wheel offers an ideal mechanism with which to accomplish this goal.

A case in which upside capture occurs was presented in Figure I-14. If damping were included, the motion would eventually stabilize at $\theta = \pi$, a stable equilibrium for $\sin 2\theta$ wheel control. However, this equilibrium is unstable if the wheel is controlled according to the $\sin\theta$ law. Therefore, if, following the completion of pitch acquisition (as indicated by telemetered error signals and/or wheel speed measurements), the weighting of scan cone quadrants 2 and 3 is inverted by ground command, turnover (if required) will occur automatically. The resulting motion is approximately as shown in Figure I-17.

If the scanner processing includes blanking, this procedure will not work; in particular, roll/yaw acquisition can terminate with the vehicle oscillating about $\theta = \pi$ with an amplitude such that no error signal is generated. In this event, an open loop turnover must be commanded from the ground, either by cycling the wheel to re-introduce tumbling (as shown in Figure I-17) or by retracting and re-extending the inertia mast to achieve the same end. The former alternative is certainly the most easily understood, and is also the most appealing from the standpoint of reliability and mechanization.

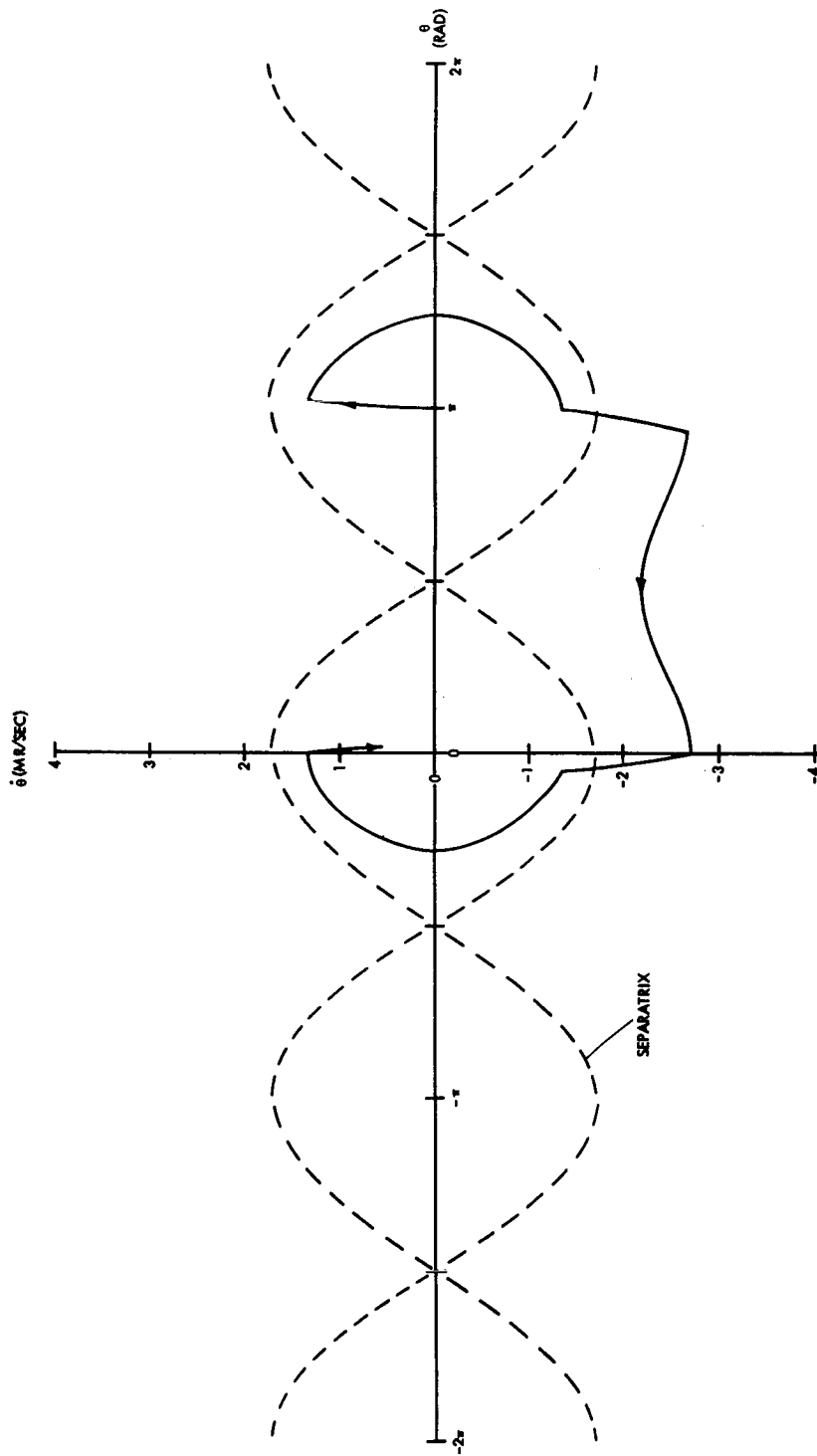


Figure I-17 Turnover Maneuver with "Sine" Processing
 $T_m = 5 \text{ in-oz}$, $H_D = 1 \text{ ft-lb-sec}$

REFERENCES

- I-1 N. I. Kolesnikov, "On the Stability of a Free Gyrostat,"
PMM, 27, 4, 196
- I-2 T. R. Kane and D. L. Mingori, "Effect of a Rotor on the
Attitude Stability of a Satellite in a Circular Orbit,"
AIAA Journal, 3, 5, May 1965.
- I-3 R. Pringle, "On the Captive, Stability and Passive Damping
of Artificial Satellites," SUDAER No. 181, Dept. of Aeronautics
And Astronautics, Stanford University, April 1964.
- I-4 N. G. Chetaev, The Stability of Motion, Pergamon Press,
New York, 1961.

APPENDIX II
SAGS ACQUISITION SIMULATION

A. INTRODUCTION

In order to evaluate roll/yaw acquisition performance, the equations developed here were simulated. Owing to the wide disparity in the magnitudes of the gyroscopic and gravity gradient torques, analog simulation of these equations presents scaling difficulties; for this reason, the simulation has been carried out digitally employing MIDAS (Modified Integration Digital Analog Simulation).

Two versions of the acquisition simulation have been developed, one with a constant speed pitch reaction wheel and the other including an approximate model of the pitch control loop. The former program is a valid representation of roll/yaw acquisition in the case that pitch control is activated following roll/yaw acquisition, and considerable savings in computer time can be obtained by its use.*

B. DEVELOPMENT OF SIMULATION EQUATIONS

1. Dynamics and Kinematics

Assuming that the mass center of the reaction wheel assembly is coincident with that of the vehicle the dynamical equations can be obtained from:

$$\begin{aligned} I_x \dot{\omega}_x + (I_z - I_y) \omega_y \omega_z &= T_{gx} + T_c \\ I_y \dot{\omega}_y + (I_x - I_z) \omega_x \omega_z &= T_{gy} + T_{By} \\ I_z \dot{\omega}_z + (I_y - I_x) \omega_x \omega_y &= T_{gz} + T_{Bz} \end{aligned} \quad (II.1)$$

*Owing to the extreme reduction of computation speed caused by inclusion of the pitch control system, all roll/yaw acquisition runs were made with a constant speed pitch wheel. Pitch acquisition was treated via phase plane techniques.

$$\begin{aligned}
J_1 \dot{\omega}_1 + (J_3 - J_2) \omega_2 \omega_3 - \omega_3 H_c &= T_{g1} - T_c \\
J_2 \dot{\omega}_2 + (J_1 - J_3) \omega_1 \omega_3 + \dot{H}_c &= T_{g2} + T_{B2} \\
J_3 \dot{\omega}_3 + (J_2 - J_1) \omega_1 \omega_2 + \omega_1 H_c &= T_{g3} + T_{B3}
\end{aligned} \tag{II.2}$$

where

I_x, I_y, I_z are the vehicle inertias

J_1, J_2, J_3 are the wheel assembly inertias

$\omega_x, \omega_y, \omega_z$ are the components in vehicle coordinates of the vehicle angular velocity

$\omega_1, \omega_2, \omega_3$ are the components in gimbal coordinates of the wheel assembly angular velocity

H_c is the wheel momentum

$T_{gx}, T_{gy}, T_{gz}, T_{g1}, T_{g2}, T_{g3}$ are gravity gradient torque components

T_c is the constraint torque acting in the gimbal

$T_{By}, T_{Bz}, T_{B2}, T_{B3}$ are bearing torque components.

The constraint torque will be taken to be

$$T_c = c \dot{r} + f(r) \tag{II.3}$$

with

$$f(r) = \begin{cases} k r & , |r| < r_s \\ [k + k_s (|r| - r_s)^2] r, & |r| > r_s \end{cases} \tag{II.4}$$

Note that proportional damping (e.g., eddy current damping) is assumed. The effect of the gimbal stop at γ_s is represented by a non-linear spring characteristic; although this representation may not be the most accurate, it should be conservative in the sense that it neglects the (desirable) effect of energy transfer to the vehicle and its subsequent dissipation in the inertia mast.*

Utilizing the rotation matrix relating the gimbal coordinate frame to the vehicle coordinate frame, i.e.,

$$\begin{bmatrix} \bar{x}_g \\ \bar{y}_g \\ \bar{z}_g \end{bmatrix} = \begin{bmatrix} 1 & 0 & 0 \\ 0 & \cos\gamma & \sin\gamma \\ 0 & -\sin\gamma & \cos\gamma \end{bmatrix} \begin{bmatrix} \bar{x}_b \\ \bar{y}_b \\ \bar{z}_b \end{bmatrix} \quad (\text{II.5})$$

the dynamical equations can be manipulated to yield four final equations. Neglecting the inertias of the wheel assembly ($J_1 = J_2 = J_3 = 0$):

$$\begin{aligned} I_x \dot{\omega}_x + (I_z - I_y) \omega_y \omega_z &= T_{gx} - H_c (\omega_y \sin\gamma - \omega_z \cos\gamma) \\ I_y \dot{\omega}_y + (I_x - I_z) \omega_x \omega_z &= T_{gy} - \dot{H}_c \cos\gamma + H_c (\dot{\gamma} + \omega_x) \sin\gamma \\ I_z \dot{\omega}_z + (I_y - I_x) \omega_x \omega_y &= T_{gz} - \dot{H}_c \sin\gamma - H_c (\dot{\gamma} + \omega_x) \cos\gamma \\ c \dot{\gamma} + f(\gamma) + H_c (\omega_y \sin\gamma - \omega_z \cos\gamma) &= 0 \end{aligned} \quad (\text{II.6})$$

The orientation of the vehicle in the (x_r, y_r, z_r) rotating geocentric coordinate frame can be represented by Euler parameters.

*A continuous spring characteristic has been selected to avoid computational difficulties.

Considering any rotation of the vehicle relative to (x_r, y_r, z_r) as a rotation through an angle \mathcal{J} about an axis defined (in either coordinate frame) by the direction cosines (m_1, m_2, m_3) , the rotation can be represented by the Euler parameters:

$$\begin{aligned} E_1 &= m_1 \sin(\mathcal{J}/2), & i &= 1, 2, 3. \\ E_4 &= \cos(\mathcal{J}/2) \end{aligned} \tag{II.7}$$

In terms of the Euler parameters, the elements of the rotation matrix relating the vehicle frame to the (x_r, y_r, z_r) frame are:*

$$\begin{aligned} a_{11} &= E_1^2 - E_2^2 - E_3^2 + E_4^2 \\ a_{12} &= 2(E_1 E_2 + E_3 E_4) \\ a_{13} &= 2(E_1 E_3 - E_2 E_4) \\ a_{21} &= 2(E_1 E_2 - E_3 E_4) \\ a_{22} &= -E_1^2 + E_2^2 - E_3^2 + E_4^2 \\ a_{23} &= 2(E_2 E_3 + E_1 E_4) \\ a_{31} &= 2(E_1 E_3 - E_2 E_4) \\ a_{32} &= 2(E_2 E_3 - E_1 E_4) \\ a_{33} &= -E_1^2 - E_2^2 + E_3^2 + E_4^2 \end{aligned} \tag{II.8}$$

*For small rotations ϕ , θ and ψ :

$$\phi \approx 2E_1, \quad \theta \approx 2E_2, \quad \psi \approx 2E_3, \quad 1 \approx E_4$$

The appropriate kinematical differential equations are:

$$\begin{aligned}
 \dot{E}_1 &= \frac{1}{2} [\omega_z E_2 - (\omega_y - \omega_0) E_3 + \omega_x E_4] \\
 \dot{E}_2 &= \frac{1}{2} [-\omega_z E_1 + \omega_x E_3 + (\omega_y + \omega_0) E_4] \\
 \dot{E}_3 &= \frac{1}{2} [(\omega_y - \omega_0) E_1 - \omega_x E_2 + \omega_z E_4] \\
 \dot{E}_4 &= \frac{1}{2} [-\omega_x E_1 - (\omega_y + \omega_0) E_2 - \omega_z E_3]
 \end{aligned}
 \tag{II.9}$$

The terms involving ω_0 arise because the (x_r, y_r, z_r) frame is rotating in inertial space with the angular velocity $-\omega_0 \bar{y}_r$.

The dynamical equations (II.6) can now be completed by adding the gravity gradient torques, given (for circular orbits) by:

$$\begin{aligned}
 T_{gx} &= 3\omega_0^2 (I_z - I_y) a_{23} a_{33} \\
 T_{gy} &= 3\omega_0^2 (I_x - I_z) a_{13} a_{33} \\
 T_{gz} &= 3\omega_0^2 (I_y - I_x) a_{13} a_{23}
 \end{aligned}
 \tag{II.10}$$

The fact that these equations are amenable to normalization is of considerable importance when attempting to generalize the simulation results to other situations (e.g., varying orbital altitudes).

The normalized equations are:

$$\begin{aligned}
 \xi p' + (\zeta - 1) qr &= 3 (\zeta - 1) a_{23} a_{33}^{-\mu} (q \sin \gamma - r \cos \gamma) \\
 q' + (\xi - \zeta) pr &= 3 (\xi - \zeta) a_{13} a_{33}^{+\mu} (\gamma' + p) \sin \gamma - \mu' \cos \gamma \\
 \zeta r' + (1 - \xi) pq &= 3 (1 - \xi) a_{13} a_{23}^{-\mu} (\gamma' + p) \cos \gamma - \mu' \sin \gamma \\
 \alpha r' + g(\gamma) + \mu (q \sin \gamma - r \cos \gamma) &= 0
 \end{aligned}
 \tag{II.11a}$$

and

$$\begin{aligned}
 E_1' &= \frac{1}{2} [rE_2 - (q-1) E_3 + p E_4] \\
 E_2' &= \frac{1}{2} [-rE_1 + p E_3 + (q+1) E_4] \\
 E_3' &= \frac{1}{2} [(q-1) E_1 - pE_2 + rE_4] \\
 E_4' &= \frac{1}{2} [-pE_1 - (q+1) E_2 - rE_3]
 \end{aligned}
 \tag{II.11b}$$

where

$$\begin{aligned}
 \omega_x &= \omega_o p, \quad \omega_y = \omega_o q, \quad \omega_z = \omega_o r \\
 \tau &= \omega_o t, \quad \frac{d}{dt} (-) = \omega_o \frac{d}{d\tau} (-) \rightarrow (\dot{-}) = \omega_o (-)' \\
 I_x &= \xi I_y, \quad I_z = \zeta I_y \\
 H_c &= \mu \omega_o I_y, \quad c = \alpha \omega_o I_y, \quad f(\gamma) = \omega_o^2 I_y g(\gamma)^*
 \end{aligned}$$

These results indicate that having obtained results for particular values of the system parameters, the orbital angular velocity, and the vehicle inertias, we can extend these results to any other situation in which the normalized parameters (c, ξ , etc.) are the same. In particular the time to acquire (in terms of τ , the number of orbits) will be unchanged for a given set of initial conditions.

2. Reaction Wheel Control

The reaction wheel control law system included in the acquisition simulation is shown in Figure II-1. The assumption of a

*That is:

$$k = \omega_o^2 I_y \beta, \quad k_s = \omega_o^2 I_y \beta_s \text{ in Eq. (II.4)}$$

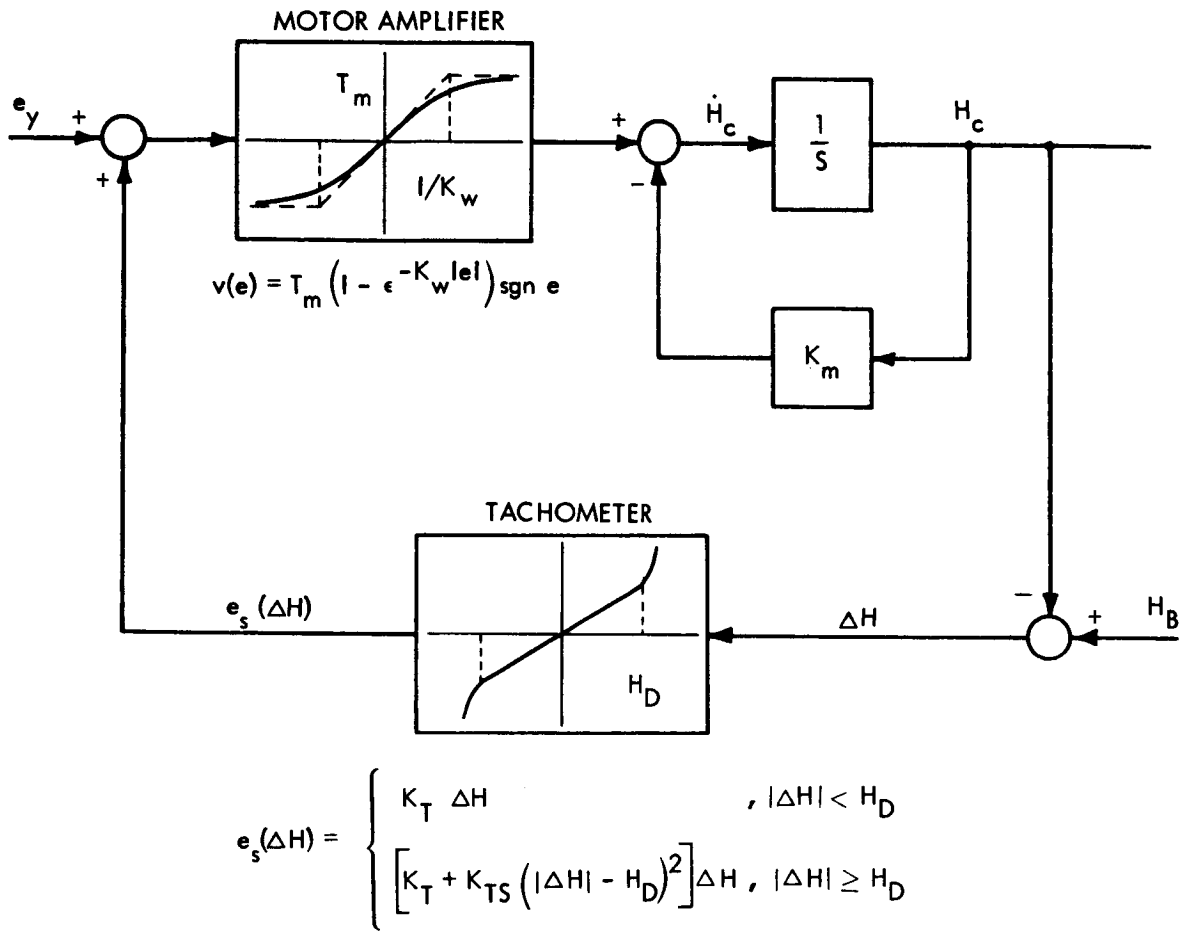


Figure II-1 Reaction Wheel Control Law in SAGS Acquisition Simulation

"flat" torque curve is particularly valid in this instance since the motor is constrained to operate in a small portion of its speed range by the biasing loop. Notice that all non-linearities are represented by smooth functions for computational purposes.

The error signal e_y can be derived from the horizon scanner simulation (see below), or by using appropriate combinations of the direction cosines as developed in the preceding section.

3. Horizon Scanner Outputs

A development of the conical horizon scanner outputs was presented in the SAGS First Quarterly Report. The model appropriate to the current problem is summarized here. The pitch error signal is:

$$e_y = K_e (K_1 W_1 + K_2 W_2 + K_3 W_3 + K_4 W_4) \operatorname{sgn} \delta \quad (\text{II.12})$$

where W_i is the width of the pulse portion occurring in the i -th quadrant of the partitioned scan cone. This representation allows simulation of the three processing schemes of primary interest:

(i) $\sin 2\theta$ processing:

$$K_1 = K_3 = +1, K_2 = K_4 = -1$$

(ii) $\sin \theta$ processing:

$$K_1 = K_2 = +1, K_3 = K_4 = -1$$

(iii) Blanked $\sin \theta$ processing (180° FOV)

$$K_1 = +1, K_2 = K_3 = 0, K_4 = -1$$

The gain constant K_e is selected so that for small errors $e_y \approx \theta$. For example, with $\sin 2\theta$ processing $K_e = -\frac{1}{2}$.

The computation of W_1, W_2, W_3 and W_4 is accomplished as indicated in Figure II-2. The angles δ and ρ are computed from

$$\frac{\sin \delta}{\cos \delta} = \frac{c_{13}}{c_{33}} ; \quad (-\pi \leq \delta \leq \pi)$$

$$Q = \frac{\cos \alpha_e - c_{23} \cos \sigma}{\sqrt{1 - c_{23}^2} \sin \sigma} \quad (\text{II.13})$$

$$\rho = \begin{cases} 0 & , \quad Q > 1 \\ \cos^{-1} Q & , \quad Q \in [-1, 1] \\ \pi & , \quad Q < -1 \end{cases}$$

where

$$c_{13} = a_{13}$$

$$c_{23} = a_{23} \cos \gamma + a_{33} \sin \gamma$$

$$c_{33} = -a_{23} \sin \gamma + a_{33} \cos \gamma$$

$$\sin \alpha_e = \frac{R_e}{R_e + h}$$

and σ is the half-angle of the scan cone. The variable δ represents the distance of earth pulse center from the primary scanner reference marker, while ρ is the half-width of the pulse ($0 \leq \rho \leq \pi$). The option of replacing c_{13}, c_{23} and c_{33} in (II.13) by a_{13}, a_{23} and a_{33} has been provided to allow consideration of a vehicle-fixed (ungimballed) scanner.

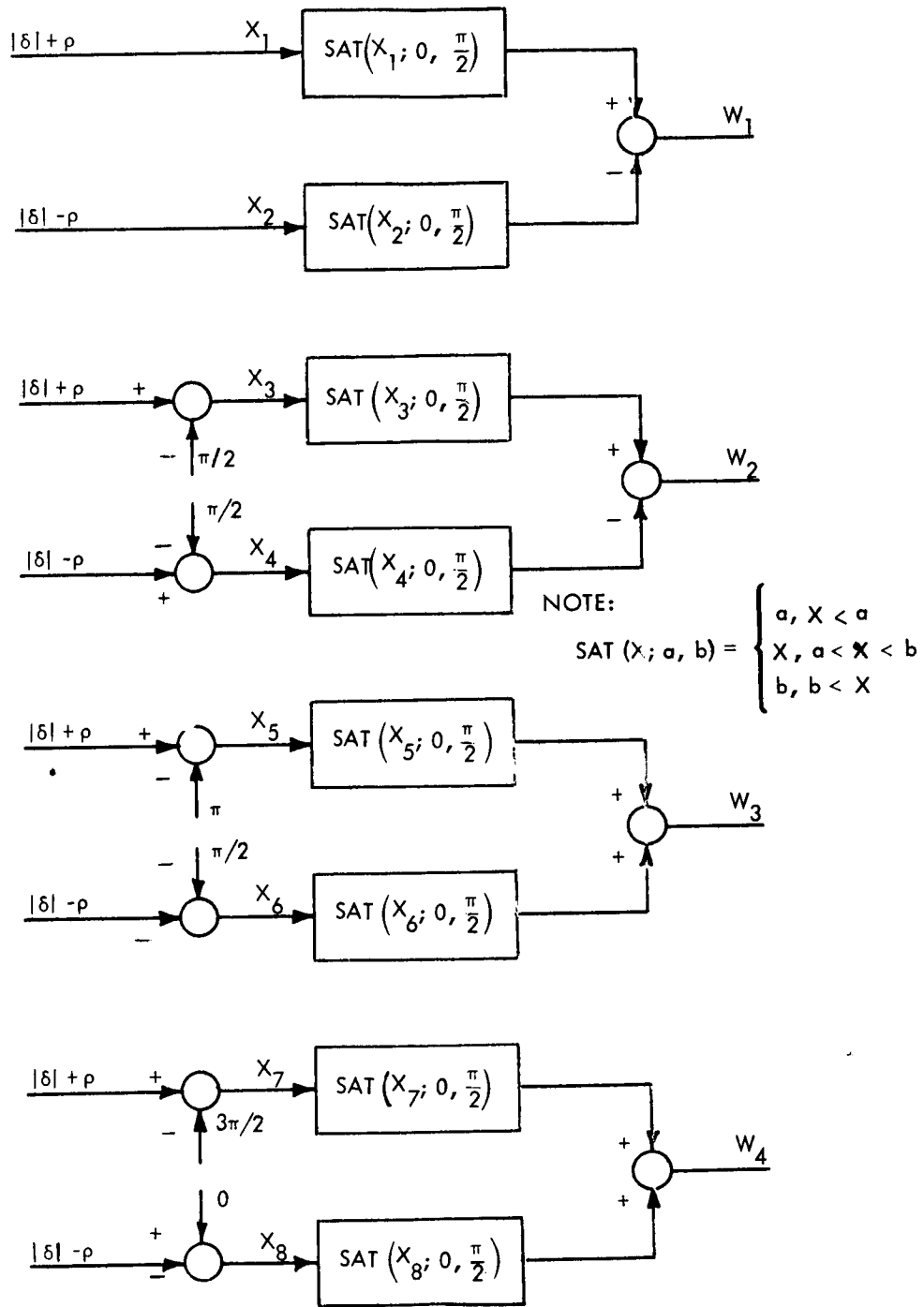


Figure II-2 Horizon Scanner Processing Logic

3. Initial Condition/Solution Symmetry

In previous acquisition simulations it has been noticed that solutions arising from related initial condition sets are often "similar". This phenomenon occurs due to the symmetry properties of the differential equations. Consider the following theorem:

Theorem:

Let $\dot{\bar{x}} = \bar{f}(\bar{x})$ such that solutions exist and are unique everywhere, and consider solutions $\bar{\phi}(t; \bar{x}_1)$ and $\bar{\phi}(t; \bar{x}_2)$ arising from initial states \bar{x}_1 and \bar{x}_2 . Assume that $\bar{f}(x)$ has the property that

$$\bar{f}(A\bar{x}) = A\bar{f}(\bar{x})$$

for some real $n \times n$ matrix A and, further, that the initial states \bar{x}_1 and \bar{x}_2 are related by

$$\bar{x}_2 = A \bar{x}_1$$

Then the solution arising from \bar{x}_2 is

$$\bar{\phi}(t; \bar{x}_2) = A \bar{\phi}(t; \bar{x}_1)$$

Proof:

(1) The two solutions of interest are given by

$$\bar{\phi}(t; \bar{x}_1) = \bar{x}_1 + \int_{t_0}^t \bar{f}(\bar{\phi}(\tau; \bar{x}_1)) d\tau \quad (*)$$

$$\bar{\phi}(t; \bar{x}_2) = \bar{x}_2 + \int_{t_0}^t \bar{f}(\bar{\phi}(\tau; \bar{x}_2)) d\tau \quad (**)$$

- (2) Assume that the proposition is true. Then the left side of (**) is simply

$$A \bar{\phi} (t ; \bar{x}_1)$$

- (3) Using $\bar{f}(A \bar{x}) = A \bar{f}(\bar{x})$ and $\bar{x}_2 = A \bar{x}_1$ the right side of (**) is

$$\begin{aligned} \bar{x}_2 + \int_{t_0}^t \bar{f}(\bar{\phi}(\tau ; \bar{x}_2)) d\tau &= A\bar{x}_1 + \int_{t_0}^t \bar{f}(A\bar{\phi}(\tau ; \bar{x}_1)) d\tau \\ &= A \left\{ \bar{x}_1 + \int_{t_0}^t \bar{f}(\bar{\phi}_1(\tau ; \bar{x}_1)) d\tau \right\} = A\bar{\phi}_1(\tau ; \bar{x}_1) \end{aligned}$$

- (4) Thus $\bar{\phi}(t ; \bar{x}_2) = A\bar{\phi}(t ; \bar{x}_1)$ has been shown to be a solution arising from \bar{x}_2 . By uniqueness it is the only such solution.

The preceding result is useful only if a suitable matrix A can be found. In this regard it is useful to treat the special case in which A is a diagonal matrix with all elements having unity magnitude. Denoting the components of \bar{x} by x_j , and the corresponding element of A by α_j the symmetry conditions can be expressed as:

$$f_j(\alpha_1 x_1, \alpha_2 x_2, \dots, \alpha_n x_n) = \alpha_j f_j(x_1, x_2, \dots, x_n) \quad (\text{II.14})$$

This test is much easier to perform than the general one resulting when A is arbitrary. Even though there are still 2^n possible choices for A , many of them will be eliminated at the outset by trivial constraints.

As an example, this result can be applied to the SAGS acquisition equations (with the wheel speed assumed to be constant).

Subscripting the state variables in the order ($\omega_x, \omega_y, \omega_z, r, E_1, E_2, E_3, E_4$), the following conditions are obtained from the 8 equations represented by (II.14):

$$\begin{aligned}
 \text{(i)} \quad & \alpha_1 = \alpha_2 \alpha_3 = \alpha_6 \alpha_7 = \alpha_5 \alpha_8 = \alpha_2 \alpha_4 = \alpha_3 \\
 \text{(ii)} \quad & \alpha_2 = \alpha_1 \alpha_3 = \alpha_5 \alpha_7 = \alpha_6 \alpha_8 = \alpha_4^2 = \alpha_1 \alpha_4 \\
 \text{(iii)} \quad & \alpha_3 = \alpha_1 \alpha_2 = \alpha_4 = \alpha_1 = \alpha_5 \alpha_6 = \alpha_7 \alpha_8 \\
 \text{(iv)} \quad & \alpha_4 = \alpha_2 \alpha_4 = \alpha_3 \qquad \qquad \qquad \text{(II.15)} \\
 \text{(v)} \quad & \alpha_5 = \alpha_3 \alpha_6 = \alpha_7 = \alpha_7 \alpha_2 = \alpha_1 \alpha_8 \\
 \text{(vi)} \quad & \alpha_6 = \alpha_3 \alpha_5 = \alpha_1 \alpha_7 = \alpha_8 = \alpha_2 \alpha_8 \\
 \text{(vii)} \quad & \alpha_7 = \alpha_5 = \alpha_5 \alpha_2 = \alpha_1 \alpha_6 = \alpha_3 \alpha_8 \\
 \text{(viii)} \quad & \alpha_8 = \alpha_1 \alpha_5 = \alpha_6 = \alpha_2 \alpha_6 = \alpha_3 \alpha_7
 \end{aligned}$$

Removing redundancies, these conditions reduce to:

$$\begin{aligned}
 \alpha_1 &= \alpha_3 = \alpha_4 = \alpha_5 \alpha_6 \\
 \alpha_2 &= 1 \\
 \alpha_7 &= \alpha_5 \\
 \alpha_8 &= \alpha_6
 \end{aligned}
 \qquad \qquad \qquad \text{(II.16)}$$

Thus the symmetrical initial states are:

$$\begin{array}{cccc} \omega_x & -\omega_x & -\omega_x & \omega_x \\ \omega_y & \omega_y & \omega_y & \omega_y \\ \omega_z & -\omega_z & -\omega_z & \omega_z \\ \gamma & -\gamma & -\gamma & \gamma \\ E_1 & E_1 & -E_1 & -E_1 \\ E_2 & -E_2 & E_2 & -E_2 \\ E_3 & E_3 & -E_3 & -E_3 \\ E_4 & -E_4 & E_4 & -E_4 \end{array} \quad (\text{II.17})$$

Having once determined the response for the first of these initial states, the response for any of the others can be obtained by changing the signs of the appropriate variables in the original result.

APPENDIX III

REACTION WHEEL CONTROL SYSTEM DESIGN STUDIES

A. INTRODUCTION

The SAGS control configuration provides for pitch axis control by perturbing the speed of the gimballed reaction wheel about its bias level, in response to the processed horizon scanner output signal. The reaction wheel control system must provide pitch attitude control while maintaining the wheel speed in a small neighborhood of the nominal bias speed. These functions must be performed in the presence of environmental disturbances which cannot be precisely estimated; thus, the design evolved must be one which will function (perhaps with somewhat reduced attitude accuracy) in the presence of abnormal perturbative effects.

Figure III-1 shows the general configuration considered for control of the pitch wheel. The pulse modulator, represented in Figure III-1 by its slow-signal average input/output characteristic, is mechanized as shown in Figure III-2. The motor torque-speed relationship is here taken as "flat," a particularly valid representation because the motor always operates in a restricted portion of its speed range by virtue of the speed inhibit loop.

The effect of a constant disturbance torque (T_{do}) will be a steady pitch offset (θ_o). Neglecting the compensation network and assuming θ_c to be zero, the effect of a constant error in excess of the modulator deadband (θ_D) will be a constant average motor torque. This will cause the wheel to accelerate until the magnitude of $H_B - H_c$ exceeds H_D . At this point the effectiveness of pitch control (for example, in reacting to periodic components of T_d) will be

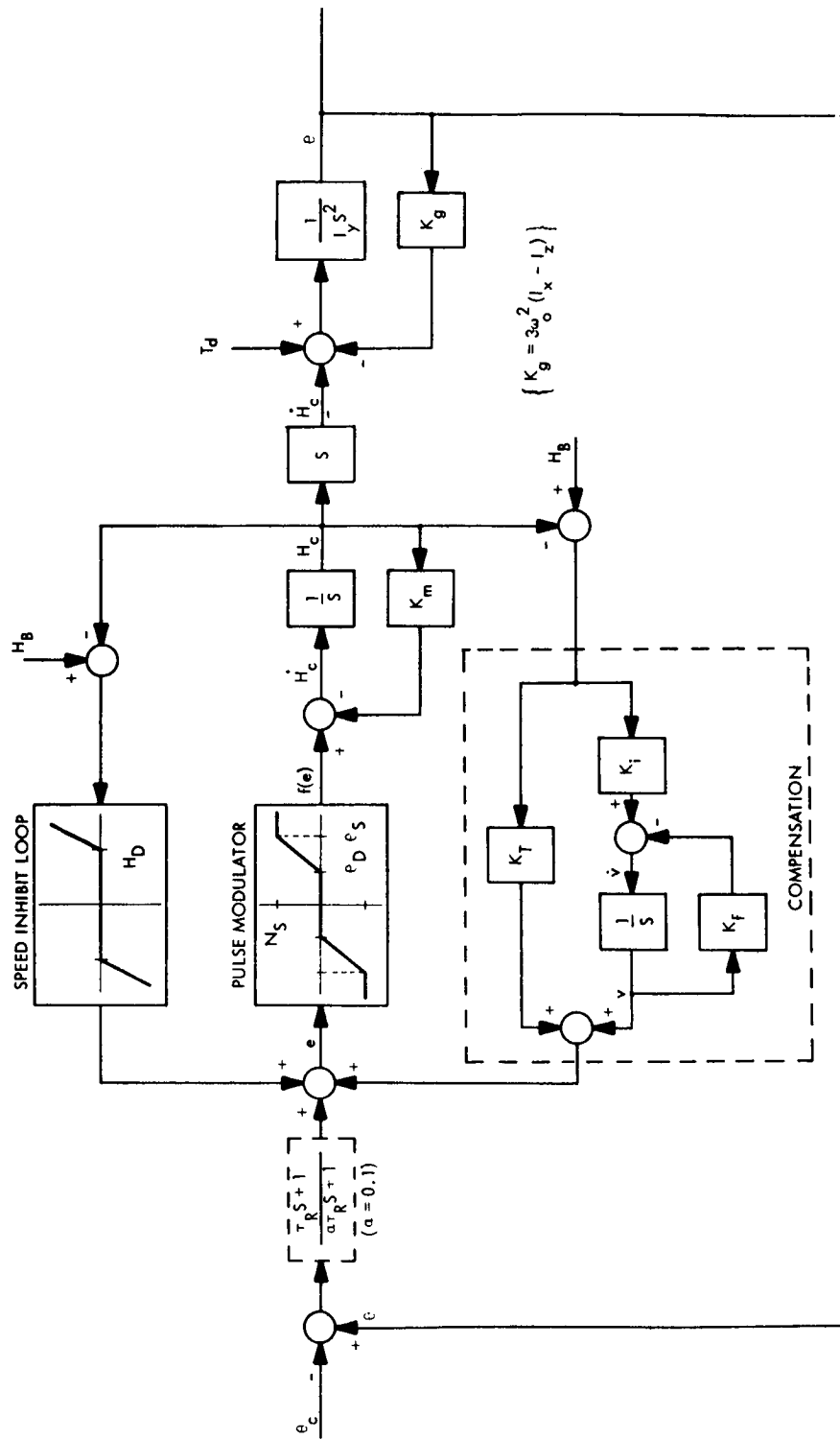


Figure III-1 Reaction Wheel Control System

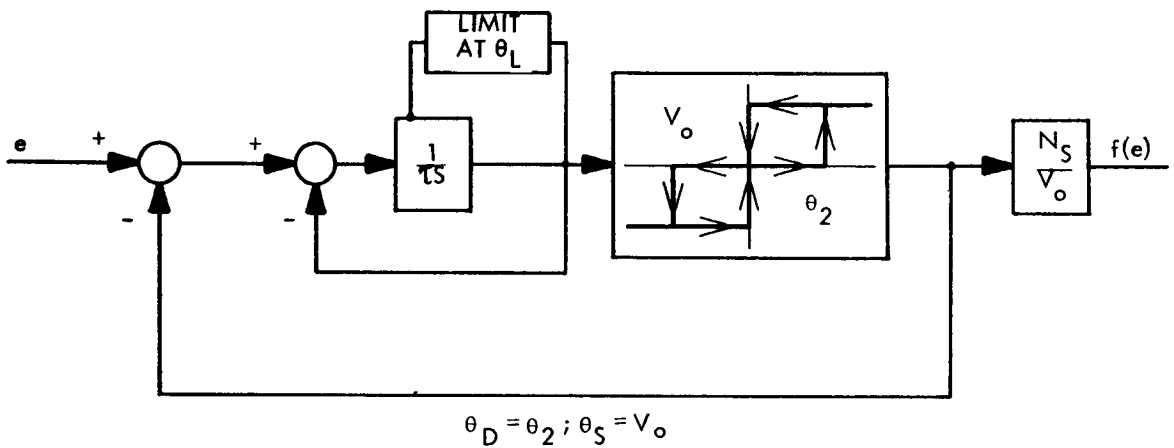


Figure III-2 Pulse Ratio Modulator Mechanization

seriously impaired.

The purpose of the compensation network is to avoid the degradation in pitch performance observed above. By adding to the error signal a term which depends upon the incremental wheel momentum ($H_B - H_C$), steady-state operation can be reached without excessive speed excursions. The system is converted from one in which \dot{H}_C is proportional to attitude error to one in which $H_C - H_B$ is essentially proportional to Θ . Notice that two compensation techniques are considered, one a proportional channel and the other an integral channel (with K_F on the order of 10^{-4} sec^{-1}). Three configurations were simulated: (i) proportional compensation only; (ii) integral compensation only; and, (iii) proportional plus integral compensation. The simplest of these (proportional tachometer feedback) appears to offer adequate steady-state performance and, of the three configurations, gives the most highly damped transient performance.

B. ANALYSIS

A considerable degree of insight can be obtained by analyzing the configuration of Figure III-1 with some simplifying assumptions. Of immediate interest is the response of the system (in particular of Θ and H_C) to constant and orbital frequency disturbance torques. For this purpose a static representation of the modulator is reasonable, as is omission of the lead-lag network. If the system performs acceptably, the speed inhibit loop will be excited only during the large attitude excursions associated with acquisition. Neglecting these factors the system can be represented by:

$$\begin{aligned}\ddot{\Theta} &= \frac{1}{I_y} (T_d - \dot{H}_C - K_g \Theta) \\ \dot{H}_C &= f(e) - K_m H_C \\ \dot{v} &= K_1 (H_B - H_C) - K_f v\end{aligned}\tag{III.1}$$

where

$$e = \theta - \theta_c + v + K_T(H_B - H_c)$$

Introducing state variable notation ($x_1 = \theta$, $x_2 = I_y \dot{\theta}$, $x_3 = H_c$, $x_4 = v$) these equations become

$$\begin{aligned} \dot{x}_1 &= \frac{1}{I_y} x_2 \\ \dot{x}_2 &= T_d - \dot{x}_3 - K_g x_1 \\ \dot{x}_3 &= f(e) - K_m x_3 \\ \dot{x}_4 &= K_i H_B - K_i x_3 - K_f x_4 \end{aligned} \quad (\text{III.2})$$

with

$$e = x_1 + x_4 - K_T x_3 + K_T H_B - \theta_c .$$

The steady-state response can be derived simply by setting $\dot{x}_i = 0$ for all i . This yields:

$$\begin{aligned} x_{10} &= \frac{T_d}{K_g} \\ x_{20} &= 0 \\ x_{30} &= \frac{1}{K_m} f(e_0) \\ x_{40} &= \frac{1}{K_f} (K_i H_B - K_i x_{30}) \\ e_0 &= x_{10} + x_{40} - K_T x_{30} + K_T H_B - \theta_c \end{aligned} \quad (\text{III.3})$$

Notice that θ_c does not affect the steady value of attitude error; the purpose of this attitude command capability is to relieve the wheel control loop (i.e., reduce the modulator duty cycle under static conditions).

Neglecting the attitude bias command (which is probably not necessary for acceptable system performance) and noting that the system must operate in the regime $\theta_D \leq e_0 \leq \theta_S$ (because the windage torque $K_m H_c$ can never exceed (N_s) , the static operating wheel momentum can be determined to be:

$$H_{c0} = x_{30} = \frac{N_s \{K_f T_D + K_g (K_i + K_f K_T) H_B - K_f K_g \theta_D\}}{K_g \{K_f K_m (\theta_S - \theta_D) + (K_i + K_T K_f) N_s\}}$$

It is of considerable significance that the static operating point is in the active region of the modulator, even with no steady disturbance, owing to the action of the windage torque. Thus, in the absence of disturbances, the control system will hold θ equal to zero instead of allowing limit cycle operation.

It should be noted that the parameters not associated with the compensation loop will be selected on the basis of achieving suitable steady-state accuracy and adequate acquisition response. The deadband and saturation limits will be selected to be consistent with the desired attitude accuracy, but with θ_D larger than the noise level (e.g., 0.2°) which might be expected from the horizon scanner. For pointing accuracies on the order of one degree a reasonable selection for θ_D is 0.5 degree, with θ_S at twice this value. The motor torque will be selected primarily from acquisition considerations; a reasonable value is 5 in-oz. The parameter K_g must be chosen (in terms of the spacecraft roll/yaw inertia difference) so that the pointing error in the presence of the expected constant

environmental disturbance is somewhat less than the required accuracy. For instance, using $T_{d0} = 3 \times 10^{-5}$ ft-lb and $\omega_0 = 10^{-3}$ rad/sec, a roll/yaw inertia difference of 1400 slug-ft² is reasonable. Thus

$$I_x = I_y = 1500 \text{ slug-ft}^2; I_z = 100 \text{ slug-ft}^2$$

The major remaining question, then, is the choice of the parameters of the compensation loop.

As a preliminary design approximation $f(e)$ can be replaced by a gain. Consider now the case of proportional feedback only. Then:

$$\begin{aligned} \dot{x}_1 &= \frac{1}{I_y} x_2 \\ \dot{x}_2 &= T_d - \dot{x}_3 - K_g x_1 \\ \dot{x}_3 &= f(e) - K_m x_3 \end{aligned} \tag{III.4}$$

where

$$\begin{aligned} e &= x_1 - K_T x_3 + K_T H_B - \theta_c \\ f(e) &= K_w e; K_w = N_s / \theta_D \end{aligned}$$

In this case the static wheel momentum will be:

$$H_{CO} = \frac{K_w (T_d + K_T K_g H_B - K_g \theta_c)}{K_g (K_w K_T + K_m)} \approx H_B + \frac{T_d}{K_g K_T} - \frac{\theta_c}{K_T} \tag{III.5}$$

Figure III-3 shows the steady wheel speed offsets due to disturbance torque and windage.

It is also of interest to examine the amplitudes of θ and H_c in response to sinusoidal disturbances at orbital frequency. In the frequency domain:

$$\begin{bmatrix} s & -\frac{1}{I_y} & 0 \\ K_g + K_w & s & -(K_m + K_w K_T) \\ -K_w & 0 & s + K_m + K_w K_T \end{bmatrix} \begin{bmatrix} x_1(s) \\ x_2(s) \\ x_3(s) \end{bmatrix} = \begin{bmatrix} 0 \\ T_D - K_w (K_T H_B - \theta_c) \\ K_w (K_T H_B - K_w \theta_c) \end{bmatrix} \quad (\text{III.6})$$

The characteristic equation is:

$$\Delta(s) = s^3 + (K_m + K_w K_T) s^2 + \frac{K_w + K_g}{I_y} s + \frac{K_g (K_w K_T + K_m)}{I_y} \quad (\text{III.7})$$

Typical parameter values are:

$$K_m: 10^{-3} \text{ to } 10^{-2} \text{ sec}^{-1}$$

$$K_w: 1.0 \text{ to } 10 \text{ ft-lb/rad}$$

$$K_g: 0.005 \text{ ft-lb/rad}$$

$$I_y: 1500 \text{ slug-ft}^2$$

Making the following realistic assumptions

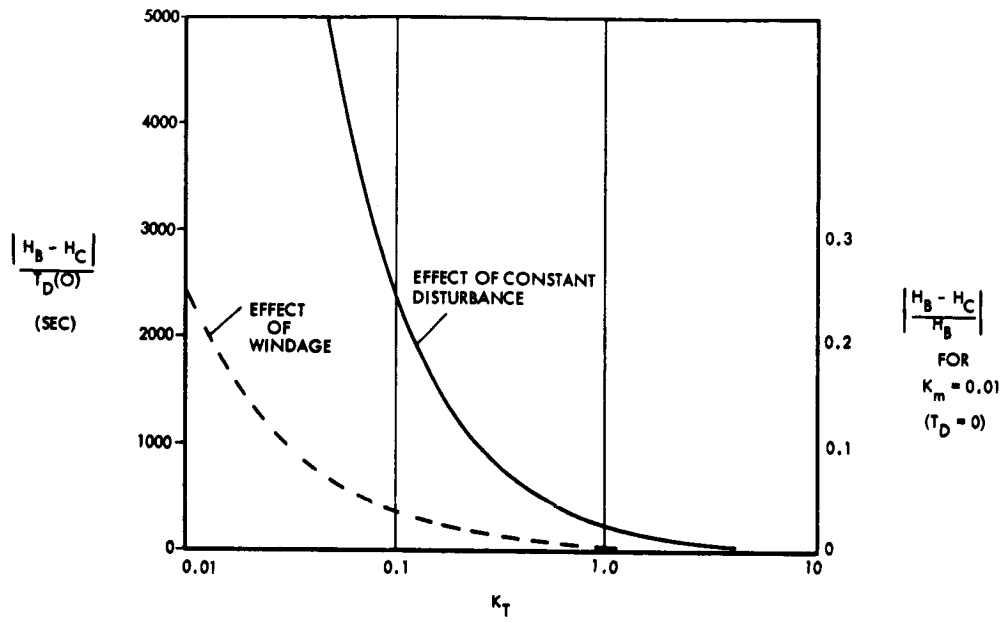


Figure III-3 Static Wheel Speed Offsets due to Disturbance Torque and Windage

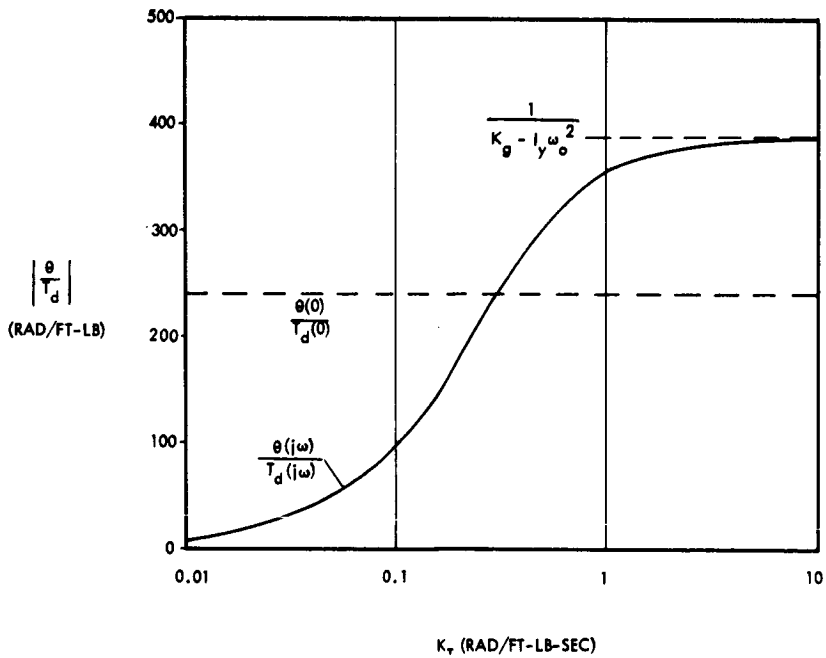


Figure III-4 Attitude Error as a Function of Tachometer Gain

$$K_w K_T \gg K_m$$

$$K_w \gg K_g$$

$$\Delta(s) \approx s^3 + K_w K_T s^2 + \frac{K_w}{I_y} s + \frac{K_w K_T K_g}{I_y} \quad (\text{III.8})$$

Evaluating the response of θ and H_c to disturbances at orbital frequency:

$$\frac{\theta(j\omega_o)}{T_d(j\omega_o)} \approx \frac{1}{(K_g - I_y \omega_o^2) + j(\omega_o/K_T)} \quad (\text{III.9})$$

$$\frac{H_c(j\omega_o)}{T_D(j\omega_o)} \approx \frac{1}{K_T} \cdot \frac{\theta(j\omega_o)}{T_d(j\omega_o)}$$

where the above assumptions have been employed. Figures III-4 and III-5 present these results graphically for $K_m = 0.01 \text{ sec}^{-1}$, $I_x = I_y = 1500 \text{ slug-ft}^2$, $I_z = 100 \text{ slug-ft}^2$ and $\omega_o = 10^{-3} \text{ rad/sec}$ with K_T varied. Figure III-4 indicates that tachometer gains in the range 0.1 to 0.3 will give an orbit-rate response component similar in amplitude to the steady offset. Figure III-5 shows that values of K_T larger than 0.1 are desirable if we wish to reduce the momentum storage requirements. Assuming that the steady and orbit-rate disturbance components are $3 \times 10^{-5} \text{ ft-lb}$ and $4 \times 10^{-5} \text{ ft-lb}$, respectively, the following steady-state performance is predicted by this linear analysis with $K_T = 0.2 \text{ rad/ft-lb-sec}$:

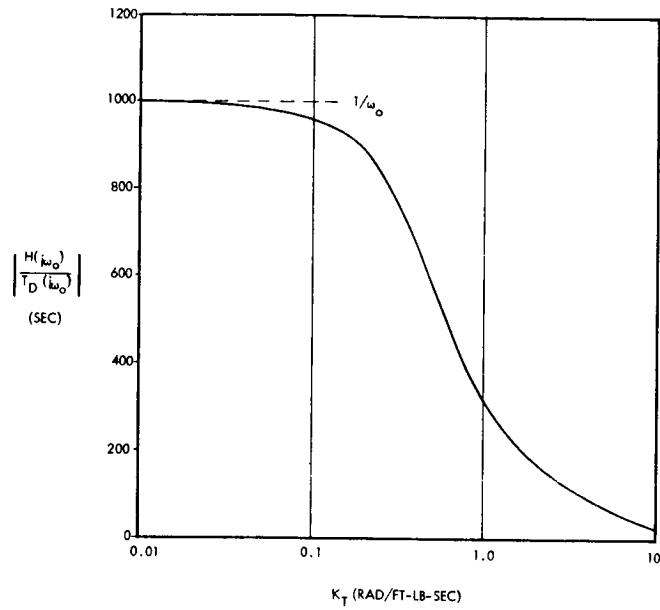


Figure III-5 Momentum Storage Requirements as a Function of Tachometer Gain

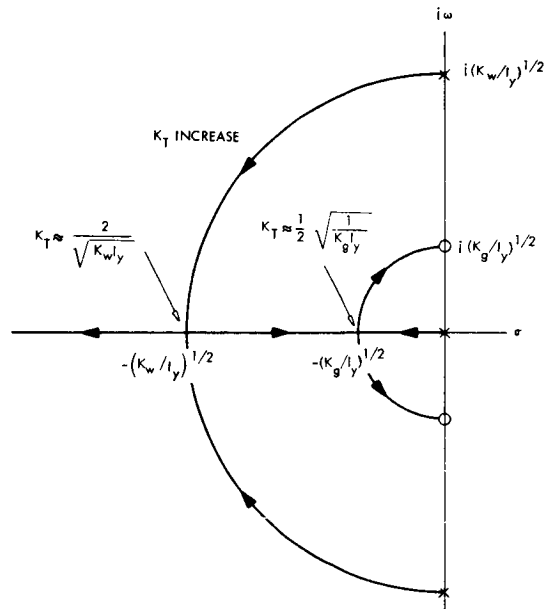


Figure III-6 Reaction Wheel Loop Characteristic Frequencies as a Function of Tachometer Gain

$$H_c(0) = H_B + 0.036 \text{ ft-lb-sec}$$

$$H_c(j\omega_0) = 0.032 \quad \text{ft-lb-sec}$$

$$\theta(0) = 0.41^\circ$$

$$\theta(j\omega_0) = 0.41^\circ$$

This performance is quite acceptable. The addition of an integral compensation loop with its probable greater complexity appears unwarranted in this instance. The major contribution of such a loop would be a reduction in the steady-state wheel speed excursions; such an effect is of minor importance in the SAGS control configuration since the wheel capacity is determined by momentum bias and pitch capture considerations.

The tachometer gain has been chosen above based upon steady-state performance. Its effect upon transient response is of somewhat less importance but is still of interest. To determine the effect of K_T upon the characteristic roots of the system, equation III.8 may be written as:

$$K_T K_W \frac{s^2 + K_g/I_y}{s(s^2 + K_w/I_y)} = -1 \quad (\text{III.10})$$

Figure III-6 shows the corresponding root locus diagram. Notice that the first breakaway point is at $s_1 = -\sqrt{K_w/I_y}$ and occurs with a tachometer gain given by:

$$K_{T1} \approx \frac{2}{\sqrt{K_w I_y}} \quad (\text{III.11})$$

For the breakaway point at $s_2 = -\sqrt{K_g/I_y}$:

$$K_{T2} \approx \frac{1}{2} \sqrt{\frac{1}{K_g I_y}} \quad (\text{III.12})$$

This value of tachometer gain is a good one in that it forces the pole nearest the $j\omega$ axis as far as is possible into the left-half plane, thus minimizing the longest time constant of the system.* Notice that this "optimum" tachometer gain is totally independent of other ACS parameters. For $I_x = I_y = 1500 \text{ slug-ft}^2$, $I_z = 100 \text{ slug-ft}^2$ and $\omega_o = 10^{-3} \text{ rad/sec}$:

$$K_{T2} \approx 0.2 \text{ rad/ft-lb-sec}$$

A more realistic estimate of the system transient response can be obtained by noting that the terminal phase of any autonomous (undisturbed) motion should occur very near the deadband of the modulator (this is so because the wheel torque is generally much greater than the gravity gradient torque and because the windage torque will hold the error at the deadband). Thus, during the terminal transient:

$$\theta - K_T (H_c - H_B) = \theta_D \quad (\text{III.13})$$

$$I_y \ddot{\theta} + \dot{H}_c + K_g \theta = 0$$

*Of course, this assumes that this root is excited significantly during transient response. This may not be the case.

Differentiating the first of these equations and combining the result with the second:

$$I_y \ddot{\theta} + \frac{1}{K_T} \dot{\theta} + K_g \theta = 0 \quad (\text{III.14})$$

Owing to the small size of K_g , the roots will be real for reasonable values of K_T :

$$\lambda_1, \lambda_2 = \frac{1}{2K_T I_y} \left\{ -1 \pm \sqrt{1 - 4 K_g K_T^2 I_y} \right\} \quad (\text{III.15})$$

Note that this yields two equal roots at $s = - (K_g / I_y)^{\frac{1}{2}}$ when

$$K_T = 0.5 (K_g I_y)^{-\frac{1}{2}} ;$$

this result is completely equivalent to that obtained by root locus techniques.

The corresponding time response (for λ_1 and λ_2 real and distinct) is:

$$\theta(t) = \frac{\dot{\theta}(0) - \lambda_2 \theta(0)}{\lambda_1 - \lambda_2} e^{\lambda_1 t} + \frac{\dot{\theta}(0) - \lambda_1 \theta(0)}{\lambda_2 - \lambda_1} e^{\lambda_2 t} \quad (\text{III.16})$$

where $\dot{\theta}(0)$ and $\theta(0)$ refer to the phase point at which this "zero-error" terminal motion begins. Notice that if gravity gradient torques are neglected (i.e., assuming momentum conservation during the time required for the system to first reach the modulation deadband):

$$\theta(0) + K_T I_y \dot{\theta}(0) = \theta_D + K_T H_1 \quad (\text{III.17})$$

where H_1 is the amount by which the initial system momentum exceeds H_B .

Now consider the case in which $4K_I K_T^2 \ll 1$ (in the present instance $K_T \leq 0.1$ will satisfy this requirement). Denoting the near (slower) root by λ_1 :

$$\lambda_1 \approx -K_T K_g ; \lambda_2 \approx -\frac{1}{K_T I_y} \quad (\text{III.18})$$

Combining (III.16), (III.17), and (III.18) yields:

$$\theta(t) \approx (\theta_D + K_T H_1) e^{\lambda_1 t} + [\theta(0) - (\theta_D + K_T H_1)] e^{\lambda_2 t} \quad (\text{III.19})$$

Clearly, for significant initial attitude errors, the faster mode will dominate the motion until the attitude error is reduced to the neighborhood of θ_D . This puts the rationale of maximizing $|\lambda_1|$ in question, because increasing K_T to increase the magnitude of λ_1 will decrease the speed of the dominant mode.

The above result suggests that the reaction wheel motor is performing as a high gain amplifier in that it maintains its input signal very near zero. It is not surprising, then, that all aspects of system performance discussed above are relatively insensitive to the value chosen for K_w , the major requirement being that $K_w K_T$ be much greater than K_m .

C. SIMULATION STUDIES

In order to verify and extend the results of the preceding analysis the system of Figure III-1 was simulated on an analog computer. Both proportional and integral compensation were examined. Transient

response runs employed a simulation of the pulse modulator while a static representation of the modulator was employed for investigation of steady-state behavior (in order to allow runs of sufficient length). It should be noted that these simulation studies were performed prior to the final determination from acquisition considerations of the wheel bias momentum and the motor torque. These discrepancies in no way invalidate the general conclusions available from examining the analog data.

Parameter	Value
I_x (slug-ft ²)	1500
I_y (slug-ft ²)	1500
I_z (slug-ft ²)	100
ω_o (rad/sec)	0.9×10^{-3}
K_m (sec ⁻¹)	0.01
K_f (sec ⁻¹)	10^{-4}
N_s (in-oz)	16
H_B (ft-lb-sec)	2.0
K_T (rad/ft-lb-sec)	0.1
θ_D (deg)	0.5
θ_s (deg)	1.0

Table III-1 Baseline Parameter Values for Analog Study

1. Proportional Tachometer Feedback

Figure III-7 shows the transient response of the baseline system for various initial pitch attitude errors with the wheel momentum initially equal to its bias value. Since these runs were taken with a 10 sec/1 sec lead-lag network in the attitude error feedback path, the data of Figure III-8 was later taken for reference purposes; * the effect of this network is clearly unimportant for this amount of lead information. Notice that, following the initial phase of the motion, the response is essentially exponential (as indicated by the straight-line phase trajectory). The time constant of this motion is approximately 120 seconds; evaluating the characteristic roots from expression (III.15):

$$\lambda_1 = -0.00037 \text{ sec}^{-1}; \quad \lambda_2 = -0.0063 \text{ sec}^{-1}$$

It is clear that the faster root has been excited most significantly in the analog runs; only a low amplitude "slow" exponential motion persists after the fast mode has decayed. These results are in complete agreement with the preceding analysis.

During the runs described above the speed inhibit loop was removed; however, with $H_D = 1.0 \text{ ft-lb-sec}$ (a reasonable value for pitch capture, scanner operation and roll/yaw control) the limit would not have been reached. For larger initial errors limiting would have been observed; the effect would have been an upper limit on $\dot{\theta}$ with a corresponding lengthening of the convergence time.

*As noted earlier, such a compensation network is not necessary with proportional tachometer feedback. As seen in the present data, it adds damping to a system which is already overdamped.

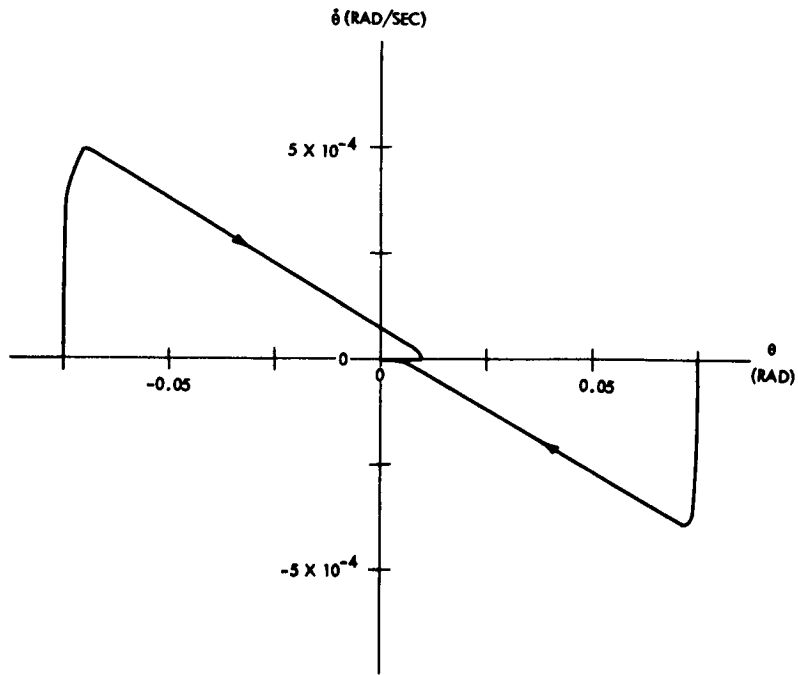


Figure III-7 Transient Response of Baseline System

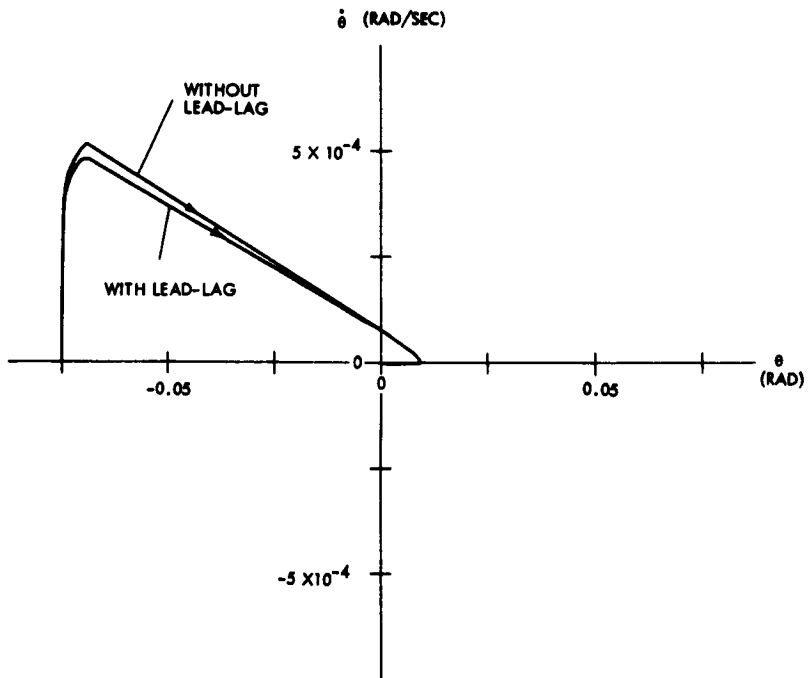


Figure III-8 Effect of Lead-Lag Network upon Transient Response

Figure III-9 shows the effect of various initial wheel momenta, again with no inhibit loop. Notice that the offsetting effect of an initial stored momentum which differs from the bias momentum is predicted by the presence of H_i in expressions (III.17) and (III.19); as H_i increase, the amplitude of the slow component of θ increases. In this case, again, the speed inhibit loop would not have affected the results.

The effect of reducing the windage of the motor is shown in Figure III-10. Clearly there is little effect upon the transient response; however, this is not the complete story. By reducing K_f from 0.01 to 0.002, the duty cycle of the motor during the linear portion of the trajectory is reduced by a factor of five.

The steady-state behavior of the system was evaluated with nominal disturbances of $T_{dy}(0) = 3 \times 10^{-5}$ ft-lb and $T_{dy}(j\omega_0) = 4 \times 10^{-5}$ ft-lb. The results are summarized in Table III-2 with comparable results derived by the preceding analytical procedures.* The close agreement between the analysis and the simulation is not

	Simulation Data		Analytical Data*	
	$\theta(0)$	$\theta(j\omega_0)$	$\theta(0)$	$\theta(j\omega_0)$
Nominal Disturbance	0.49°	0.26°	0.50°	0.26°
Twice Nominal Disturbance	1.01°	0.51°	1.00°	0.52°

*Note that Figure III-4 is based upon $\omega_0 = 0.001$ rad/sec

Table III-2 Steady-State Performance

*Analyses conducted subsequent to this simulation study indicate that more realistic disturbance estimates are $T_{dy}(0) = .000016$ ft-lb and $T_{dy}(j\omega_0) = .00012$ ft-lb. The corresponding performance is $\theta(0) = 0.27^\circ$, $\theta(j\omega_0) = 0.78^\circ$.

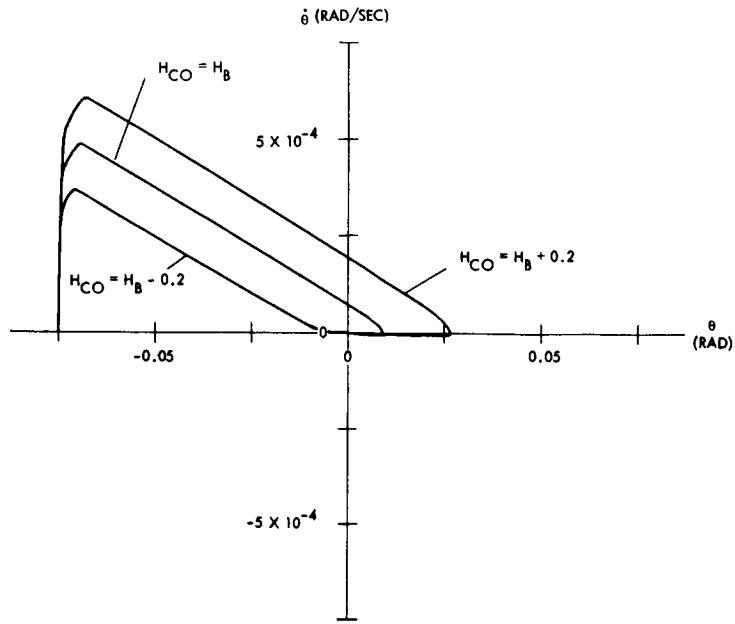


Figure III-9 Transient Response as a Function of Initial Reaction Wheel Momentum

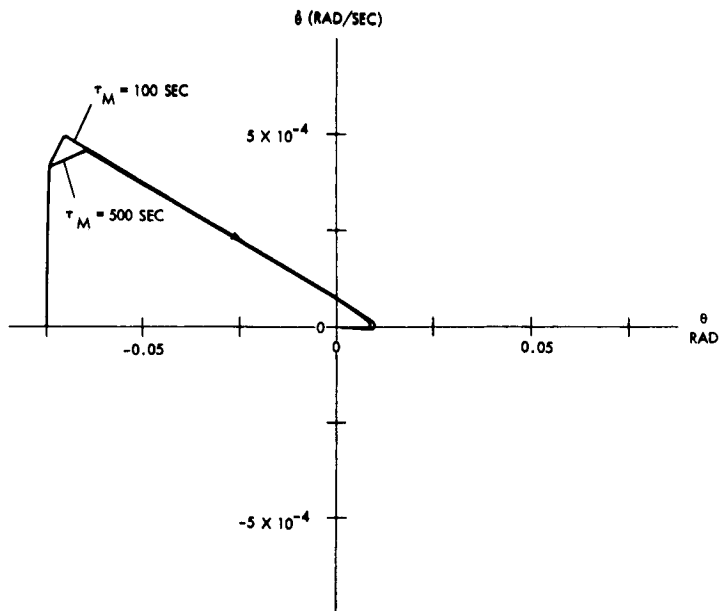


Figure III-10 Effect of Motor Windage Level upon Transient Response

surprising, even though the analysis approximated the modulator as a linear element. This is because the modulator will, for sufficient wheel torque levels, act as a high gain element and maintain its input signal at zero. Thus the precise character of the high gain element is not important, and moderate gain variations and changes in the shape of its input/output characteristic will have little effect upon the steady-state behavior of the system. Note, however, that this result applies only in the case where biasing of the wheel produces a windage torque to hold the error signal at the modulator deadband in spite of attitude perturbations due to periodic disturbances. In cases where the wheel momentum is not biased it should be possible to achieve a similar result by applying an appropriate attitude bias signal (θ_c) by ground command.

Transient response was also observed during the runs with disturbances. The time to reach the neighborhood of the deadband was relatively short (since the fast mode is dominant). Subsequent convergence to the steady motion required an additional two to three orbits; however, the important factor is the time required for the attitude error to be reduced to an acceptable level (i.e., the modulator deadband).

2. Integral Tachometer Feedback

Figure III-11 shows the transient response of the system with integral tachometer feedback ($K_I = 0.1 K_F$, $K_F = 10^{-4} \text{ sec}^{-1}$) both with and without the 10/1 lead-lag network in the attitude error feedback path.* Clearly the lead-lag network is necessary, even though it will produce an undesirable amplification of any sensor

*This value of K_I was chosen on the basis of steady-state analyses similar to those presented earlier.

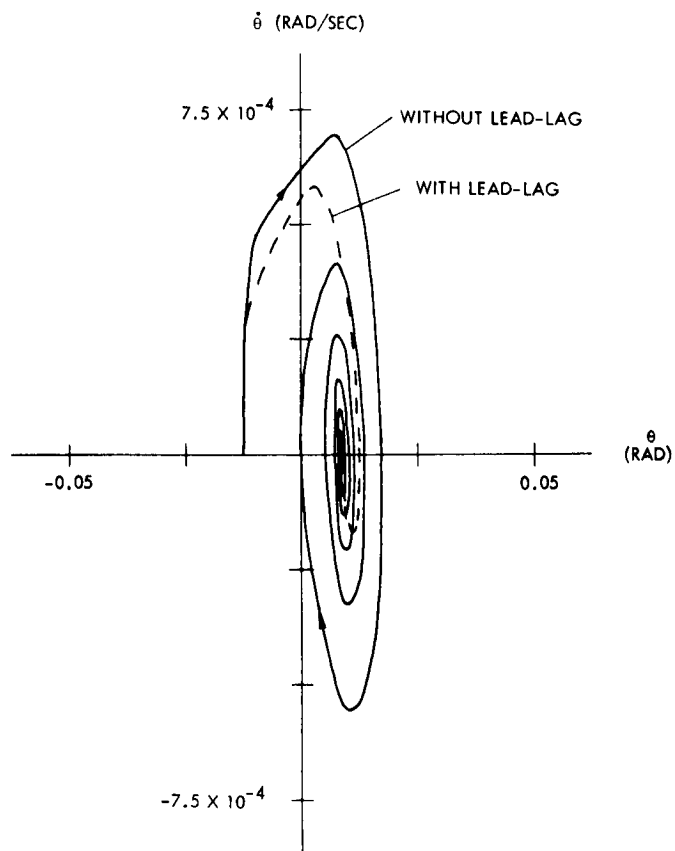


Figure III-11 Transient Response with Integral Tachometer Feedback

noise. Extreme limiting of the excursions in H_C (for example, by setting H_D equal to $0.05 H_B$) will also prevent these oscillations; however, this measure is also undesirable.

The steady-state behavior was evaluated under conditions similar to those under which proportional tachometer feedback was evaluated. The constant and orbit rate attitude variations with the previously defined nominal disturbances were 0.49° and 0.02° , respectively. Note that this compensation scheme gives considerably improved performance in the face of periodic disturbances. However, this is at the expense of transient performance and will be of value only if large periodic disturbances are expected (i.e., on the order of 5×10^{-4} ft-lb), or if the orbital frequency attitude motions which occur with proportional tachometer compensation are incompatible with the mission requirements.

3. Hybrid Tachometer Compensation

Several analog runs were made with $K_i = 0.1 K_f$ and varying values of K_{τ} (from 0 to 0.1), and with the lead-lag network. The limiting cases were quite similar to those of Figures III-8 and III-11, and the intermediate cases comprised a smooth transition between these extremes. The effect upon steady-state performance was similar; that is, as K_{τ} was increased the orbital frequency response increased. It is of interest to note that with $K_{\tau} = 0.1$ rad/ft-lb-sec, the introduction of integral feedback has no appreciable effect upon steady-state performance, although the time required to settle is increased.

APPENDIX IV

ROLL/YAW FINE CONTROL STUDY

A. INTRODUCTION

This appendix presents the results of a linearized performance study of the SAGS roll/yaw control system. As discussed in the SAGS First Quarterly Report (Reference 1), the SAGS control system utilizes a reaction wheel which is gimballed about the satellite's roll and/or yaw axis. Relative motion between the reaction wheel and satellite is coupled by a spring and damped (in this analysis) by a proportional damper. The specific objective of this study is an evaluation of the steady-state accuracy of the roll/yaw control system under the presence of normal mode disturbances.

This appendix includes a review of a previously reported preliminary analysis of the roll/yaw performance of SAGS. This study led to the selection of the gimbal configuration of the reaction wheel, the selection of control system parameters, and a determination of the parameter requirements for roll/yaw stability. To complete the analysis, the disturbance torques on satellite are evaluated for a specified set of system parameters. With a knowledge of both the disturbance torques and the system gain/frequency characteristics, the steady-state pointing errors of the roll/yaw control system are evaluated.

B. GENERAL PERFORMANCE CONSIDERATIONS

In this section, relations for evaluating the performance of the roll/yaw control system are developed. The basis for the analysis is the set of linearized equations of motion developed in Reference 1

for the "Roll-Yaw," "Yaw-Roll," "Roll," and "Yaw" gimbal configurations. As shown in Figure IV-1, the Roll-Yaw and Yaw-Roll configurations have two degrees of freedom for damping librations of the satellite, whereas the Roll and Yaw configurations have but a single gimbal. Fixing the inner set of gimbals with an "infinitely" stiff spring reduces the Roll-Yaw or Yaw-Roll configuration to the Roll or Yaw configurations, respectively. Thus the single gimbal configurations are considered a subclass of the two gimbal configurations.

In general, the small angle equations of motion for the Roll-Yaw or Yaw-Roll configurations can be reduced to the following matrix equations:

$$\begin{bmatrix} r_{11}(s) & \dots & r_{15}(s) \\ \cdot & & \cdot \\ \cdot & & \cdot \\ \cdot & & \cdot \\ r_{51}(s) & \dots & r_{55}(s) \end{bmatrix} \begin{bmatrix} \phi(s) \\ \theta(s) \\ \psi(s) \\ \gamma_x(s) \\ \gamma_z(s) \end{bmatrix} = \begin{bmatrix} T_{dx}(s) \\ T_{dy}(s) \\ T_{dz}(s) \\ T_{d4}(s) \\ T_{d5}(s) \end{bmatrix} \quad (\text{IV-1})$$

where ϕ, θ, ψ = attitude errors about the roll, pitch and yaw axis, respectively;

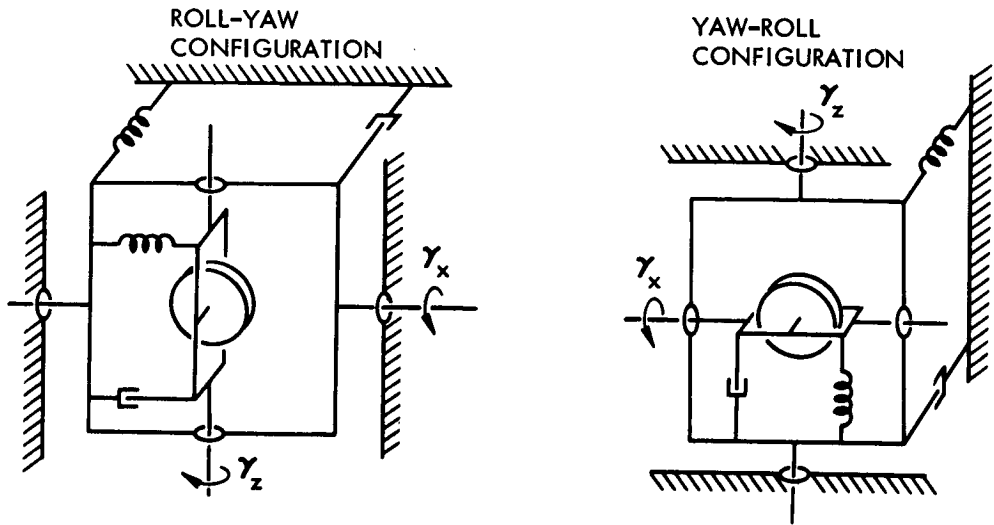
γ_x, γ_z = Gimbal roll and yaw angles, respectively;

T_{dx}, T_{dy}, T_{dz} = Main body disturbance torque components;

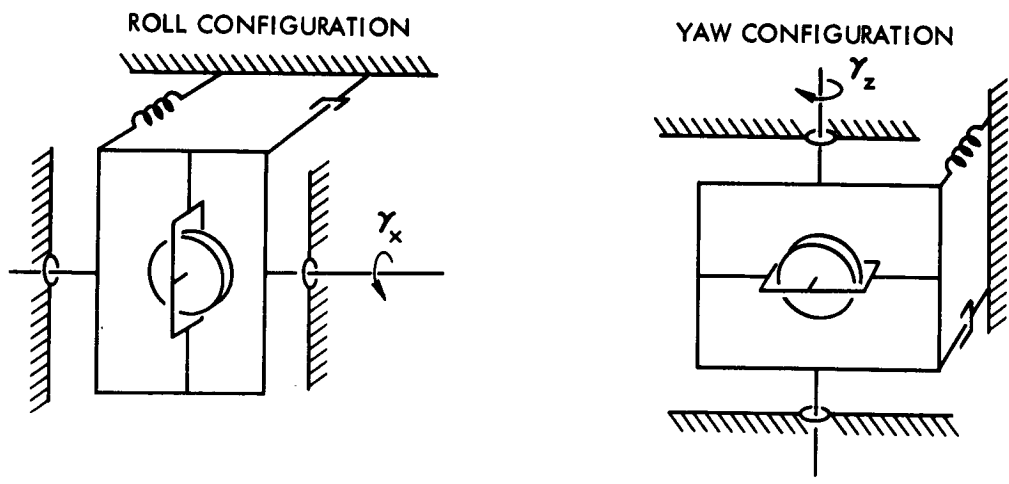
T_{d4}, T_{d5} = Gimbal disturbance torques;

s = LaPlace transform operator.

(A) TWO GIMBAL REACTION WHEEL CONFIGURATION



(B) SINGLE GIMBAL REACTION WHEEL CONFIGURATION






NOTE:
 SPRING
 DAMPER
 MAIN BODY

Figure IV-1 Gimbaled Reaction Wheel Configurations

and r_{ij} are elements of a 5×5 matrix $[r_{ij}]$ which is defined in Appendix VII of Reference 1.

By normalizing the system equations with respect to $\omega_o^2 J_{yy1}$ and performing a matrix inversion, Equation (IV-1) can be written as

$$\begin{bmatrix} \phi(p) \\ \theta(p) \\ \psi(p) \\ r_x(p) \\ r_z(p) \end{bmatrix} = \frac{1}{\omega_o^2 J_{yy1}} \begin{bmatrix} t_{11}(p) & \dots & t_{15}(p) \\ \cdot & & \cdot \\ \cdot & & \cdot \\ \cdot & \dots & \cdot \\ t_{51}(p) & \dots & t_{55}(p) \end{bmatrix} \begin{bmatrix} T_{dx}(p) \\ T_{dy}(p) \\ T_{dz}(p) \\ T_{d4}(p) \\ T_{d5}(p) \end{bmatrix} \quad (IV-2)$$

where

$$p = s/\omega_o$$

$$\omega_o = \text{Orbital angular velocity}$$

$$J_{yy1} = \text{Main body moment of inertia about the pitch axis.}$$

Because the system is linear, the matrix $[r_{ij}]$ (and thus $[t_{ij}]$) determines the gain and transient characteristics of the control system; thus the performance characteristics can be evaluated from a knowledge of the elements t_{ij} . On the other hand, the steady-state pointing errors require a knowledge of both the system gain characteristics $[t_{ij}(p)]$ and the disturbance torques as indicated by Equation (IV-2).

C. PRELIMINARY PERFORMANCE ASSESSMENTS

In this section attention is focused on the frequency response and stability of the roll/yaw control system. Dependent upon

elements of matrix $[r_{ij}]$, the system's frequency response and stability are affected primarily by (i) the gimbal configuration selected for the reaction wheel suspension, and (ii) the values selected for the suspension parameters. As a result, the gimbal configuration and the control system parameters are selected on the basis of achieving desirable gain/frequency characteristics and insuring system stability.

1. Preliminary Results

In Reference 1, a preliminary study was conducted to determine the effects of gimbal configurations and control system parameters on the system performance. This study was based on assumptions which neglected small terms in the system equations (e.g., the satellite products of inertia, wheel mass, and gimbal inertias). Moreover, the main body roll and pitch inertias for SAGS were assumed to be equal and the yaw inertia was considered negligible ($J_{yy1} = J_{xx1} \gg J_{zz1} \approx 0$).

Those assumptions not only decouple pitch motion from roll/yaw motion but also simplify the resulting error/torque gain expressions of Equation (IV-2). Reproduced in Tables IV-1 and IV-2, the gain expressions at zero and orbit rate frequencies are found to be functions of normalized control parameters, defined as follows:

$$\beta_1 = \frac{k_1}{\omega_o^2 J_{yy1}} \quad (i = x, z)$$

Zero Frequency Gain	Two Gimbal Wheel System	Single Gimbal Wheel System	
		Roll Config.	Yaw Config.
$\frac{ \phi(o) }{ T_{dx}(o)/\omega_o^2 J_{yy1} }$	$\frac{m + \beta_x}{4m + \beta_x(4+m)}$	$\frac{m + \beta_x}{4m + \beta_x(4+m)}$	$\frac{1}{4 + m}$
$\frac{ \phi(o) }{ T_{dz}(o)/\omega_o^2 J_{yy1} } *$	0	0	0
$\frac{ \psi(o) }{ T_{dz}(o)/\omega_o^2 J_{yy1} }$	$\frac{m + \beta_z}{m\beta_z}$	$\frac{1}{m}$	$\frac{m + \beta_z}{m\beta_z}$
$\frac{ r_x(o) }{ T_{dx}(o)/\omega_o^2 J_{yy1} }$	$\frac{m}{4m + \beta_x(4+m)}$	$\frac{m}{4m + \beta_x(4+m)}$	dna
$\frac{ r_x(o) }{ T_{dz}(o)/\omega_o^2 J_{yy1} }$	0	0	dna
$\frac{ r_z(o) }{ T_{dz}(o)/\omega_o^2 J_{yy1} }$	$\frac{1}{\beta_z}$	dna	$\frac{1}{\beta_z}$
$\frac{ r_z(o) }{ T_{dx}(o)/\omega_o^2 J_{yy1} }$	0	dna	0

*Note:
$$\frac{|\phi(j\omega)|}{|T_{dz}(j\omega)/\omega_o^2 J_{yy1}|} = \frac{|\psi(j\omega)|}{|T_{dx}(j\omega)/\omega_o^2 J_{yy1}|}$$

Table IV-1 Roll/Yaw Gain Expressions at Zero Frequency

Zero Frequency Gain	Two Gimbal Wheel System	Single Gimbal Wheel System	
		Roll Config.	Yaw Config.
$\frac{ \phi(j\omega_o) }{ T_{dx}(j\omega_o)/\omega_o^2 J_{yy1} }$	$\frac{1}{3}$	$\frac{1}{3}$	$\frac{1}{3}$
$\frac{ \phi(j\omega_o) }{ T_{dz}(j\omega_o)/\omega_o^2 J_{yy1} }$	$\frac{1}{3}$	$\frac{1}{3}$	$\frac{1}{3}$
$\frac{ \psi(j\omega_o) }{ T_{dz}(j\omega_o)/\omega_o^2 J_{yy1} }$	$\frac{1}{3m} \sqrt{\frac{A_1}{A_2}}^*$	$\frac{1}{3m} \sqrt{\frac{A_3}{\beta_x^2 + \alpha_x^2}}$	$\frac{1}{3m} \sqrt{\frac{A_4}{\beta_z^2 + \alpha_z^2}}$
$\frac{ r_x(j\omega_o) }{ T_{dx}(j\omega_o)/\omega_o^2 J_{yy1} }$	0	0	dna
$\frac{ r_x(j\omega_o) }{ T_{dz}(j\omega_o)/\omega_o^2 J_{yy1} }$	$\frac{1}{\sqrt{\beta_x^2 + \alpha_x^2}}$	$\frac{1}{\sqrt{\beta_x^2 + \alpha_x^2}}$	dna
$\frac{ r_z(j\omega_o) }{ T_{dz}(j\omega_o)/\omega_o^2 J_{yy1} }$	$\frac{1}{\sqrt{\beta_z^2 + \alpha_z^2}}$	dna	$\frac{1}{\sqrt{\beta_z^2 + \alpha_z^2}}$
$\frac{ r_z(j\omega_o) }{ T_{dx}(j\omega_o)/\omega_o^2 J_{yy1} }$	0	dna	0

*Note:

$$A_1 = [(3+m)(\beta_x \beta_z - \alpha_x \alpha_z) + 3m(\beta_x + \beta_z)]^2 + [(3+m)(\alpha_x \beta_z + \alpha_z \beta_x) + 3m(\alpha_x + \alpha_z)]^2$$

$$A_2 = (\beta_x^2 + \alpha_x^2)(\beta_z^2 + \alpha_z^2); A_3 = [(3+m)\beta_x + 3m]^2 + [(3+m)\alpha_x]^2$$

$$A_4 = [(3+m)\beta_z + 3m]^2 + [(3+m)\alpha_z]^2$$

Table IV-2 Roll/Yaw Gain Expressions at Orbital Frequency

$$\alpha_i = \frac{c_i}{\omega_o J_{yy1}} \quad (i = x, z)$$

$$m = \frac{H_o}{\omega_o J_{yy1}}$$

where k_i = Gimbal spring constant,
 c_i = Proportional damping coefficient,
 H_o = Bias momentum.*

Table IV-2 indicates that the orbit rate gains are not significantly affected by the suspension configuration chosen. However, the zero frequency gains of Table IV-1 show that gain errors due to steady yaw disturbances are very sensitive to the value chosen for β_z for either of the suspension systems possessing a yaw degree of freedom. In this case, the d-c yaw gain becomes unacceptably large for small spring constants ($k_z \ll \omega_o^2 J_{yy1}$). Increasing the spring constant to higher values ($k_z > \omega_o^2 J_{yy1}$) will reduce the yaw gain but may seriously degrade the transient response of the system, as evidenced in a previous parameter study (Reference IV-1). On the other hand, the d-c yaw gain of the Roll configuration is independent of the spring constant β_x and is reasonably small for nominal values of the wheel's angular momentum ($H_o > \omega_o J_{yy1}$). Thus, from a low frequency performance standpoint, a single gimbal Roll wheel system is superior to either a two gimbal wheel system or a single gimbal yaw system.

*In this discussion positive bias momentum H_o adds to the angular momentum of the satellite. That is, with the gimbal undeflected $\bar{H}_c = -H_o \bar{y}_b$. With reference to the notation in the foregoing acquisition discussion $H_o = -H_c$.

To assess the effects of the control system parameters on the gain characteristics about the roll and yaw axes, the preliminary study utilized a TRW On-Line Computer. The specific objective of the On-Line Computer program was to obtain a range of control parameters which gave reasonable error/torque gains for the Roll gimbal system. In particular, the frequency characteristics at orbital harmonics were especially scrutinized because the most significant disturbance torques are at these frequencies. The On-Line study resulted in the following recommended range of spring constants and damping coefficients:

$$0 < k_x \leq .5 \omega_o^2 J_{yy1}$$

$$\omega_o J_{yy1} \leq c_x \leq 2\omega_o J_{yy1}$$

In Figure IV-2, the above ranges of control parameters are plotted as functions of pitch inertia for a SAGS satellite orbiting at a nominal altitude of 750 nautical miles.

The preliminary study also investigated the stability requirements for a two gimbal wheel system. It was shown that for the desired orientation to be asymptotically stable (in the small) the bias momentum H_o must satisfy the following conditions:

$$(i) \quad H_o > -4\omega_o (J_{yy1} + J_{yyc} - J_{zz1} - J_{zxc}) \quad (IV-3)$$

$$(ii) \quad H_o > -\omega_o (J_{yy1} + J_{yyc} - J_{xx1} - J_{xxc})$$

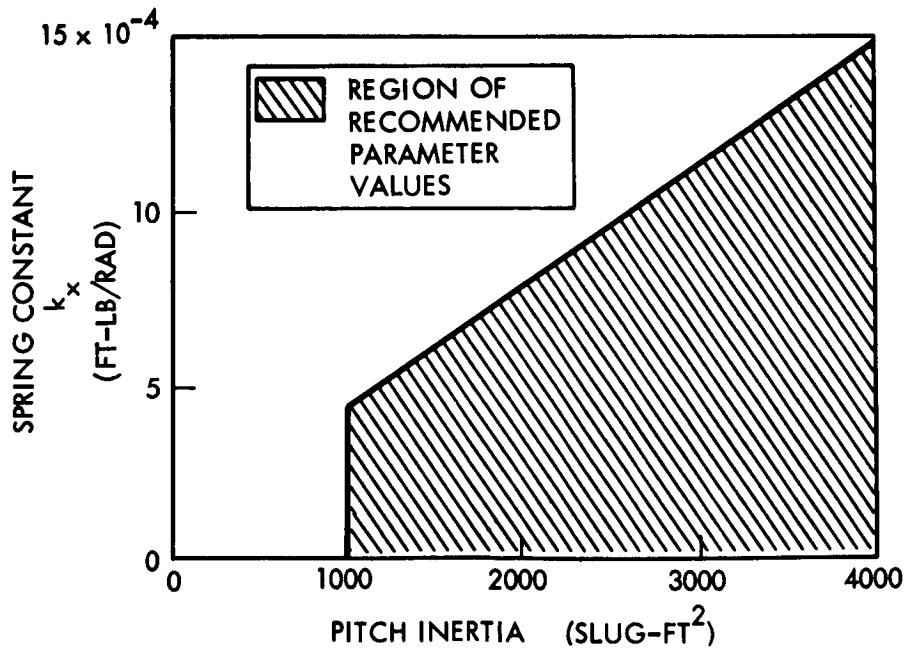
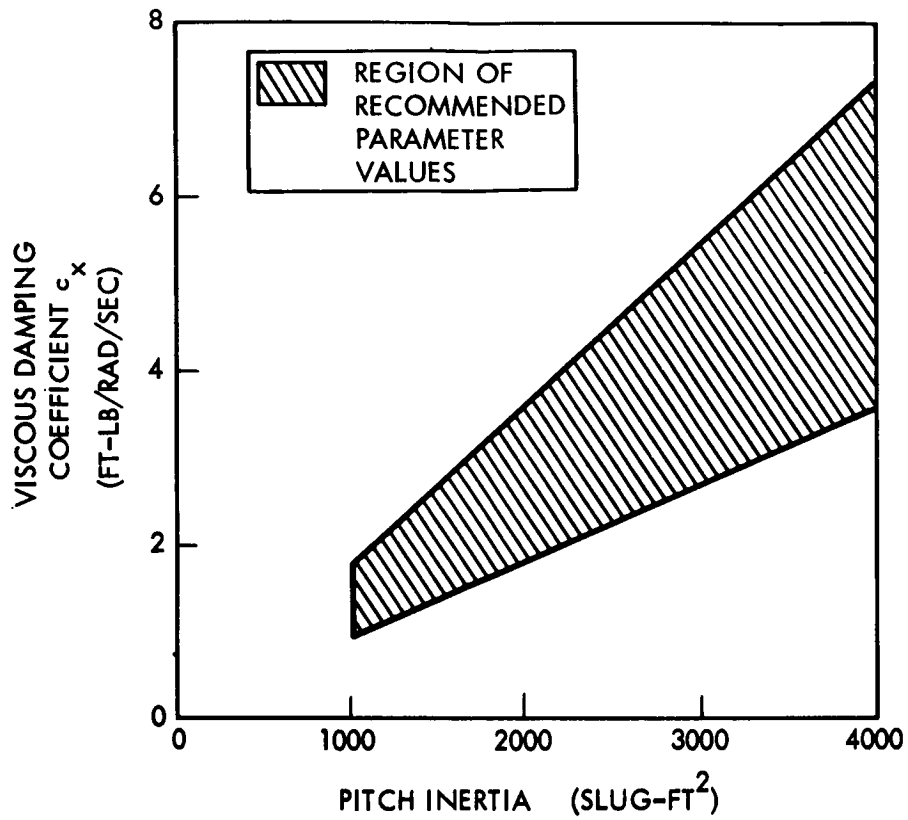


Figure IV-2 Recommended Values of Spring Constant and Damping Coefficient (Orbital Attitude = 750 n. mi.)

$$(iii) \quad H_o > - \frac{4\omega_o [\omega_o^2 (J_{yy1} - J_{zz1})(J_{yyc} - J_{zxc}) + k_x (J_{yy1} + J_{yyc} - J_{zz1} - J_{zxc})]}{k_x + 4\omega_o^2 (J_{yy1} - J_{zz1})}$$

$$(iv) \quad H_o > \frac{\omega_o [\omega_o^2 (J_{yy1} - J_{xx1})(J_{yyc} - J_{xzc}) + k_z (J_{yy1} + J_{yyc} - J_{xx1} - J_{xzc})]}{k_z + \omega_o^2 (J_{yy1} - J_{xx1})}$$

where J_{xzc} , J_{yyc} , J_{zxc} represent the inertias of the gimbal cases and are negligible in any practical situation.*

In general, the above stability conditions are met by making H_o sufficiently positive; negative values of H_o should be avoided. Suppose a Roll gimbal system is considered where

$$\frac{J_{xx1}}{J_{yy1}} = 1 \gg \frac{J_{zz1}}{J_{yy1}} \gg \frac{J_{yyc}}{J_{yy1}} > \frac{J_{xzc}}{J_{yy1}} = \frac{J_{zxc}}{J_{yy1}}$$

$$\frac{k_x}{\omega_o^2 J_{yy1}} = .5,$$

then conditions (i) through (iii) become

$$(i) \quad H_o > - 4\omega_o J_{yy1}$$

$$(ii) \quad H_o > 0$$

$$(iii) \quad H_o > .44 \omega_o J_{yy1}$$

*For the single (roll) gimbal configuration the first three conditions must be satisfied.

In this case, the critical condition is (ii). However, the On-Line Computer study recommends values of the bias momentum on the order of the orbital momentum of the satellite for acceptable yaw performance. Therefore, by setting $H_0 > \omega_0 J_{yy1}$, the control system is stable and provides desirable frequency response characteristics.

2. Digital Computer Study

The results of the previous section were based on neglecting small terms (anomalies) in the system equations to simplify the analysis. However, including anomalies such as products of inertia can affect the system response by coupling pitch motion to the roll/yaw motion of the satellite. Therefore, to extend the preliminary results to less ideal situations a digital computer program was developed.

The primary task of the computer program is to compute the elements of the matrix $[t_{ij}]$ in Equation (IV-2) and to plot the magnitude $|t_{ij}|$ as a function of the normalized frequency (ω/ω_0) . The details of the digital program are discussed in Appendix V.

In this study, the following normalized values of satellite inertias, inertia products, and gimbal inertias are considered:

$$\frac{J_{xx1}}{J_{yy1}} = 1.02,$$

$$\frac{J_{zz1}}{J_{yy1}} = .054$$

$$\frac{J_{xy1}}{J_{yy1}} = .7 \times 10^{-3},$$

$$\frac{J_{yz1}}{J_{yy1}} = 3.4 \times 10^{-3}, \quad \frac{J_{xz1}}{J_{yy1}} = -2.2 \times 10^{-3}$$

$$\frac{J_{xxc}}{J_{yy1}} = .047 \times 10^{-3}, \quad \frac{J_{yyc}}{J_{yy1}} = .08 \times 10^{-3}, \quad \frac{J_{zzc}}{J_{yy1}} = .053 \times 10^{-3}$$

$$\frac{J_{jkc}}{J_{yy1}} = 0 \quad (j, k = x, y, z; j \neq k)$$

Moreover, the mass of the gimballed reaction wheel assembly and its location relative to the center of mass of the satellite (defined as m_g and $\bar{\xi}$, respectively) were taken as

$$\frac{m_g}{J_{yy1}} = 1.11 \times 10^{-3} \text{ ft}^2$$

$$\bar{\xi} = \begin{bmatrix} 0 \\ -.39 \\ -.51 \end{bmatrix} \text{ ft}$$

The above system parameters are based on a 500 lb SAGS satellite with a 52 ft boom and 15 lb tip mass and with the reaction wheel system developed in Appendix VII. In this case the satellite has a pitch inertia J_{yy1} of 1500 slug-ft² to provide no more than .5° steady-state pitch error in the presence of expected constant disturbances (See Appendix III).

The results of the digital computer program are shown in Figures IV-3 to IV-7. In Figures IV-3a to IV-3f the roll and yaw gains for a two gimbal Roll-Yaw system are plotted against normalized frequency with the inner spring constant k_z as a parameter. It is clear that a large spring constant k_z is desirable to minimize the yaw gain characteristics. But stiffening the inner springs of the Roll-Yaw configuration simply results in the single gimbal Roll

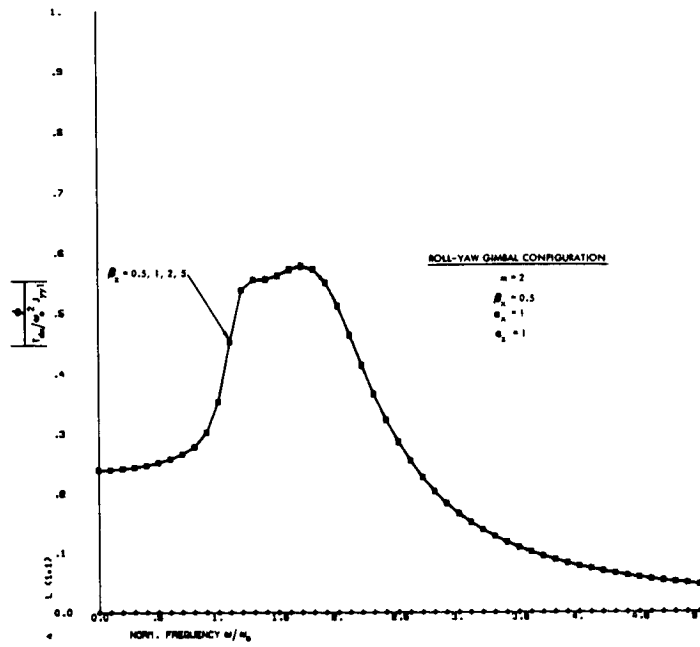


Figure IV-3a Roll Error/Roll Torque Gain (Roll-Yaw Gimbal Configuration): as a Function of Yaw Spring Constant

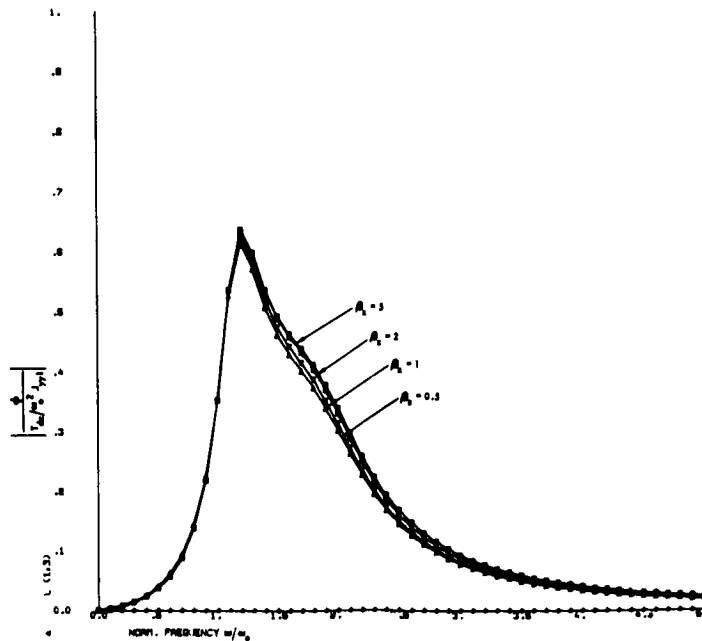


Figure IV-3b Roll Error/Yaw Torque Gain (Roll-Yaw Gimbal Configuration): as a Function of Yaw Spring Constant

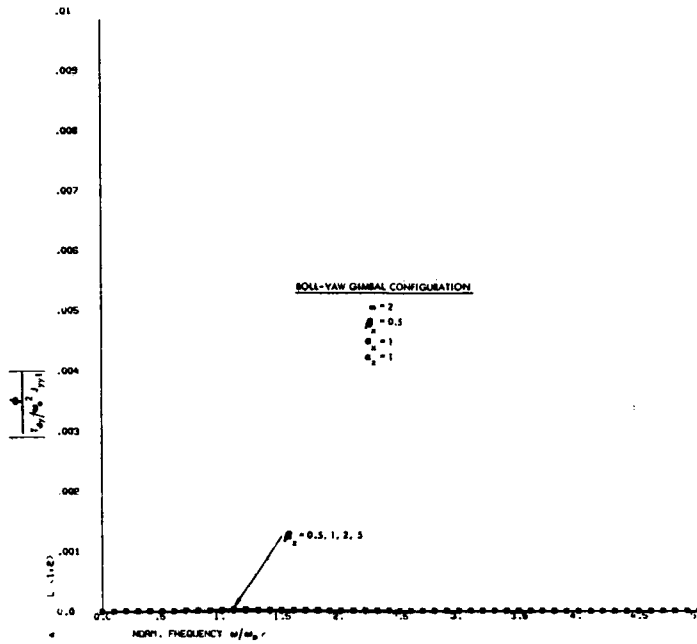


Figure IV-3c Roll Error/Pitch Torque Gain (Roll-Yaw Gimbal Configuration): as a Function of Yaw Spring Constant

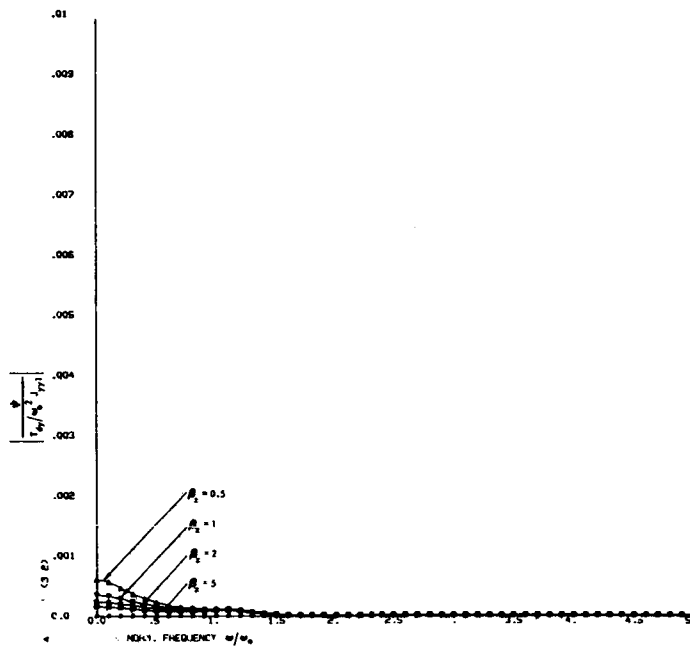


Figure IV-3d Yaw Error/Pitch Torque Gain (Roll-Yaw Gimbal Configuration): as a Function of Yaw Spring Constant

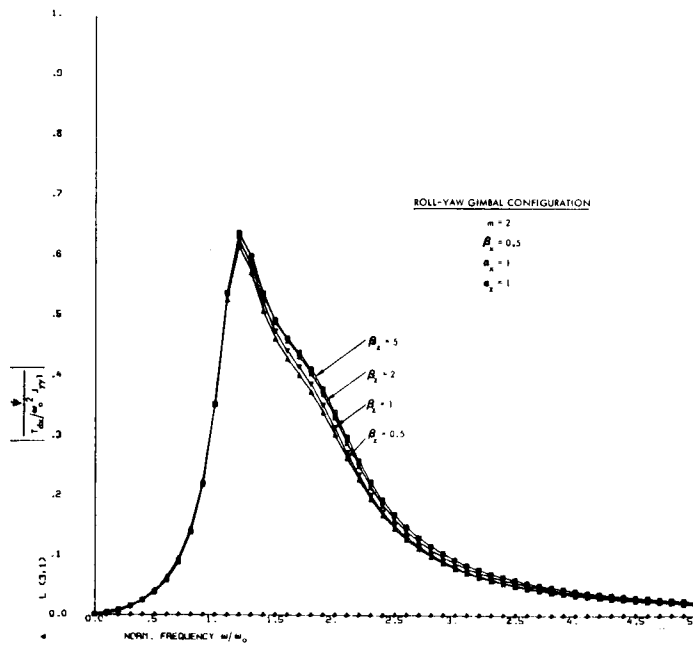


Figure IV-3e Yaw Error/Roll Torque Gain (Roll-Yaw Gimbal Configuration): as a Function of Yaw Spring Constant

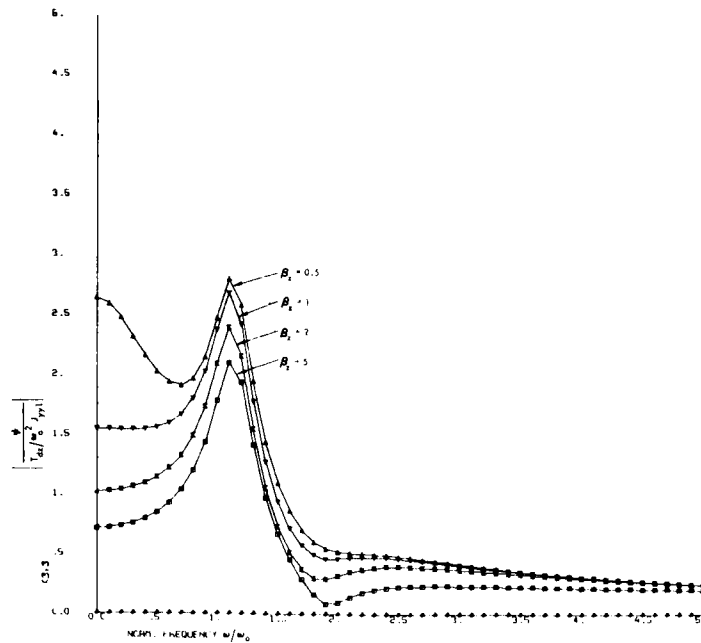


Figure IV-3f Yaw Error/Yaw Torque Gain (Roll-Yaw Gimbal Configuration): as a Function of Yaw Spring Constant

configuration. Moreover, the gain characteristics of the Yaw-Roll, and Roll-Yaw gimbal system are found to be comparable. These facts verify the preliminary results which noted the advantages of the Roll gimbal configuration over the two-gimbal configurations.

In Figures IV-4a to IV-4f, the roll and yaw gains of the Roll and Yaw Gimbal configurations are compared. It is evident that the yaw configuration exhibits significantly larger yaw gains. Moreover, the frequency response of the Yaw gimbal configuration has a large resonance gain near $1.35 \omega_0$. A large resonance peak is undesirable for it implies that the control system is highly underdamped. Reducing the spring constant decreases the gain at the resonant frequency but at the expense of increasing the d-c gains. Therefore, to minimize the error/torque gains and to enhance transient characteristics, a Roll gimbal configuration is preferred over the Yaw configuration.

In the above figures, it is noted that the roll and yaw gains sensitive to pitch disturbance torques are several orders of magnitude smaller than those affected by roll and yaw disturbance torques. Thus, assuming that the components of the disturbance torques are of the same order of magnitude, the steady-state roll and yaw errors will not be significantly affected by pitch disturbances. Furthermore, this result implies that the roll/yaw motion and the pitch motion are not strongly coupled with the assumed products of inertia.

Finally, the digital computer study verified the range of control parameters which was recommended in the preliminary study for the Roll gimbal system. Figures IV-5a to IV-7f show the error/torque gains under variations in the spring constant ($.1 \omega_0^2 J_{yy1} \leq k_x \leq 2\omega_0^2 J_{yy1}$), damping coefficient ($.5\omega_0 J_{yy1} \leq c_x \leq 2\omega_0 J_{yy1}$), and

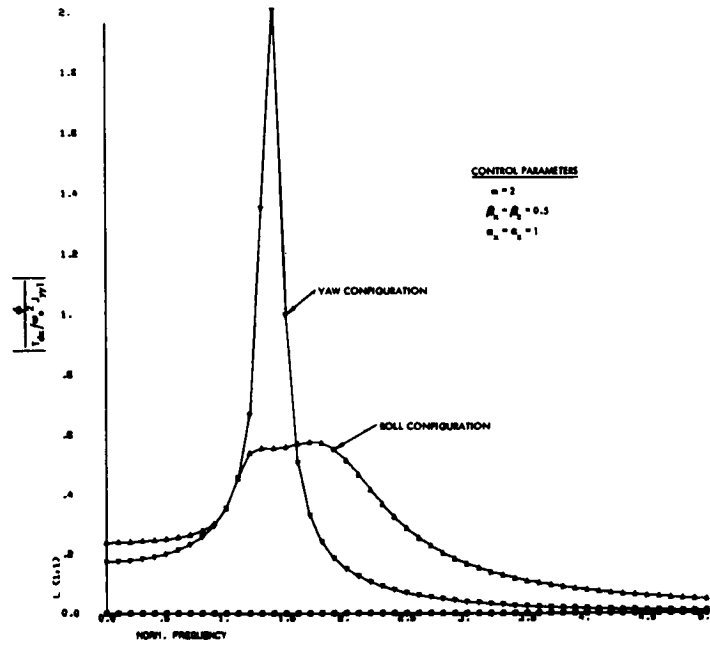


Figure IV-4a Roll Error/Roll Torque Gain
 (Single Gimbal Configurations)

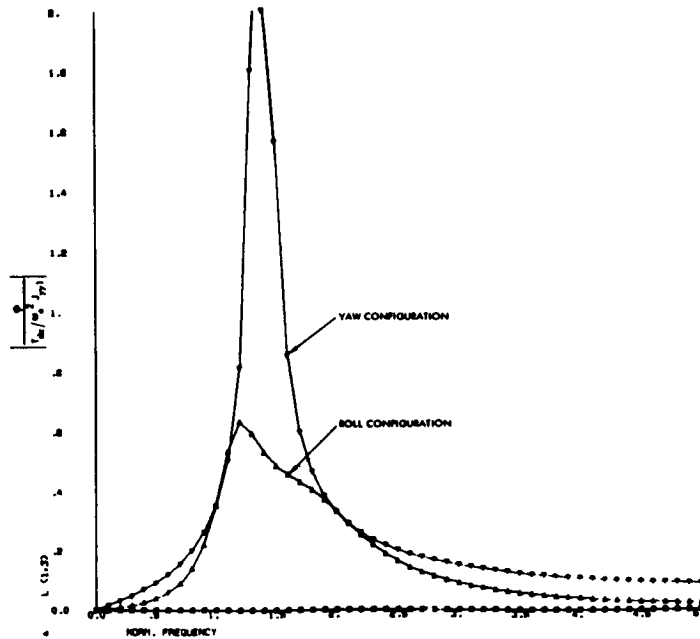


Figure IV-4b Roll Error/Yaw Torque Gain
 (Single Gimbal Configurations)

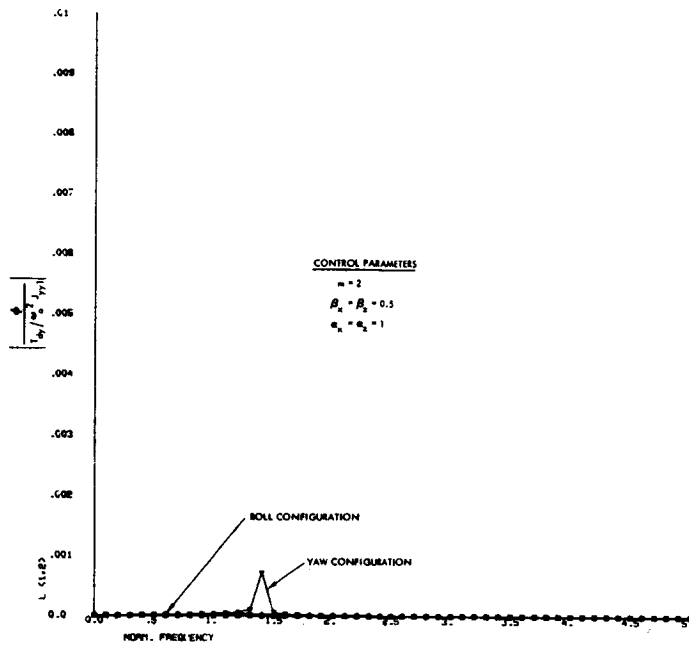


Figure IV-4c Roll Error/Pitch Torque Gain
 (Single Gimbal Configurations)

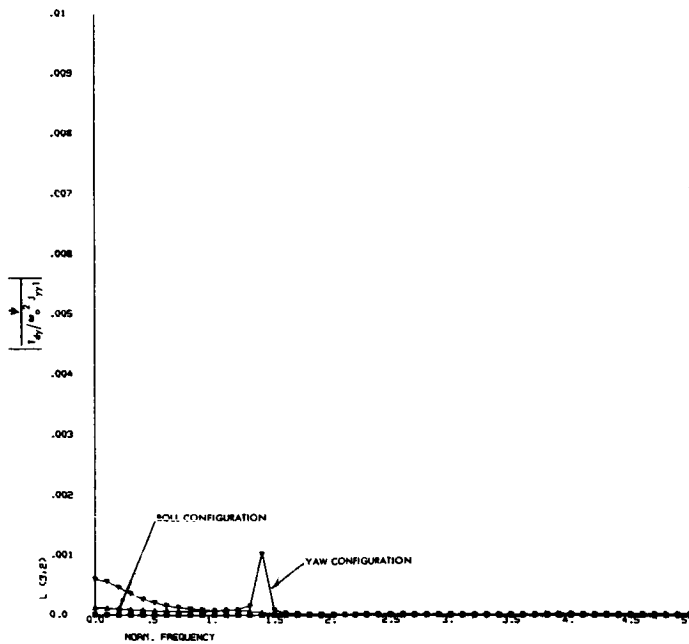


Figure IV-4d Yaw Error/Pitch Torque Gain
 (Single Gimbal Configurations)

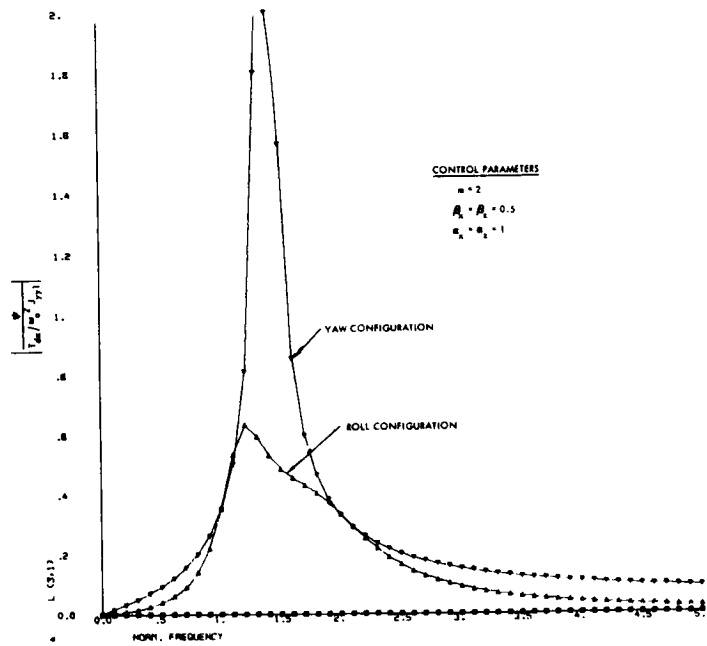


Figure IV-4e Yaw Error/Roll Torque Gain
(Single Gimbal Configurations)

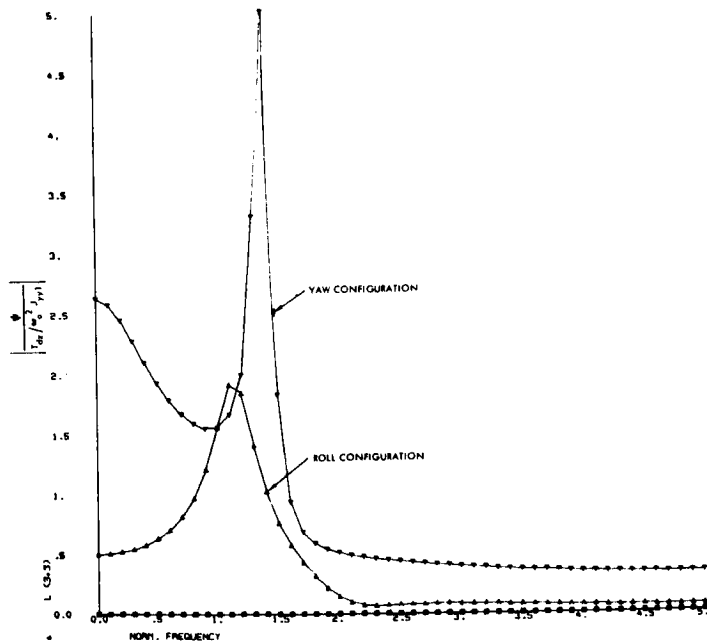


Figure IV-4f Yaw Error/Yaw Torque Gain
(Single Gimbal Configurations)

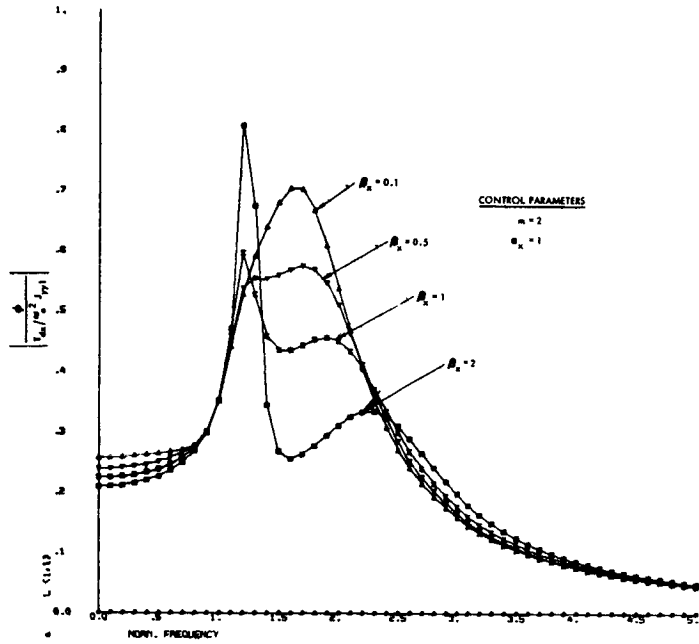


Figure IV-5a Roll Error/Roll Torque Gain (Roll Gimbal System): as a Function of Spring Constant

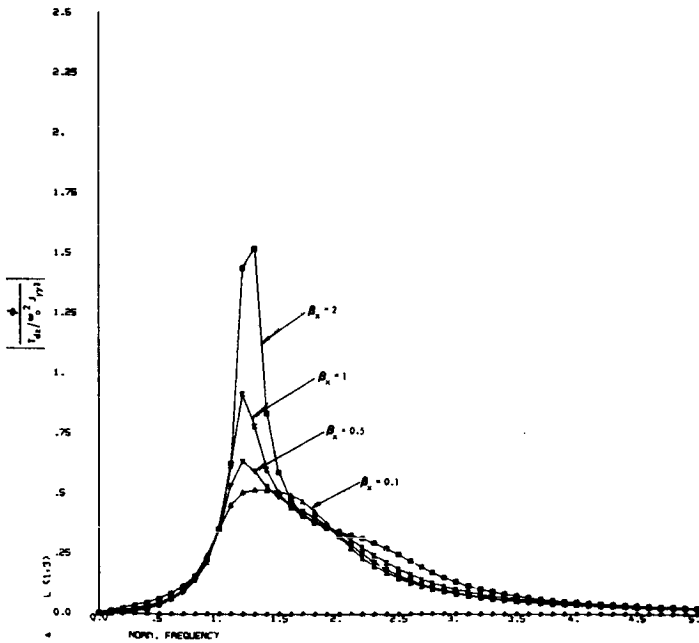


Figure IV-5b Roll Error/Yaw Torque Gain (Roll Gimbal System): as a Function of Spring Constant

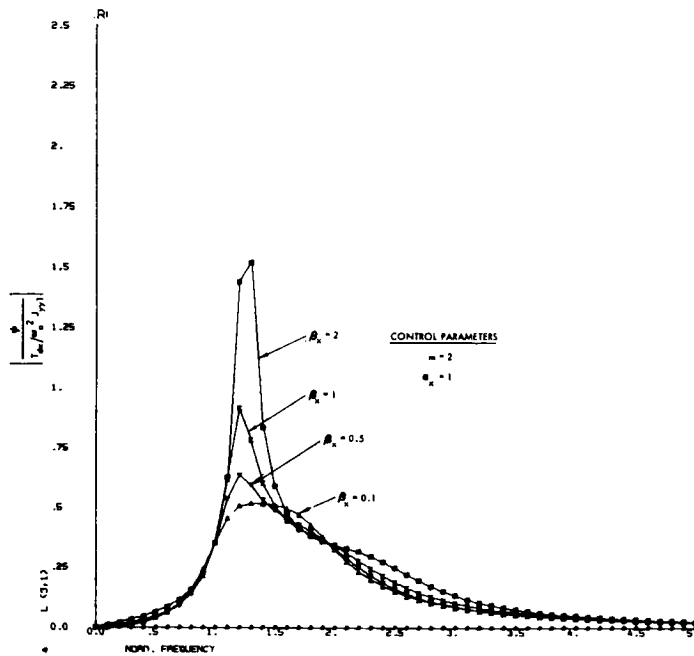


Figure IV-5c Yaw Error/Roll Torque Gain (Roll Gimbal System): as a Function of Spring Constant

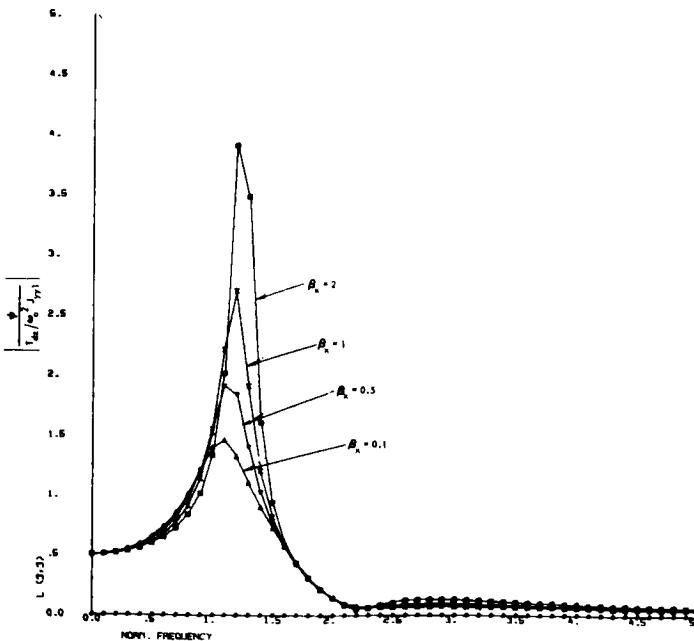


Figure IV-5d Yaw Error/Yaw Torque Gain (Roll Gimbal System): as a Function of Spring Constant

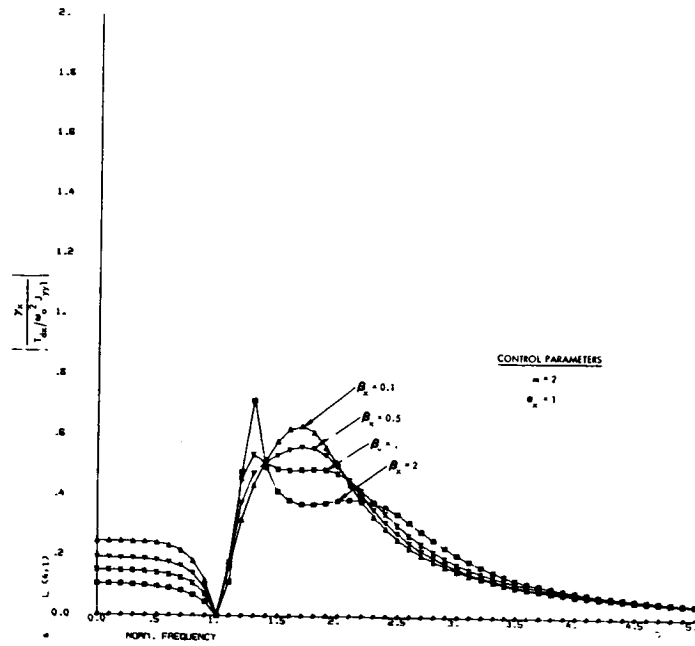


Figure IV-5e Gimbal Error/Roll Torque Gain (Roll Gimbal System): as a Function of Spring Constant

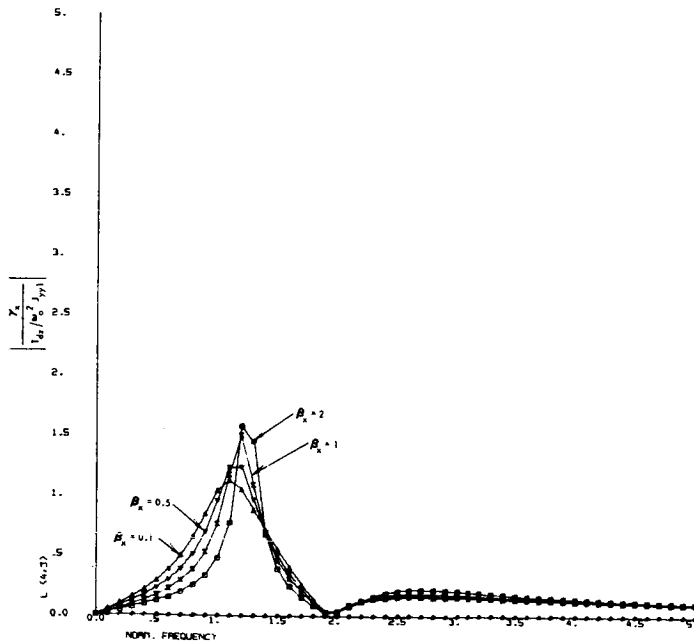


Figure IV-5f Gimbal Error/Yaw Torque Gain (Roll Gimbal System): as a Function of Spring Constant

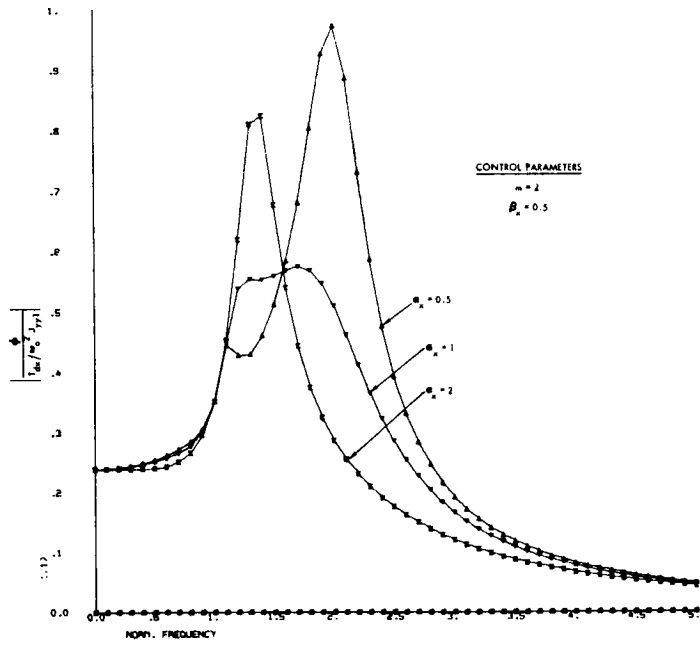


Figure IV-6a Roll Error/Roll Torque Gain (Roll Gimbal System): as a Function of Damping Coefficient

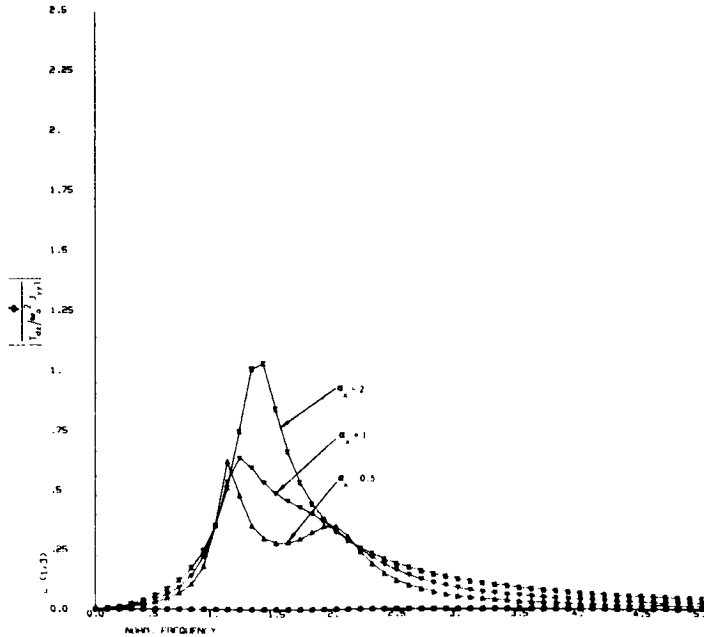


Figure IV-6b Roll Error/Yaw Torque Gain (Roll Gimbal System): as a Function of Damping Coefficient

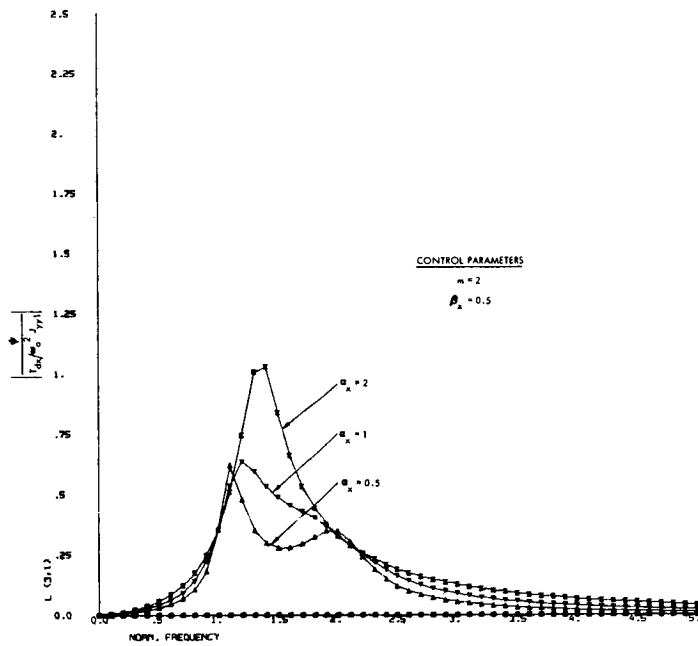


Figure IV-6c Yaw Error/Roll Torque Gain (Roll Gimbal System): as a Function of Damping Coefficient

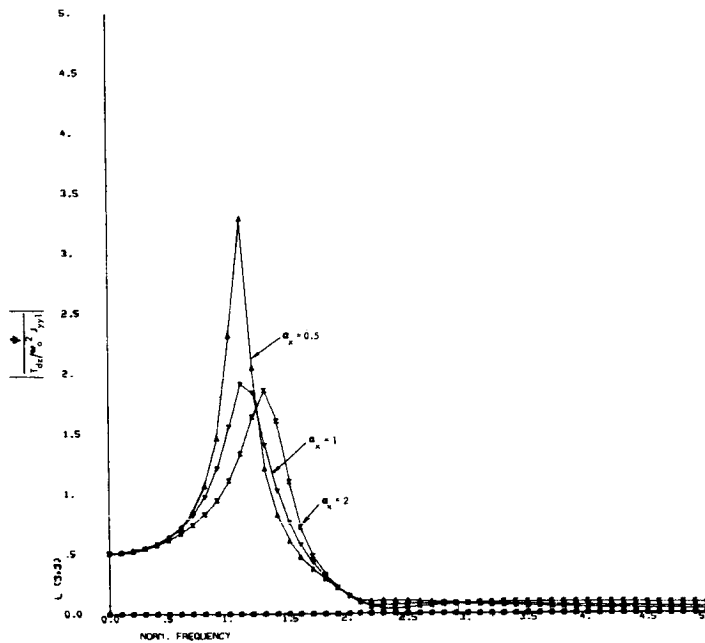


Figure IV-6d Yaw Error/Yaw Torque Gain (Roll Gimbal System): as a Function of Damping Coefficient

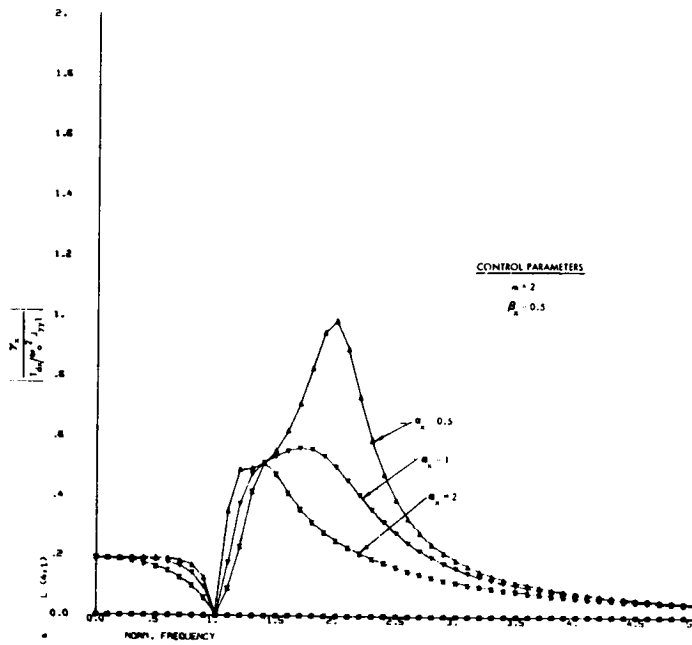


Figure IV-6e Gimbal Error/Roll Torque Gain (Roll Gimbal System): as a Function of Damping Coefficient

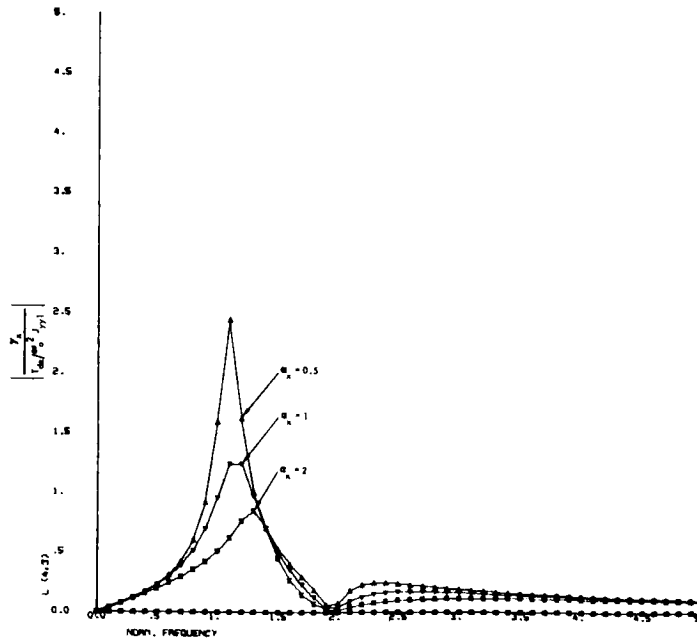


Figure IV-6f Gimbal Error/Yaw Torque Gain (Roll Gimbal System): as a Function of Damping Coefficient

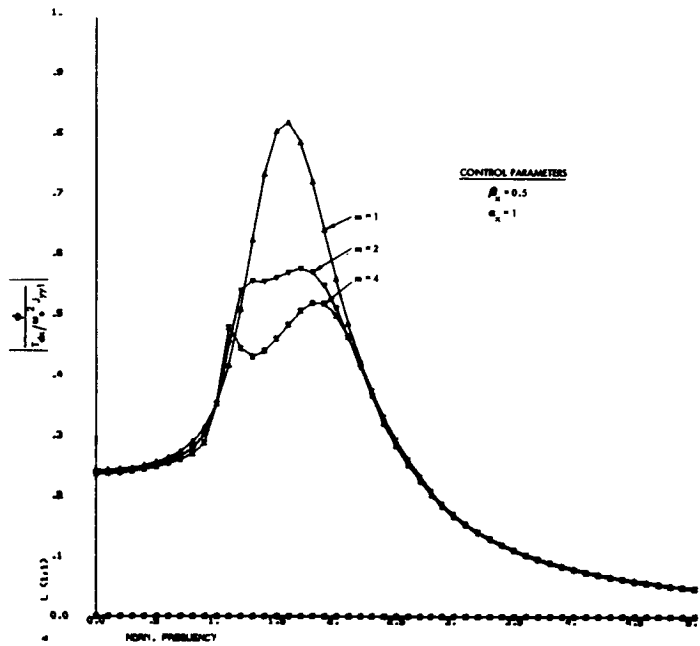


Figure IV-7a Roll Error/Roll Torque Gain (Roll Gimbal System): as a Function of Wheel Momentum

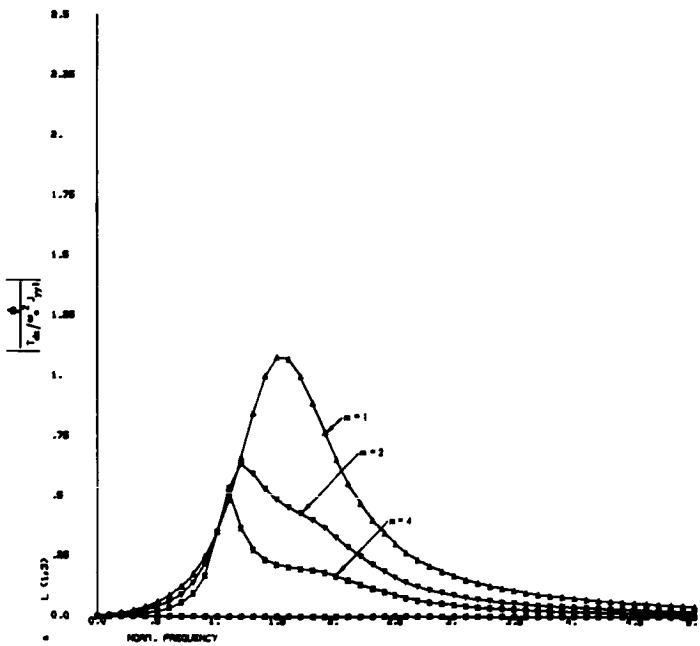


Figure IV-7b Roll Error/Yaw Torque Gain (Roll Gimbal System): as a Function of Wheel Momentum

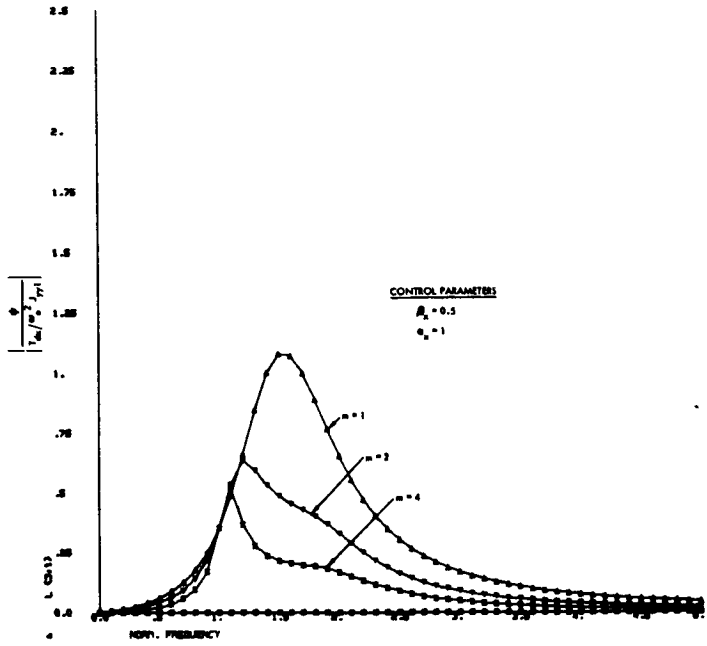


Figure IV-7c Yaw Error/Roll Torque Gain (Roll Gimbal System): as a Function of Wheel Momentum

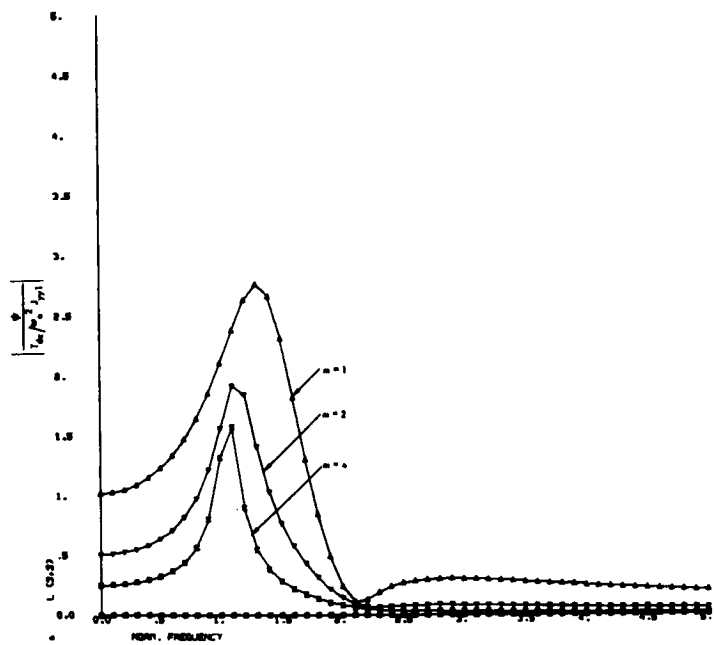


Figure IV-7d Yaw Error/Yaw Torque Gain (Roll Gimbal System): as a Function of Wheel Momentum

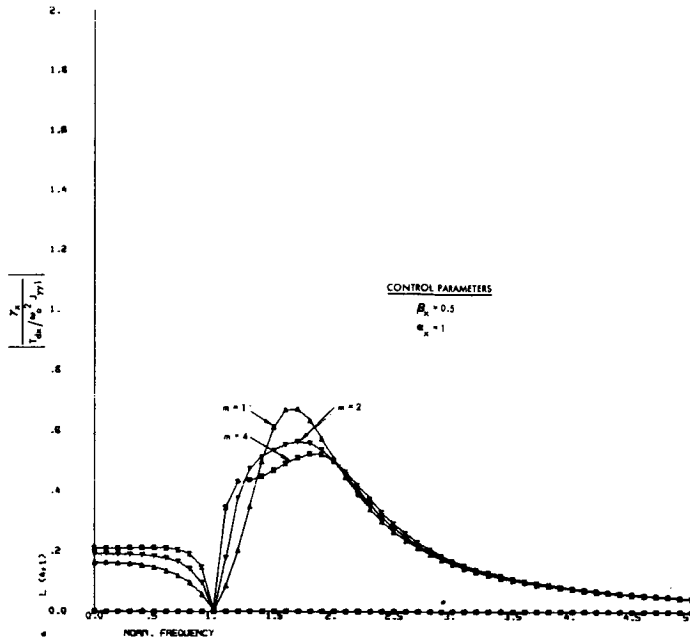


Figure IV-7e Gimbal Error/Roll Torque Gain (Roll Gimbal System): as a Function of Wheel Momentum

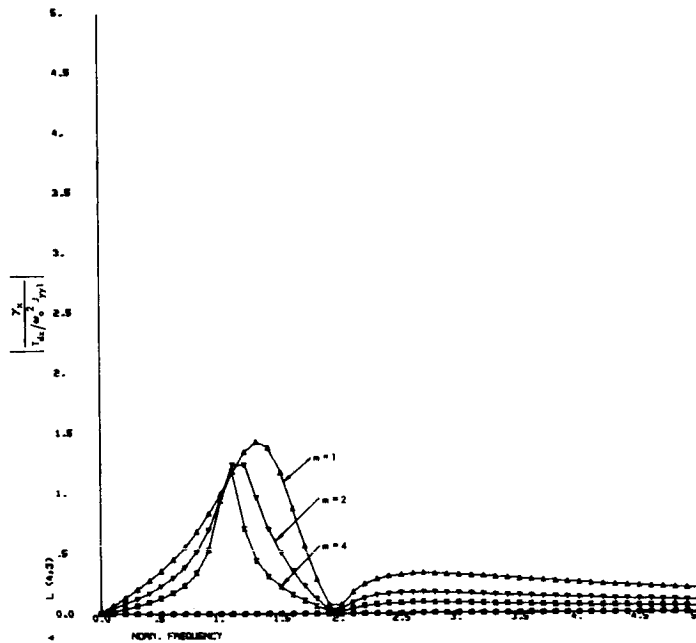


Figure IV-7f Gimbal Error/Yaw Torque Gain (Roll Gimbal System): as a Function of Wheel Momentum

bias momentum ($\omega_o J_{yy1} \leq H_o \leq 4\omega_o J_{yy1}$). These plots will be utilized in the subsequent sections to evaluate the steady-state roll and yaw control accuracies.

D. FORCED SYSTEM PERFORMANCE

1. Satellite Environmental Disturbances

In Appendix VI, a detailed study was conducted to evaluate the torques on the SAGS satellite due to environmental disturbances. The results of this disturbance torque evaluation are summarized in this section. The study is conducted for a SAGS satellite with the dimensions of Figure VI-1. The disturbance torques are determined for a satellite orbiting in a 750 nautical mile polar orbit. To vary thermal conditions, the following locations of the sun were considered:

Case I - Sun in the orbit plane

Case II - Sun normal to the orbit plane

The sources of disturbance torques considered in the study are:

- (i) Solar radiation pressure
- (ii) Thermal boom bending
- (iii) Magnetic moments
- (iv) Control axis misalignment
- (v) Orbital eccentricity

When the sun is in the orbit plane, torques due to solar radiation pressure, thermal boom bending, and magnetic moments on the solar panel are assumed to be nulled during eclipse. When the sun is normal to the orbit plane, the solar array is assumed to be fixed relative to the satellite.

Values of the system parameters which affect the disturbance torques are listed in Table VI-1. It is noted that torques due to both in-plane and out-of-plane boom bending are considered. In the table the bending coefficients are determined for a Be-Cu* boom with a diameter of .5 inch and a thickness of .002 inch. Constant as well as orbital frequency components of magnetic moment (5×10^{-5} ft-lb/gauss) are assumed to be located on the satellite. Gravitational torques resulting from misalignment of the control axes from the principal axes are based on a maximum 2 degree offset about the roll and pitch axes and a 5 degree offset about the yaw axis prior to boom extension. An orbital eccentricity of 1 percent is assumed.

Some of the environmental disturbances were obtained from a TRW Generalized Computer Program (Prog. AC-019); the remainder were analytically derived in Appendix VI. The components of the disturbance torque \bar{T}_d were expanded in a trigonometric series as follows:

$$\bar{T}_d = \begin{bmatrix} \sum_k A_{kX} \cos \omega_k t + \sum_k B_{kX} \sin \omega_k t \\ \sum_k A_{kY} \cos \omega_k t + \sum_k B_{kY} \sin \omega_k t \\ \sum_k A_{kZ} \cos \omega_k t + \sum_k B_{kZ} \sin \omega_k t \end{bmatrix} \quad (IV-4)$$

where ω_k = k-th frequency,

t = time.

For the disturbances considered, the significant frequencies are:

* A DeHavilland boom is assumed.

Solar pressure:	$\omega_k = 0, \omega_o, 2\omega_o, 3\omega_o$
Thermal bending:	$\omega_k = 0, \omega_o, 2\omega_o, 3\omega_o$
Magnetics:	$\omega_k = 0, \omega_o, \omega_o \pm \omega_e, 2\omega_o, 2\omega_o \pm \omega_e,$ $2\omega_o \pm 2\omega_e, 3\omega_o, 3\omega_o \pm \omega_e$
Misalignment:	$\omega_k = 0$
Eccentricity:	$\omega_k = \omega_o$

where ω_e represents the spin rate of the earth. Terms above $3\omega_o$ neglected since the system frequency response is well attenuated at these frequencies.

The results of the study are summarized in plots where the root-sum-squared (RSS) values of disturbance torques are presented as a function of frequency. In Figures IV-8 to IV-13, the torques due to solar radiation pressure, thermal boom bending, and magnetic moments are summed, component by component. Then the RSS values are obtained as follows:

$$\begin{aligned}
 |T_{dx}(j\omega_k)| &= \sqrt{A_{kx}^2 + B_{kx}^2} \\
 |T_{dy}(j\omega_k)| &= \sqrt{A_{ky}^2 + B_{ky}^2} \\
 |T_{dz}(j\omega_k)| &= \sqrt{A_{kz}^2 + B_{kz}^2}
 \end{aligned}
 \tag{IV-5}$$

Notice that the effects of magnetic moments are dominant in these results. Boom bending contributes significantly to the orbit rate

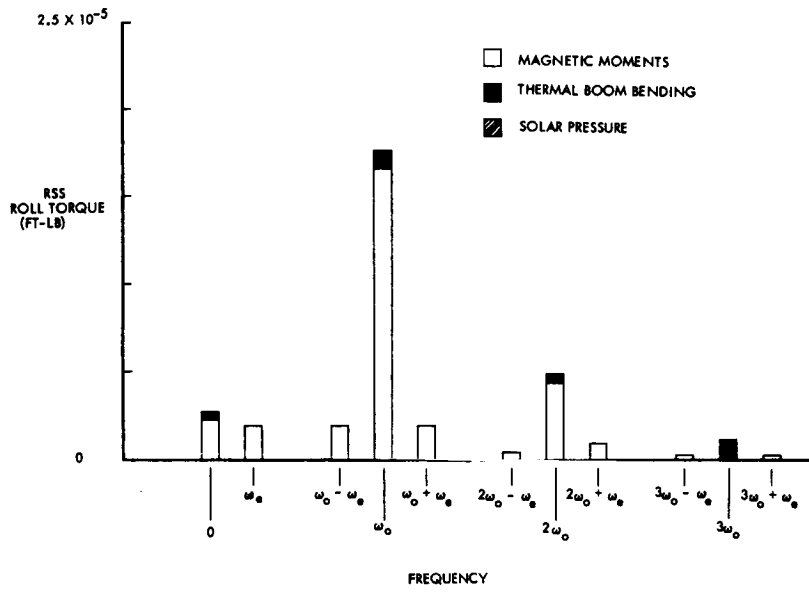


Figure IV-8 RSS Roll Torque Versus Frequency (Case I: Sun in Orbit Plane)

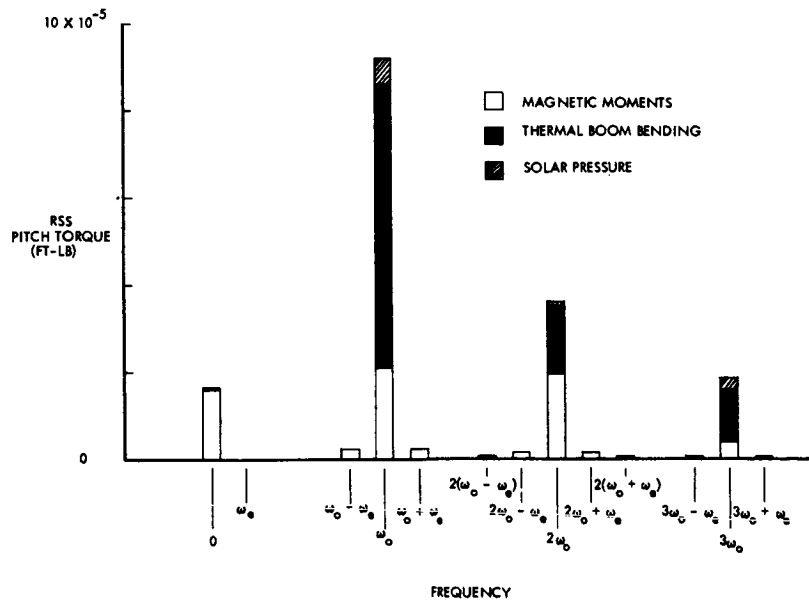


Figure IV-9 RSS Pitch Torque Versus Frequency (Case I: Sun in Orbit Plane)

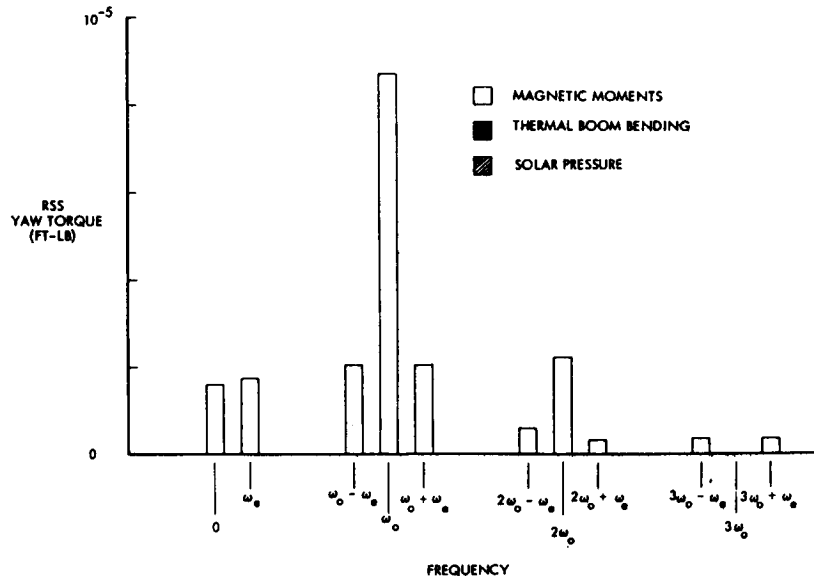


Figure IV-10 RSS Yaw Torque Versus Frequency (Case I: Sun in Orbit Plane)

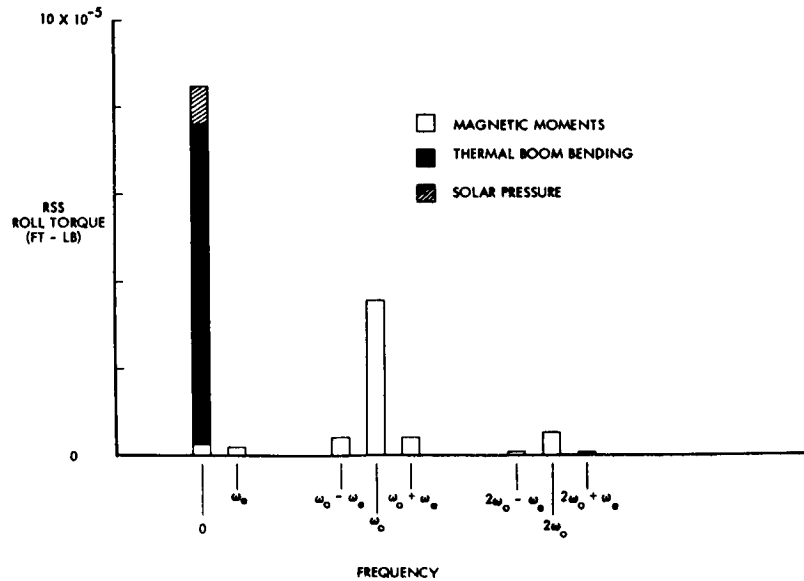


Figure IV-11 RSS Roll Torque Versus Frequency (Case II: Sun Normal to Orbit Plane)

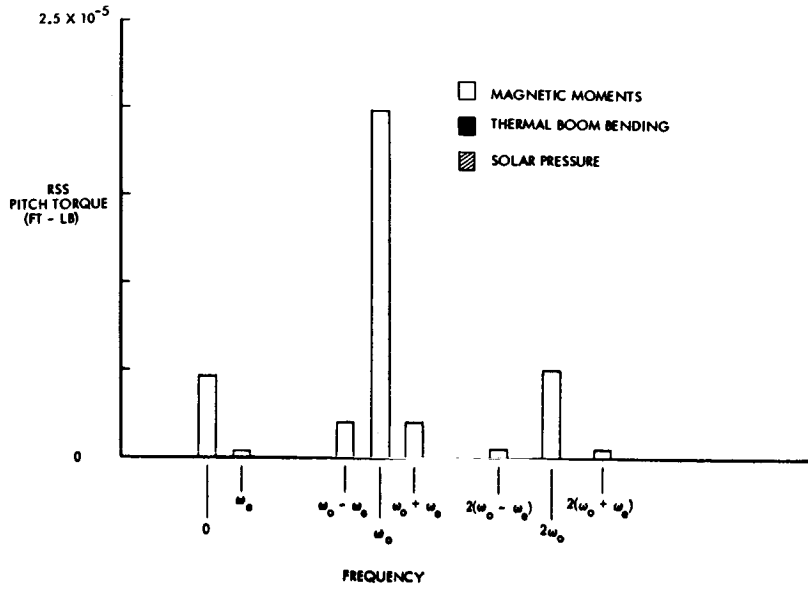


Figure IV-12 RSS Pitch Torque Versus Frequency
(Case II: Sun Normal to Orbit Plane)

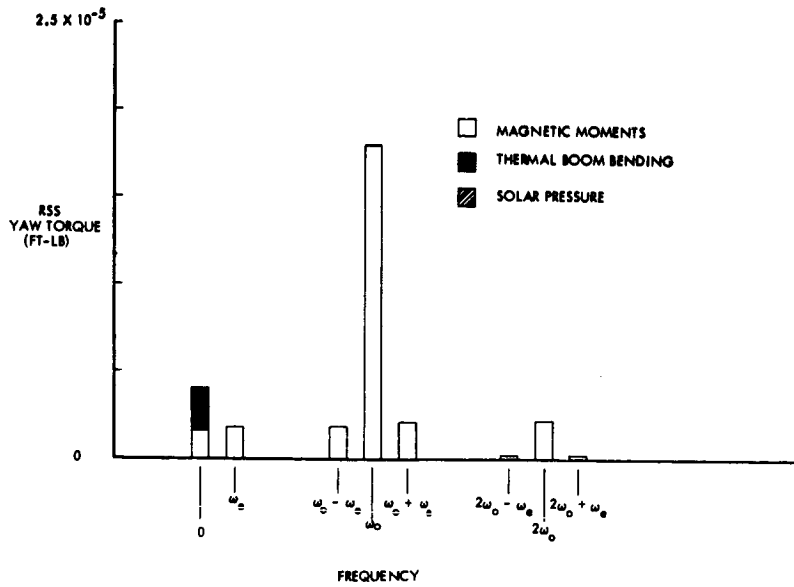


Figure IV-13 RSS Yaw Torque Versus Frequency
(Case II: Sun Normal to Orbit Plane)

pitch torque in Case I and to the d-c roll and yaw torques in Case II. Torques due to solar radiation pressure are significant only about the pitch axis, and then only when the sun is normal to the orbit plane.

As shown in Figures IV-14 and IV-15, control axis misalignments relative to the principal axes produce constant gravitational torques and eccentricity effects produce torques at orbital frequency. Note that eccentricity torques are largest about the pitch axis and, therefore, have little effect upon roll/yaw accuracy.

2. Steady-State Roll/Yaw Errors

With the information provided above, the steady-state roll and yaw errors are now evaluated for the Roll gimbal configuration. From Equation (IV-2) and (IV-4), the form of the resulting attitude errors can be expressed as

$$\frac{1}{\omega_o^2 J_{yy1}} \sum_j \sum_k \left[|\ell_{ij}(j\omega_k)| \cdot |\bar{T}_{dj}| \sin(\omega_k t + \phi_k) \right]$$

where ϕ_k is a phase angle. Thus the magnitude of the roll/yaw errors and the gimbal deflection γ_x can be estimated by the following equations:*

$$\phi = \frac{1}{\omega_o^2 J_{yy1}} \sum_k \left[|\ell_{11}(j\omega_k)| \cdot |T_{dx}(j\omega_k)| + |\ell_{12}(j\omega_k)| \cdot |T_{dy}(j\omega_k)| \right. \\ \left. + |\ell_{13}(j\omega_k)| \cdot |T_{dz}(j\omega_k)| \right] \quad (IV-6)$$

*Note that this procedure yields a pessimistic estimate in that the error magnitudes due to pitch, roll and yaw torques are treated as if they are strictly additive, as are the effects of torques at various frequencies. The resulting error estimate assumes worst case (in-phase) conditions.

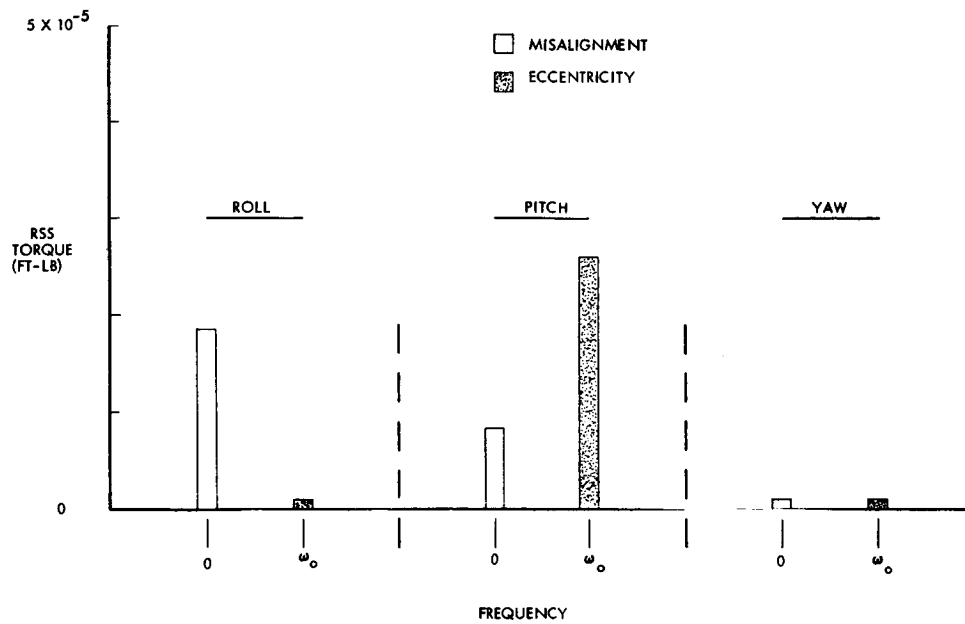


Figure IV-14 RSS Torque Due to Control Axis Misalignments and Orbital Eccentricity (Case I: Sun in Orbit Plane)

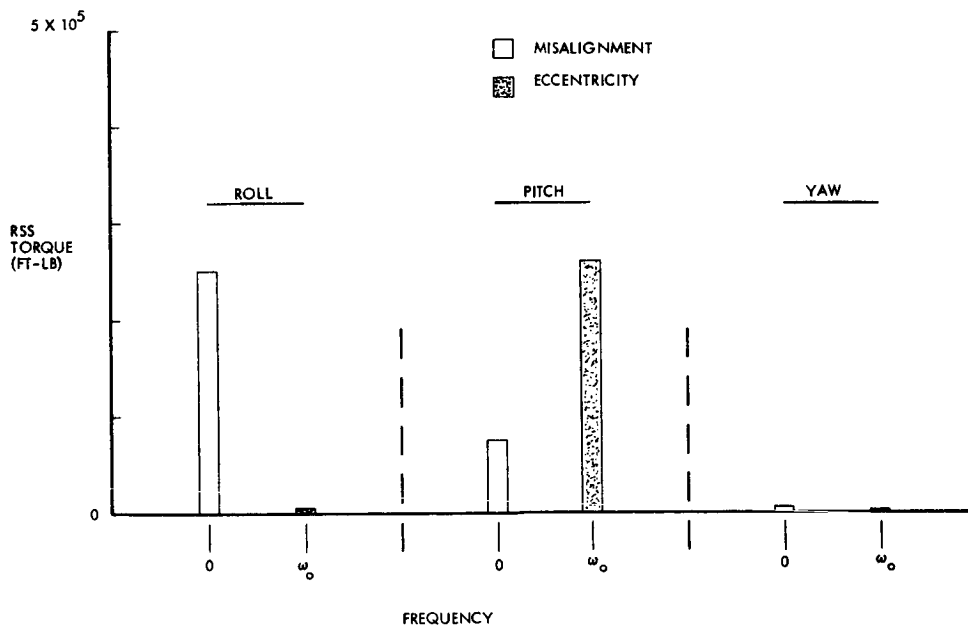


Figure IV-15 RSS Torque Due to Control Axis Misalignments and Orbital Eccentricity (Case II: Sun Normal to Orbit Plane)

$$\psi = \frac{1}{\omega_o^2 J_{yy1} k} \sum \left[|l_{31}(j\omega_k)| \cdot |T_{dx}(j\omega_k)| + |l_{32}(j\omega_k)| \cdot |T_{dy}(j\omega_k)| \right. \\ \left. + |l_{33}(j\omega_k)| \cdot |T_{dz}(j\omega_k)| \right] \quad (IV-7)$$

$$r_x = \frac{1}{\omega_o^2 J_{yy1} k} \sum \left[|l_{41}(j\omega_k)| \cdot |T_{dx}(j\omega_k)| + |l_{42}(j\omega_k)| \cdot |T_{dy}(j\omega_k)| \right. \\ \left. + |l_{43}(j\omega_k)| \cdot |T_{dz}(j\omega_k)| \right] \quad (IV-8)$$

In the above equations the external torques on the gimbals are neglected. The steady-state errors are evaluated by substituting the values of the error/torque gains and the disturbance torque into Equations (IV-6), (IV-7); and (IV-8) and performing the indicated operations.

The results are summarized in Table IV-3 in which the following control system parameters were assumed:

$$k_x = .5 \omega_o^2 J_{yy1}$$

$$c_x = \omega_o J_{yy1}$$

$$H_o = 2\omega_o J_{yy1}$$

Most of the contribution to the steady-state roll and yaw errors came from roll and yaw torques at zero, orbit rate, and twice orbit rate frequencies. As previously noted, pitch torques were well attenuated by the roll/yaw gains. More specifically, the roll/yaw errors were especially influenced by the effects of magnetic moments

and thermal boom bending. On the other hand, solar radiation pressure, control axis misalignment, and eccentricity effects did not contribute significantly to the steady-state errors.

Table IV-3 also indicates that the roll and yaw errors vary by about 1° depending on the position of the sun relative to the orbit plane. The increased error with the sun normal to the orbit plane is mainly the result of a large d-c torque due to thermal boom bending.

Disturbance Source	Steady-State Errors*(deg)					
	ϕ		ψ		γ_x	
	Case I	Case II	Case I	Case II	Case I	Case II
Magnetic Moment, Solar Radiation, Boom Bending	.76	2.0	1.45	2.41	.78	1.7
Control Axis Misalignment	.20	.26	.02	-	.16	.21
Orbital Eccentricity(1%)	.01	.01	.02	.02	--	--
Total	.97	2.27	1.49	2.42	.94	1.91

*Note: Case I - Sun in orbit plane
Case II- Sun normal to orbit plane

Table IV-3 Steady-State Roll/Yaw Errors (as defined in expressions (IV-6), (IV-7), and (IV-8)).

$$(k_x = .5 \omega_o J_{yy1}; c_x = \omega_o J_{yy1}; H_o = 2\omega_o J_{yy1}; J_{yy1} = 1500 \text{ slug-ft}^2)$$

3. Conclusions

The accuracy levels indicated in Table IV-3 should be adequate for a variety of missions; however, these results by no means represent the ultimate performance attainable with the SAGS control configuration. Two general courses can be pursued to achieve greater accuracies:

- (i) reduction of environmental disturbances
- (ii) improved roll/yaw "stiffness"

The foregoing disturbance torque estimates indicate clearly that magnetic and thermal bending effects are dominant in determining the capabilities of this control system (for the vehicle considered). Both torque sources are amenable to reduction, the former by striving for a higher degree of magnetic cleanliness and the latter by coating the inertia mast (i.e., with silver). The alternative of altering the ACS performance is probably less attractive, in that it will generally involve increases in the weight of the system. In particular, increases in either H_o or c_x will incur such penalties. Similarly, increasing the pitch inertia will have a like effect if the normalized parameters α_x and m are to remain unchanged.

Furthermore, increasing J_{yy1} may involve altering the parameters of the inertia augmentation assembly in such a way as to increase the thermal bending torques. Table IV-4 summarizes the improvements in roll/yaw control available by resorting to the techniques mentioned above. Several of these approaches will improve pitch performance as well.

System Change	Effect
Momentum bias increased from $2\omega_{yy1} J_{yy1}$ to $4\omega_{yy1} J_{yy1}$	Yaw error reduced from 2.42° to 2.05° .
Damping coefficient increased from $\omega_{yy1} J_{yy1}$ to $2\omega_{yy1} J_{yy1}$	Yaw error reduced from 2.42° to 2.15°
Boom coated with silver (.005 in. thickness)	Roll error reduced from 2.27° to 1.60° ; Yaw error not significantly affected.
Pitch inertia increased from 1500 slug-ft^2 to 3000 slug-ft^2 (by doubling the tip mass)*	Roll error reduced from 2.27° to 1.70° ; Yaw error reduced from 2.42° to 1.30° ;

*Assumes that α_x and m are unchanged (hence that the bias momentum and the damping coefficient are doubled).

Table IV-4 Effect upon Roll/Yaw Performance of Representative System Changes (Sun normal to the orbit plane)

REFERENCE

- IV-1 R. G. Nishinaga, "Preliminary Design Considerations for a Gyro-Damped Gravity-Gradient Satellite," TRW Report No. 8427-6005-RU000, dated 28 May 1965.

APPENDIX V

ROLL/YAW FREQUENCY RESPONSE PROGRAM

This appendix presents a brief description of a digital computer program developed for SAGS Roll/Yaw frequency response evaluations. Through use of this computer routine it is possible to determine the response of the SAGS control configuration to constant and periodic disturbances; such an application is presented in Appendix IV. A more detailed description of the subject digital program is to be found in Reference V-1.

As shown in the preceding appendix the small error linearized equations of motion can be written in the form

$$A(p) \bar{x}(p) = \frac{1}{\omega_o^2 J_{yy1}} \bar{T}(p) \quad (V.1)$$

where

- o $\bar{x}(p)$ is a column matrix with elements $\phi(p)$, $\theta(p)$, $\psi(p)$, $r_x(p)$, $r_z(p)$.
- o $A(p)$ is the 5 x 5 matrix of (normalized) coefficients of the linearized differential equations.
- o $\bar{T}(p)$ is a column matrix of external disturbances.
- o $p = s/\omega_o$ is the normalized frequency.
- o ω_o is the spacecraft orbital angular velocity.
- o J_{yy1} is the pitch axis moment of inertia of the spacecraft.

Solving the above equation for the vehicle attitudes and the gimbal deflections:

$$\bar{x}(p) = \frac{1}{\omega_o^2 J_{yy1}} L(p) \bar{T}(p) \quad (V.2)$$

Of particular interest is the determination of the steady-state system response to periodic (and constant) disturbances at a general real frequency ω . Letting

$$s = j\omega = jn\omega_o = pn\omega_o \quad (V.3)$$

(with n not necessarily an integer), the element $l_{ij}(jn)$ of $L(jn)$ will determine the influence of the j -th disturbance component upon the i -th position variable.

The motion of a mechanical system such as this one is described by a set of q second order differential equations (here $q = 4$ or 5 , depending upon the wheel suspension configuration). Thus the coefficient matrix is of the form

$$A(p) = Ep^2 + Fp + G \quad (V.4)$$

where E , F , and G are explicit functions of the (normalized) parameters of the system. Evaluated for real frequencies $p = jn$:

$$A(jn) = G - n^2E + jnF \quad (V.5)$$

Notice that $A(jn)$ and $L(jn)$ may be written as

$$\begin{aligned}
 A(jn) &= C + jD \\
 L(jn) &= M + jN = \{A(jn)\}^{-1}
 \end{aligned}
 \tag{V.6}$$

with C, D, M and N real square matrices which depend upon the normalized real frequency $j\omega$. M and N can be readily evaluated (for each value of n) in terms of C and D:

$$\begin{aligned}
 M &= \{C + DC^{-1}D\}^{-1} \\
 N &= -C^{-1}DM
 \end{aligned}
 \tag{V.7}$$

The digital computer program computes the magnitude of the elements of $L(jn)$ as a function of n, starting with the system (and vehicle) parameters as input data. The sequence of computer operations is as shown in Figures IV-1. The first step is the computation of E, F and G in terms of the following normalized parameters of the system:

Wheel Bias momentum:	$m =$	$\frac{H_o}{\omega_o J_{yy1}}$
Pitch Wheel gain:	$g_o =$	$\frac{G_o}{\omega_o J_{yy1}}$
Spring constant:	$\beta_i =$	$\frac{k_i}{\omega_o^2 J_{yy1}} \quad (i = x, z)$
Damping coefficient:	$\alpha_i =$	$\frac{c_i}{\omega_o J_{yy1}} \quad (i = x, z)$
General parameter: *	$Q'_i =$	$\frac{Q_i}{J_{yy1}}$

*The Q_i are mass and inertia parameters, all of which are normalized relative to the spacecraft pitch inertia.

Denoting, for example, the general element of E by e_{ij} , the elements of E, F and G are computed as follows:

$$e_{11} = I'_{xx1} + I'_{xx3} + I'_{xxc} + m'_g(\xi_{y1}^2 + \xi_{z1}^2) + I'_{xx2} + m'_o(t_{y1}^2 + t_{z1}^2)$$

$$e_{12} = -I'_{xy1} - I'_{xy3} - I'_{xyc} - m'_g \xi_{x1} \xi_{y1} - I'_{xy2} - m'_o t_{x1} t_{y1}$$

$$e_{13} = -I'_{xz1} - I'_{xz3} - I'_{xzc} - m'_g \xi_{x1} \xi_{z1} - I'_{xz2} - m'_o t_{x1} t_{z1}$$

$$e_{14} = I'_{xx3} + \Delta_1 I'_{xxc}$$

$$e_{15} = -I'_{xz3} - \Delta_2 I'_{xzc}$$

$$e_{21} = e_{12}$$

$$e_{22} = 1 + I'_{yy3} + I'_{yyc} + m'_g(\xi_{z1}^2 + \xi_{x1}^2) + I'_{yy2} + m'_o(t_{x1}^2 + t_{z1}^2)$$

$$e_{23} = -I'_{yz1} - I'_{yz3} - I'_{yyc} - m'_g \xi_{y1} \xi_{z1} - I'_{yz2} - m'_o t_{y1} t_{z1}$$

$$e_{24} = -I'_{xy3} - \Delta_1 I'_{xyc}$$

$$e_{25} = -I'_{yz3} - \Delta_2 I'_{yyc}$$

$$e_{31} = e_{13}$$

$$e_{32} = e_{23}$$

$$e_{33} = I'_{zz1} + I'_{zz3} + I'_{zzc} + m'_g(\xi_{x1}^2 + \xi_{y1}^2) + I'_{zz2} + m'_o(t_{x1}^2 + t_{y1}^2)$$

$$e_{34} = -I'_{zx3} - \Delta_1 I'_{zxc}$$

$$e_{35} = I'_{zz3} + \Delta_2 I'_{zzc}$$

$$e_{41} = e_{14}$$

$$e_{42} = e_{24}$$

$$e_{43} = e_{34}$$

$$e_{44} = e_{14}$$

$$e_{45} = -I'_{xz3}$$

$$e_{51} = e_{15}$$

$$e_{52} = e_{25}$$

$$e_{53} = e_{35}$$

$$e_{54} = e_{45}$$

$$e_{55} = e_{35}$$

$$f_{11} = 0$$

$$f_{12} = 2(I'_{zy1} + I'_{zy3} + I'_{zyc} + m'g_{z1}\xi_{y1} + I'_{zy2} + m'o_{y1}l_{z1})$$

$$f_{13} = 1 + I'_{yy3} + I'_{yyc} - I'_{xx1} - I'_{xx3} - I'_{xxc} - I'_{zz1} - I'_{zz3} - I'_{zzc} + m \\ - 2m'g_{y1}^2 + I'_{yy2} - I'_{xx2} - I'_{zz2} - 2m'o_{y1}^2$$

$$f_{14} = 0$$

$$f_{15} = I'_{yy3} - I'_{zz3} - I'_{xx3} + m + \Delta_2(I'_{yyc} - I'_{xxc} - I'_{zzc})$$

$$f_{21} = -f_{12}$$

$$f_{22} = -g_o$$

$$f_{23} = 2(I'_{xy1} + I'_{xy3} + I'_{xyc} + m'g_{x1}\xi_{y1} + I'_{xy2} + m'o_{x1}l_{y1})$$

$$f_{24} = -2(I'_{yz3} + \Delta_1 I'_{yzc})$$

$$f_{25} = 2(I'_{xy3} + \Delta_2 I'_{xyc})$$

$$f_{31} = -f_{13}$$

$$f_{32} = -f_{23}$$

$$f_{33} = 0$$

$$f_{34} = I'_{zz3} + I'_{xx3} - I'_{yy3} - m + \Delta_1 (I'_{zzc} + I'_{xxc} - I'_{yyc})$$

$$f_{35} = 0$$

$$f_{41} = 0$$

$$f_{42} = -f_{24}$$

$$f_{43} = -f_{34}$$

$$f_{44} = \alpha_x$$

$$f_{45} = I'_{yy3} - I'_{zz3} - I'_{xx3} + m$$

$$f_{51} = -f_{15}$$

$$f_{52} = -f_{25}$$

$$f_{53} = 0$$

$$f_{54} = -f_{45}$$

$$g_{11} = 4[1 + I'_{yy3} + I'_{yyc} - I'_{zz1} - I'_{zz2} - I'_{zz3} - I'_{zzc} + I'_{yy2} \\ + m'(\xi_{z1}^2 - \xi_{y1}^2) + m'_0(\ell_{z1}^2 - \ell_{y1}^2)] + m$$

$$g_{12} = 3(I'_{xy1} + I'_{xy3} + I'_{xyc} + m'_g \xi_{x1} \xi_{y1} + I'_{xy2} + m'_o l_{x1} l_{y1})$$

$$g_{13} = -I'_{zx1} - I'_{zx3} - I'_{zxc} - m'_g \xi_{x1} \xi_{z1} - I'_{zx2} - m'_o l_{x1} l_{z1}$$

$$g_{14} = 4[I'_{yy3} - I'_{zz3} + \Delta_1 (I'_{yyc} - I'_{zyc})] + m$$

$$g_{15} = -4(I'_{xz3} + \Delta_2 I'_{xzc})$$

$$g_{21} = \frac{4}{3} g_{12}$$

$$g_{22} = 3[I'_{xx1} + I'_{xx3} + I'_{xxc} + I'_{xx2} - I'_{zz1} - I'_{zz3} - I'_{zyc} - I'_{zyc} \\ + m'_g (\xi_{z1}^2 - \xi_{x1}^2) + m'_o (l_{z1}^2 - l_{x1}^2)]$$

$$g_{23} = I'_{zy1} + I'_{zy3} + I'_{zyc} + m'_g \xi_{y1} \xi_{z1} + I'_{zy2} + m'_o l_{z1} l_{y1}$$

$$g_{24} = 3(I'_{xy3} + \Delta_1 I'_{xyc})$$

$$g_{25} = -3(I'_{yz3} + \Delta_2 I'_{yyc})$$

$$g_{31} = 4g_{13}$$

$$g_{32} = -3g_{23}$$

$$g_{33} = 1 + I'_{yy3} + I'_{yyc} - I'_{xx1} - I'_{xx3} - I'_{xxc} - I'_{xx2} + I'_{yy2} + m \\ + m'_g (\xi_{x1}^2 - \xi_{y1}^2) + m'_o (l_{x1}^2 - l_{y1}^2)$$

$$\epsilon_{34} = - I'_{zx3} - \Delta_1 I'_{zxc}$$

$$\epsilon_{35} = I'_{yy3} - I'_{xx3} + \Delta_2 (I'_{yyc} - I'_{xxc}) + m$$

$$\epsilon_{41} = \epsilon_{14}$$

$$\epsilon_{42} = \epsilon_{24}$$

$$\epsilon_{43} = \epsilon_{34}$$

$$\epsilon_{44} = 4[I'_{yy3} - I'_{zz3} + \Delta_1 (I'_{yyc} - I'_{zxc})] + m + \beta_x$$

$$\epsilon_{45} = - I'_{xz3} - 3\Delta_1 I'_{xz3}$$

$$\epsilon_{51} = \epsilon_{15}$$

$$\epsilon_{52} = \epsilon_{25}$$

$$\epsilon_{53} = \epsilon_{35}$$

$$\epsilon_{54} = \epsilon_{45}$$

$$\epsilon_{55} = I'_{yy3} - I'_{xx3} + m + \beta_z + \Delta_2 (I'_{yyc} - I'_{xxc})$$

The various parameters in the above expressions are defined in Appendix VII of the SAGS First Quarterly Report (Reference 1), and the above elements are therein developed in detail.

Following the determination of E, F and G, the matrices C, D, M, and N are computed for each particular frequency, and $|t_{ij}(jn)|$ is computed and stored for all i, j and each n. Provisions are included for Calcomp plotting of the influence coefficients as functions of the normalized frequency (e.g., see Appendix IV).

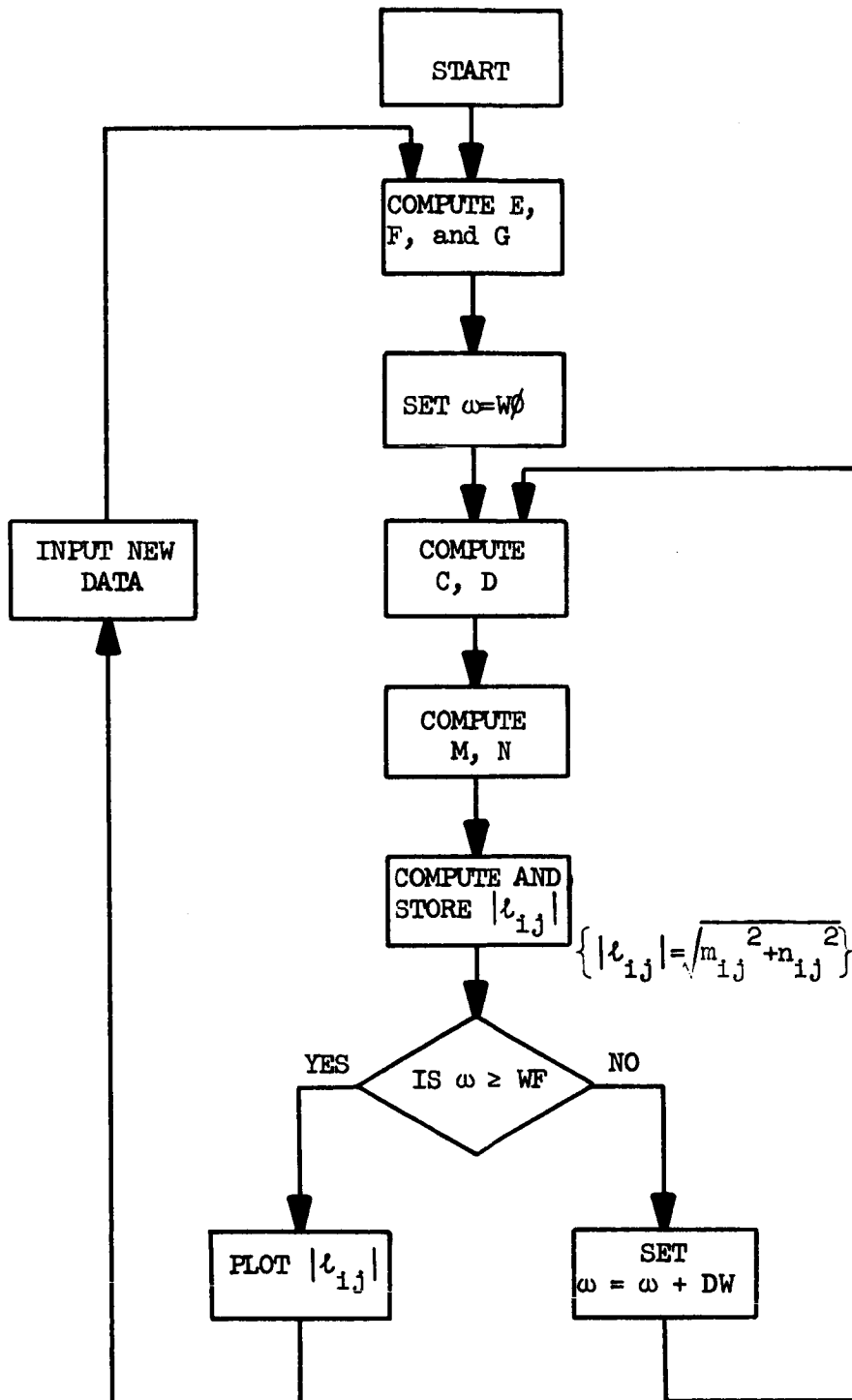


Figure V-1

Computer Flow Diagram

REFERENCE

- V-1. B. Krentzin, "Inversion of a Frequency Dependent Matrix,"
TRW Internal Memorandum 65.9352.1-94, 29 December 1965.

APPENDIX VI
SAGS DISTURBANCE TORQUE ANALYSIS

This appendix presents an evaluation of the major disturbances on the SAGS satellite. The specific objective of the study was to obtain a measure of the disturbance torques during normal mode operation. The sources of disturbance torque considered includes:

- (i) Solar radiation pressure
- (ii) Thermal boom bending
- (iii) Residual magnetic moments
- (iv) Control axis misalignment
- (v) Orbital eccentricity

The symbols and constants used in this appendix are defined at its end.

A. SATELLITE MODEL AND ASSUMPTIONS

The study is based on a 500 lb SAGS satellite which is nominally in a 750 nautical mile orbit. The dimensions and the mass distribution of the satellite are shown in Figures VI-1 and VI-2, respectively. It is noted that the satellite has a control box (C), a sensory ring (R), a rotatable solar array (P) with a hinge (H), and an inertia mast (M). The mast is 52 ft in length with a 15 lb tip mass to provide a pitch inertia of about 1500 slug-ft^2 .

Table VI-1 lists values of the system parameters assumed in the disturbance torque evaluation. These parameters were selected on the basis of providing a representative measure of the disturbance torques. For instance, the torques due to thermal boom bending are

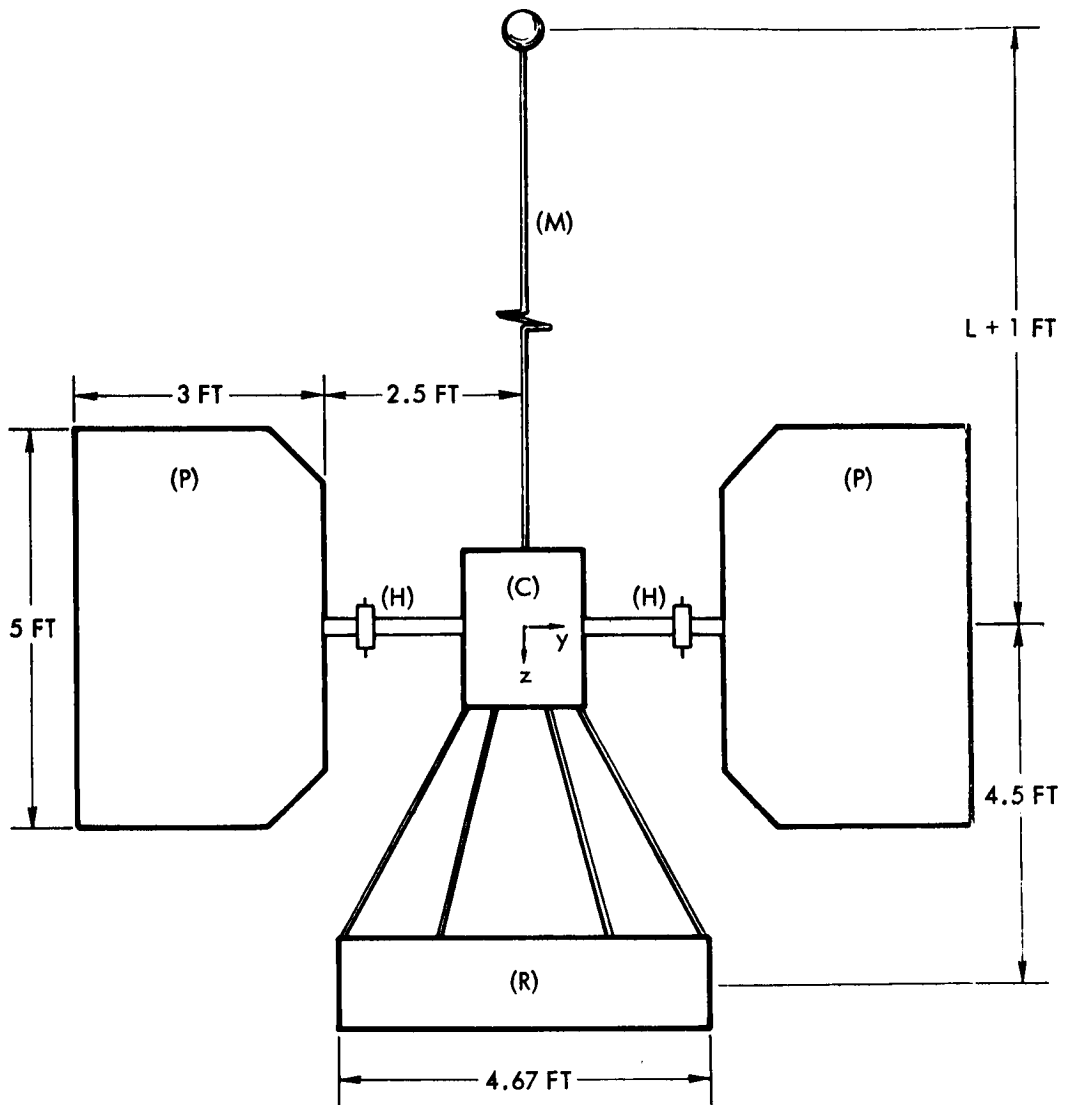


Figure VI-1 Spacecraft Dimensions

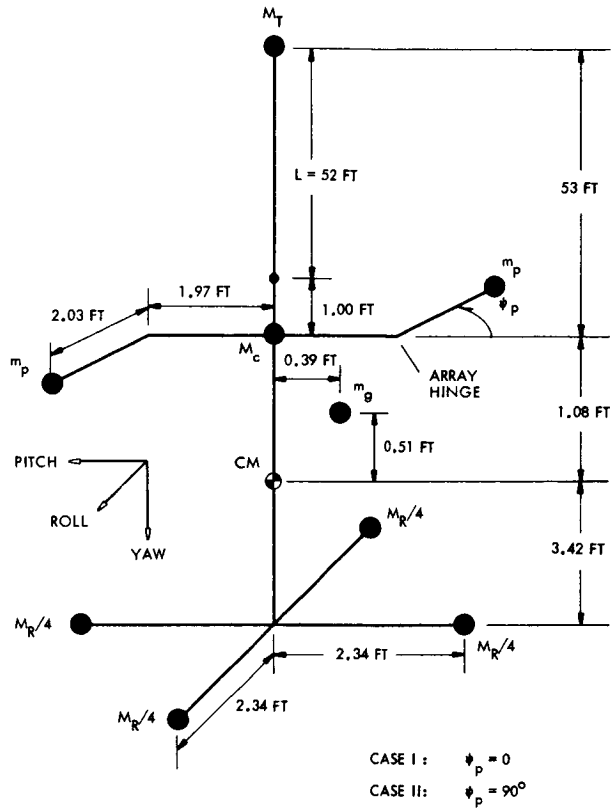


Figure VI-2 Spacecraft Mass Distribution

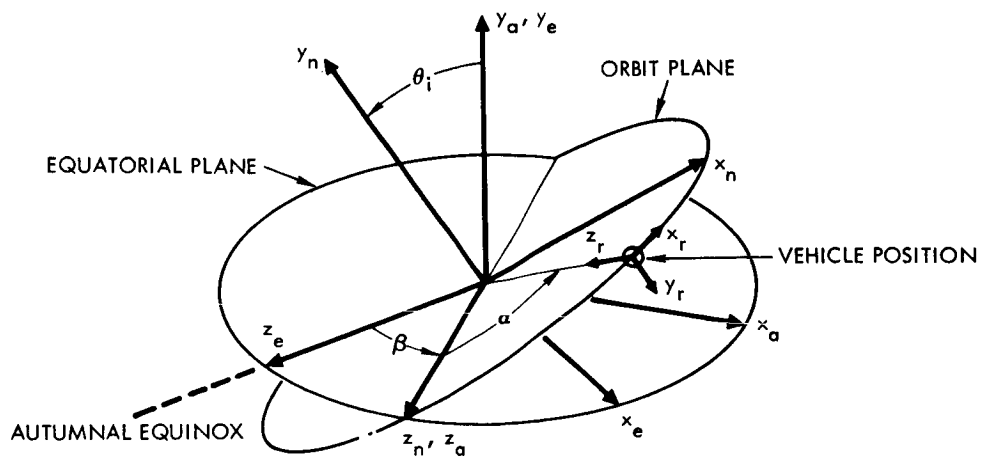


Figure VI-3 Coordinate Frames

Table VI-1

SAGS SYSTEM CONSTANTS

$r_c = .78 \text{ ft}$	$l_c = 2.0 \text{ ft}$
$r_r = 2.34 \text{ ft}$	$l_r = 1.11 \text{ ft}$
$r_t = 1 \text{ in.}$	$l_t = 6.9 \text{ in.}$
$M_c = 2.0 \text{ slugs}$	$v_c = .2$
$M_r = 9.33 \text{ slugs}$	$v_r = .2$
$M_t = .47 \text{ slugs}$	$v_t = 0$
$M_p = .93 \text{ slugs}$	$v_p = .3$
$m_g = 1.89 \text{ slugs}$	$v_b = .63$
$l_b = 52 \text{ ft}$	$A_p = 14.6 \text{ ft}^2$
$d_b = .5 \text{ in.}$	$K = 1.21 \times 10^{-3} \text{ ft}^{-1}$
$t_b = .002 \text{ in.}$	$K^* = .6 \times 10^{-3} \text{ ft}^{-1}$
$\phi_g = 2^\circ$	$\epsilon = .01$
$\theta_g = 2^\circ$	$\omega_o = .924 \times 10^{-3} \text{ rad/sec}$
$\psi_g = 5^\circ$	$\omega_e = .727 \times 10^{-4} \text{ rad/sec}$

Table VI-1 (Cont'd)

SAGS SYSTEM CONSTANTS

Parameter	Case I Sun in Orbit Plane	Case II Sun Normal to Orbit Plane
Deployed Boom:		
J_{xx1}	1535 slug-ft ²	1520 slug-ft ²
J_{yy1}	1505 slug-ft ²	1520 slug-ft ²
J_{zz1}	81 slug-ft ²	66 slug-ft ²
Undeployed Boom:		
J_{xx1}	173 slug-ft ²	150 slug-ft ²
J_{yy1}	143 slug-ft ²	149 slug-ft ²
J_{zz1}	81 slug-ft ²	66 slug-ft ²
M_{xo}	5×10^{-5} ft-lb/gauss	5×10^{-5} ft-lb/gauss
M_{yo}	5×10^{-5} ft-lb/gauss	-5×10^{-5} ft-lb/gauss
M_{zo}	-5×10^{-5} ft-lb/gauss	5×10^{-5} ft-lb/gauss
M_{xt}	-2.5×10^{-5} ft-lb/gauss	-2.5×10^{-5} ft-lb/gauss
M_{yt}	2.5×10^{-5} ft-lb/gauss	2.5×10^{-5} ft-lb/gauss
M_{zt}	2.5×10^{-5} ft-lb/gauss	2.5×10^{-5} ft-lb/gauss
ϕ_x	0°	45°
ϕ_y	-45°	45°
ϕ_z	90°	45°
M_{xp}	10×10^{-5} ft-lb/gauss	5×10^{-5} ft-lb/gauss

based on an uncoated DeHavilland boom with a diameter of .5 inch and a thickness of .002. Gravity torques resulting from misalignment of the control axes from the principal axes are based on a maximum 2 degree offset about the roll and pitch axes and a 5 degree offset about the yaw axis prior to boom extension. A nominal residual magnetic moment of 5×10^{-5} ft-lb/gauss is assumed on the satellite. Torques induced from an elliptic orbit are based on an orbital eccentricity of 1 percent.

To simplify the analysis, the following major assumptions are made:

- (1) Torques due to solar radiation pressure, thermal boom bending, and magnetic moments on the solar panels are nulled during eclipse.
- (2) The effects of shadowing are neglected.
- (3) The magnetic field of the earth is approximated by a dipole model.
- (4) Nodal regression is neglected; the location of the sun relative to the orbit plane is constant.
- (5) Torques which contain attitude dependent terms are neglected.

B. COORDINATE SYSTEMS

In this analysis, the principal inertia axis coordinate frame (x, y, z) lies at the satellite's center of mass and is assumed to be aligned with the orbiting reference frame (x_r, y_r, z_r) , or

$$\begin{bmatrix} \bar{x} \\ \bar{y} \\ \bar{z} \end{bmatrix} = \begin{bmatrix} \bar{x}_r \\ \bar{y}_r \\ \bar{z}_r \end{bmatrix} \quad (\text{VI.1})$$

The control axes (x_c, y_c, z_c) are related to the principal axes by offset rotations ϕ_g, θ_g, ψ_g about the roll, pitch, and yaw axes, respectively. Thus we can write

$$\begin{bmatrix} \bar{x}_c \\ \bar{y}_c \\ \bar{z}_c \end{bmatrix} = \begin{bmatrix} 1 & \psi_g & -\theta_g \\ -\psi_g & 1 & \phi_g \\ \theta_g & -\phi_g & 1 \end{bmatrix} \begin{bmatrix} \bar{x} \\ \bar{y} \\ \bar{z} \end{bmatrix} \quad (\text{VI.2})$$

where small offset angles are assumed.

The solar array coordinate set (x_h, y_h, z_h) is defined relative to the principal set by a paddle rotation θ_p and hinge rotation ψ_p as

$$\begin{bmatrix} \bar{x}_h \\ \bar{y}_h \\ \bar{z}_h \end{bmatrix} = \begin{bmatrix} C\psi_p & S\psi_p & 0 \\ -S\psi_p & C\psi_p & 0 \\ 0 & 0 & 1 \end{bmatrix} \begin{bmatrix} C\theta_p & 0 & -S\theta_p \\ 0 & 1 & 0 \\ S\theta_p & 0 & C\theta_p \end{bmatrix} \begin{bmatrix} \bar{x} \\ \bar{y} \\ \bar{z} \end{bmatrix} \quad (\text{VI.3})$$

where S and C denote sine and cosine, respectively.

Figure VI-3 shows the orthogonal coordinates necessary to describe the orbit position of the satellite relative to inertial space. Note that the regression angle β is measured from the Autumnal Equinox to the ascending node. The angle θ_i is the

inclination of the orbit plane with respect to the equatorial plane. The orbit angle α defines the coordinate frame (x_n, y_n, z_n) relative to the orbital reference frame as

$$\begin{bmatrix} \bar{x}_n \\ \bar{y}_n \\ \bar{z}_n \end{bmatrix} = \begin{bmatrix} \cos\alpha & 0 & -\sin\alpha \\ 0 & -1 & 0 \\ -\sin\alpha & 0 & -\cos\alpha \end{bmatrix} \begin{bmatrix} \bar{x}_r \\ \bar{y}_r \\ \bar{z}_r \end{bmatrix} \quad (\text{VI.4})$$

C. ORBITAL RELATIONS

The satellite is nominally in a 750 nautical mile polar orbit. To vary thermal conditions, the following locations of the sun are considered:

Case I: Sun in orbit plane

Case II: Sun normal to orbit plane

To simplify the analysis, the sun vector $\bar{\mu}_s$, which is directed from earth to the sun, is assumed to be along the Autumnal Equinox in both of these cases. Thus the orbital parameters become

$$\begin{array}{ll} \text{Case I:} & \bar{\mu}_s = \bar{z}_n \\ & \theta_1 = 90^\circ \\ & \beta = 0^\circ \\ \text{Case II:} & \bar{\mu}_s = \bar{y}_n \\ & \theta_1 = 90^\circ \\ & \beta = 90^\circ \end{array}$$

The face of the solar array is assumed to be maintained normal to the sun vector, or

$$\bar{\mu}_s = \bar{x}_h$$

By imposing the above requirement, the control law for the solar array becomes

$$\begin{aligned} \text{Case I:} \quad \theta_p &= \alpha + 90^\circ \\ \psi_p &= 0^\circ \\ \text{Case II:} \quad \theta_p &= 0^\circ \\ \psi_p &= -90^\circ \end{aligned} \tag{VI.5}$$

It is evident that the solar array rotates at orbit rate frequency when the sun is in the orbit plane. When the sun is normal to the orbit plane, the solar array is fixed relative to the main body of the satellite. Note that paddle angle in Case II is arbitrary.

D. DISTURBANCE TORQUE EVALUATION

1. General Considerations

In this study the disturbance torques \bar{T}_d are evaluated as a sum of trigonometric functions and can be expressed as

$$\bar{T}_d = \begin{bmatrix} \sum_k A_{kx} \cos \omega_k t + \sum_k B_{kx} \sin \omega_k t \\ \sum_k A_{ky} \cos \omega_k t + \sum_k B_{ky} \sin \omega_k t \\ \sum_k A_{kz} \cos \omega_k t + \sum_k B_{kz} \sin \omega_k t \end{bmatrix} \tag{VI.6}$$

where ω_k = k-th frequency,

t = time

and A_{ki} , B_{ki} ($i = x, y, z$) represent components of the disturbance torques. Because of the listed assumptions, there are but two time varying parameters in the system: the orbit angle α and an earth angle μ . For the purposes of this study, the orbit angle and earth angle are related to the orbit rate of the satellite (ω_o) and the spin rate of the earth (ω_e) as

$$\alpha = \omega_o t$$

$$\mu = \omega_e t$$

The significant frequencies ω_k for the disturbances considered are

Solar pressure: $\omega_k = 0, \omega_o, 2\omega_o, 3\omega_o$

Thermal bending: $\omega_k = 0, \omega_o, 2\omega_o, 3\omega_o$

Magnetics: $\omega_k = 0, \omega_o, \omega_o \pm \omega_e, 2\omega_o, 2\omega_o \pm \omega_e,$
 $2\omega_o + 2\omega_e, 3\omega_o, 3\omega_o \pm \omega_e$

Misalignment: $\omega_k = 0$

Eccentricity: $\omega_k = \omega_o$

Terms above $3\omega_o$ are neglected since the system frequency response to disturbance torques is well attenuated at these frequencies (See Appendix IV).

2. Method of Approach

Because of the complex nature of the satellite, some of the disturbance torques were evaluated on a TRW Generalized Disturbance

Program (AC019). The basic disturbance equations in this program were derived in Reference VI-1. In particular, the AC019 program was used to calculate torques due to solar radiation pressure and thermal boom bending. Torques due to solar pressure on a rotating solar array, magnetic torques, and torques due to control axes misalignment and eccentricity effects are analytically derived in the following sections.

Before proceeding to the analysis, let us digress to consider the effects of eclipse. According to assumption (1), the torques which are affected by the sun are nulled when the satellite is in eclipse. Thus the resulting expression of the disturbance torques will be modified.

Since most of the disturbances occur at d-c and at orbital harmonics, the i-th component of the torques in Equation (VI.6) can be expressed as

$$T_{di} = A_{oi} + \sum_{n=1}^3 A_{ni} \cos n\alpha + \sum_{n=1}^3 B_{ni} \sin n\alpha \quad (\text{VI.7})$$

where $i = x, y, z$. (In this equation ω_e is approximated by zero.) The effect of eclipse on the disturbance torque is to modify Equation (VI.7) by a factor $W(\alpha)$ to yield

$$T_{di}^* = W(\alpha) T_{di} \quad (\text{VI.8})$$

where

$$W(\alpha) = \begin{cases} 1, & 0 \leq \alpha < \pi - \theta_e \\ 0, & \pi - \theta_e \leq \alpha \leq \pi + \theta_e \\ 1, & \pi + \theta_e < \alpha \leq 2\pi \end{cases}$$

and θ_e is the eclipse half-cone angle. By expanding Equation (VI.8) in a Fourier series about the orbital harmonics, the modified torque component T_{di}^* can be expressed as

$$T_{di}^* = D_{0i} + \sum_{n=1}^3 D_{ni} \cos n\alpha + \sum_{n=1}^3 E_{ni} \sin n\alpha \quad (\text{VI.9})$$

where

$$D_{0i} = \left(1 - \frac{\theta_e}{\pi}\right) A_{0i} + \left(\frac{\sin\theta_e}{\pi}\right) A_{1i} - \left(\frac{\sin 2\theta_e}{2\pi}\right) A_{2i} + \left(\frac{\sin 3\theta_e}{3\pi}\right) A_{3i}$$

$$D_{1i} = \left(\frac{2\sin\theta_e}{\pi}\right) A_{0i} + \left(1 - \frac{\theta_e}{\pi} - \frac{\sin 2\theta_e}{2\pi}\right) A_{1i}$$

$$+ \frac{1}{\pi} \left(\sin\theta_e + \frac{\sin 3\theta_e}{3}\right) A_{2i} - \frac{1}{\pi} \left(\frac{1}{2} \sin\theta_e + \frac{1}{4} \sin 4\theta_e\right) A_{3i}$$

$$D_{2i} = - \left(\frac{\sin 2\theta_e}{\pi}\right) A_{0i} + \frac{1}{\pi} \left(\sin\theta_e + \frac{1}{3} \sin 3\theta_e\right) A_{1i}$$

$$+ \left(1 - \frac{\theta_e}{\pi} - \frac{\sin 4\theta_e}{4\pi}\right) A_{2i} + \frac{1}{\pi} \left(\sin\theta_e + \frac{1}{5} \sin 5\theta_e\right) A_{3i}$$

$$D_{3i} = \left(\frac{2\sin 3\theta_e}{3\pi}\right) A_{0i} - \frac{1}{\pi} \left(\frac{1}{2} \sin 2\theta_e + \frac{1}{4} \sin 4\theta_e\right) A_{1i}$$

$$+ \frac{1}{\pi} \left(\sin\theta_e + \frac{1}{5} \sin 5\theta_e\right) A_{2i} + \left(1 - \frac{\theta_e}{\pi} - \frac{\sin 6\theta_e}{6\pi}\right) A_{3i}$$

$$E_{1i} = \left(1 - \frac{\theta_e}{\pi} + \frac{\sin 2\theta_e}{2\pi}\right) B_{1i} + \frac{1}{\pi} \left(\sin\theta_e - \frac{1}{3} \sin 3\theta_e\right) B_{2i} \\ - \frac{1}{\pi} \left(\frac{1}{2} \sin 2\theta_e - \frac{1}{4} \sin 4\theta_e\right) B_{3i}$$

$$E_{2i} = \frac{1}{\pi} \left(\sin\theta_e - \frac{1}{3} \sin 3\theta_e\right) B_{1i} + \left(1 - \frac{\theta_e}{\pi} + \frac{\sin 4\theta_e}{4\pi}\right) B_{2i} \\ + \frac{1}{\pi} \left(\sin\theta_e - \frac{1}{5} \sin 5\theta_e\right) B_{3i}$$

$$E_{3i} = -\frac{1}{\pi} \left(\frac{1}{2} \sin 2\theta_e - \frac{1}{4} \sin 4\theta_e\right) B_{1i} + \frac{1}{\pi} \left(\sin\theta_e - \frac{1}{5} \sin 5\theta_e\right) B_{2i} \\ + \left(1 - \frac{\theta_e}{\pi} + \frac{\sin 6\theta_e}{6\pi}\right) B_{3i}$$

Equations (VI.9) are used in the subsequent derivations of the disturbance torque to account for the presence of eclipse.

3. Solar Radiation Pressure Torques

Torques due to solar radiation pressures were obtained from the ACO19 program based on the following body shapes on the satellite:

Control box	-	cylinder
Sensory ring	-	cylinder
Solar panel	-	flat plate
Boom	-	long cylinder
Tip mass	-	cylinder

The resulting components of the solar radiation torque are listed in Table VI-2. It is evident that when the sun is in the orbit plane, the solar pressure on the satellite produces a torque about the pitch control axis. When the sun is normal to the orbit plane, the satellite suffers a constant torque about the roll axis.

Frequency ω_k	Solar Radiation Pressure Torques($\times 10^{-6}$ ft-lb)					
	Roll		Pitch		Yaw	
	A_{kx}	B_{kx}	A_{ky}	B_{ky}	A_{kz}	B_{kz}
Case I:						
0	0	-	.11	-	0	-
ω_0	0	0	.12	-6.3	0	0
$2\omega_0$	0	0	-.10	-.38	0	0
$3\omega_0$	0	0	-.22	2.3	0	0
Case II:						
0	8.5	-	0	-	0	-
ω_0	0	0	0	0	0	0
$2\omega_0$	0	0	0	0	0	0
$3\omega_0$	0	0	0	0	0	0

Table VI-2. Summary of Solar Pressure Torques

In Case I, the ACO19 program does not account for the rotating solar array. Thus the torques resulting from solar radiation pressure on the rotating array are now derived. Based upon the momentum interchange model presented in Reference VI-2, the solar force \bar{F}_s on each solar panel is:

$$\bar{F}_s = -V_s A_p (1 + v_p) \bar{x}_h \quad (\text{VI.10})$$

where V_s = Solar radiation pressure constant (9.4×10^{-8} lb/ft²)

A_p = Area of each solar panel

ν_p = Reflectivity coefficient.

Transforming \bar{F}_s to the principal coordinate set, we obtain

$$\bar{F}_s = -V_s A_p (1 + \nu_p) [C\theta_p \bar{x} - S\theta_p \bar{z}] \quad (\text{VI.11})$$

Let \bar{r}_i be a vector from the satellite's cm to the center of pressure of panel i ($i = 1, 2$), or

$$\bar{r}_1 = L_{y1} \bar{y} - L_{z1} \bar{z} \quad (\text{VI.12})$$

$$\bar{r}_2 = -L_{y2} \bar{y} - L_{z2} \bar{z}$$

where the distances L_{yi} and L_{zi} are found in Figure VI-2 ($L_{y1} = L_{y2}$, $L_{z1} = L_{z2}$). Thus the solar pressure torque \bar{T}_s is simply expressed as

$$\bar{T}_s = \left(\sum_{i=1}^2 \bar{r}_i \right) \times \bar{F}_s \quad (\text{VI.13})$$

Substituting the relation of Equations (VI.11) and (VI.12) into (VI.13) yields

$$\bar{T}_s = 2V_s A_p (1 + \nu_p) L_{z1} \begin{bmatrix} 0 \\ C\theta_p \\ 0 \end{bmatrix} \quad (\text{VI.14})$$

By accounting for the paddle control law and the eclipse effects, the torque components Equation (VI.14) can be expressed as follows:

$$T_{sx} = T_{sz} = 0$$

$$T_{sy} = -2V_s A_p (1 + \nu_p) L_{z1} \left[\left(1 - \frac{\theta_e}{\pi} + \frac{S2\theta_e}{2\pi}\right) S\alpha + \frac{1}{\pi} \left(S\theta_e - \frac{S3\theta_e}{3}\right) S2\alpha - \frac{1}{2\pi} \left(S2\theta_e - \frac{1}{2} S4\theta_e\right) S3\alpha \right] \quad (VI.15)$$

The above torques were combined with the results of the AC019 program in Table VI-2.

4. Thermal Boom Bending Torques

To evaluate torques due to thermal boom bending, both in-plane and out-of-plane bending were considered. According to Reference VI-3, the deflection of a DeHavilland boom is proportional to an in-plane bending coefficient K which can be expressed as

$$K = \frac{\alpha_s J_s e d_b}{8 k t_b}$$

where J_s = Solar constant (442 BTU/hr-ft²)

e = Thermal expansion coefficient

α_s = Absorptivity

k = Thermal conductivity

d_b = Nominal boom diameter

t_b = Boom thickness

In this study, the out-of-plane bending coefficient K^* is assumed as

$$K^* = .5 K$$

For a DeHavilland boom made of beryllium copper material, the above parameters are

$$e = 1.04 \times 10^{-5}/^{\circ}\text{F}$$

$$\alpha_s = .37$$

$$k = 44 \text{ BTU/hr-ft } ^{\circ}\text{F}$$

By assuming a boom diameter of .5 inch and a boom thickness of .002 inch, the bending coefficients become

$$K = 1.21 \times 10^{-3} \text{ ft}^{-1}$$

$$K^* = .6 \times 10^{-3} \text{ ft}^{-1}$$

The resulting torques due to boom bending were obtained from the ACO19 program and are presented in Table VI-3. Note that thermal boom bending produces significant orbital frequency torques about the pitch axis when the sun is in the orbit plane. When the sun is normal to the orbit plane, a large constant roll torque results from the boom bending effects.

5. Magnetic Torques

In general, the torque \bar{T}_m due to the magnetic moments on the satellite can be expressed as

$$\bar{T}_m = \bar{M} \times \bar{B} \quad (\text{VI.16})$$

where

\bar{M} = Magnetic moment vector,

\bar{B} = Magnetic field vector of the earth.

Frequency ω_k	Thermal Boom Bending Torque ($\times 10^{-6}$ ft-lb)					
	Roll		Pitch		Yaw	
	A_{kx}	B_{kx}	A_{ky}	B_{ky}	A_{kz}	B_{kz}
Case I:						
0	-0.53	-	-0.33	-	0	-
ω_o	-1.3	.05	-0.80	-67.5	0	0
$2\omega_o$	-0.35	0	-0.58	-21.8	0	0
$3\omega_o$	1.1	-0.06	0	15.3	0	0
Case II:						
0	-78.7	-	0	-	-2.6	-
ω_o	0	0	0	0	0	0
$2\omega_o$	0	0	0	0	0	0
$3\omega_o$	0	0	0	0	0	0

Table VI-3. Summary of Thermal Boom Bending Torques

In Reference VI-4, expressions of \bar{B} were derived based on a simple dipole model of the earth's magnetic field. These results when transformed into the (x_r, y_r, z_r) frame are:

$$B_{xr} = -\frac{M_e}{r_o^3} \left\{ -\cos\epsilon_o \sin\theta_1 \cos\alpha + \frac{1}{2} [(1+\cos\theta_1) \cos(\alpha-\mu) - (1-\cos\theta_1) \cos(\alpha+\mu)] \sin\epsilon_o \right\}$$

$$B_{yr} = \frac{M_e}{r_o^3} \left\{ -\cos\epsilon_o \cos\theta_1 - \sin\epsilon_o \sin\theta_1 \cos\mu \right\} \quad (VI.17)$$

$$B_{zr} = \frac{M_e}{r_o^3} \left\{ 2\cos\epsilon_o \sin\theta_1 \sin\alpha - [(1+\cos\theta_1) \sin(\alpha-\mu) - (1-\cos\theta_1) \sin(\alpha+\mu)] \sin\epsilon_o \right\}$$

where

$$\begin{aligned}
 M_e &= \text{Magnetic dipole moment of earth } (2.845 \times 10^{21} \text{ gauss-ft}^3) \\
 r_o &= \text{Radius of orbit (4190 n. mile)} \\
 \epsilon_o &= \text{Angle between geographic and geomagnetic north pole} \\
 &\quad (\approx 11^\circ) \\
 \mu &= \alpha_e + 20^\circ - \beta, (\dot{\mu} = \omega_e)
 \end{aligned}$$

The total magnetic moment of the satellite is the result of magnetic moments on the main body (\bar{M}_1) and the solar array (\bar{M}_p). On the satellite's main body the magnetic moment is assumed to contain a constant residual component and an orbit rate varying component due to internal rotating devices (e.g., tape recorders). Thus the components of the magnetic moment \bar{M}_1 can be written as

$$\begin{aligned}
 M_{x1} &= M_{xo} + M_{xt} \sin(\alpha + \phi_x) \\
 M_{y1} &= M_{yo} + M_{yt} \sin(\alpha + \phi_y) \\
 M_{z1} &= M_{zo} + M_{zt} \sin(\alpha + \phi_z)
 \end{aligned} \tag{VI.18}$$

where

$$\begin{aligned}
 M_{io} &= \text{Constant magnetic moment components of the satellite} \\
 &\quad (i = x, y, z) \\
 M_{it} &= \text{Magnetic moment components of the rotating devices} \\
 \phi_i &= \text{Phase angle of the rotating magnetic moment components.}
 \end{aligned}$$

The magnetic moments of the solar array are assumed to result from the sun energizing the solar cells and producing a constant current distribution on the solar panels. Thus when the solar array is exposed to the sun, the magnetic moment \bar{M}_p can be expressed in paddle coordinates (x_h, y_h, z_h) as

$$\bar{M}_p = \begin{bmatrix} M_{xp} \\ 0 \\ 0 \end{bmatrix}$$

During eclipse, it is assumed that magnetic moments on the solar array are zero, or $\bar{M}_p = \bar{0}$.

By transforming \bar{M}_p into principal coordinates (x, y, z) and combining the results with Equation (VI.18), the following components of the total magnetic moment \bar{M} are obtained:

$$\begin{aligned} M_x &= M_{xo} + M_{xt} S(\alpha + \phi_x) + M_{xp} C\psi_p C\theta_p \\ M_y &= M_{yo} + M_{yt} S(\alpha + \phi_y) + M_{xp} S\psi_p \\ M_z &= M_{zo} + M_{zt} S(\alpha + \phi_z) - M_{xp} C\psi_p S\theta_p \end{aligned} \quad (\text{VI.19})$$

The magnetic torque \bar{T}_m is obtained by substituting Equations (VI.17) and (VI.19) into (VI.16) and by performing the cross product operation. By accounting for the paddle angle relation of Equation (VI.5), the resulting expression of the magnetic torque becomes

$$\bar{T}_m = \begin{bmatrix} T_{mx} \\ T_{my} \\ T_{mz} \end{bmatrix} \quad (\text{VI.20})$$

where

Case I:

$$\begin{aligned} \frac{T_{mx}}{M_e/r_o^3} &= \left\{ M_{yo} + M_{yt} S(\alpha+\phi_y) \right\} \cdot \left\{ 2C\epsilon_o S\theta_i S\alpha - [(1+C\theta_i) S(\alpha-\mu) \right. \\ &\quad \left. - (1-C\theta_i) S(\alpha+\mu)] S\epsilon_o \right\} + \left\{ M_{zo} + M_{zt} S(\alpha+\phi_z) - M_{xp} \alpha \right\} \\ &\quad \cdot \left\{ C\epsilon_o C\theta_i + S\epsilon_o S\theta_i C\mu \right\} \end{aligned}$$

$$\begin{aligned} \frac{T_{my}}{M_e/r_o^3} &= \left\{ M_{zo} + M_{zt} S(\alpha+\phi_z) - M_{xp} \alpha \right\} \cdot \left\{ C\epsilon_o S\theta_i \alpha \right. \\ &\quad \left. - \frac{1}{2} [(1+C\theta_i) C(\alpha-\mu) - (1-C\theta_i) C(\alpha+\mu)] S\epsilon_o \right\} \\ &\quad - \left\{ M_{xo} + M_{xt} S(\alpha+\phi_x) - M_{xp} S\alpha \right\} \\ &\quad \cdot \left\{ 2C\epsilon_o S\theta_i S\alpha - [(1+C\theta_i) S(\alpha-\mu) - (1-C\theta_i) S(\alpha+\mu)] S\epsilon_o \right\} \end{aligned}$$

$$\begin{aligned} \frac{T_{mz}}{M_e/r_o^3} &= - \left\{ M_{xo} + M_{xt} S(\alpha+\phi_x) - M_{xp} S\alpha \right\} \cdot \left\{ C\epsilon_o C\theta_i + S\epsilon_o S\theta_i C\mu \right\} \\ &\quad - \left\{ M_{yo} + M_{yt} S(\alpha+\phi_y) \right\} \cdot \left\{ C\epsilon_o S\theta_i \alpha \right. \\ &\quad \left. - \frac{1}{2} [(1+C\theta_i) C(\alpha-\mu) - (1-C\theta_i) C(\alpha+\mu)] S\epsilon_o \right\} \end{aligned}$$

Case II:

$$\begin{aligned} \frac{T_{mx}}{M_e/r_o^3} &= \left\{ M_{yo} + M_{yt} S(\alpha+\phi_y) - M_{xp} \right\} \cdot \left\{ 2C\epsilon_o S\theta_1 S\alpha \right. \\ &\quad \left. - [(1+C\theta_1) S(\alpha-\mu) - (1-C\theta_1) S(\alpha+\mu)] S\epsilon_o \right\} \\ &\quad + \left\{ M_{zo} + M_{zt} S(\alpha+\phi_z) \right\} \cdot \left\{ C\epsilon_o C\theta_1 + S\epsilon_o S\theta_1 C\mu \right\} \end{aligned}$$

$$\begin{aligned} \frac{T_{my}}{M_e/r_o^3} &= \left\{ M_{zo} + M_{zt} S(\alpha+\phi_z) \right\} \cdot \left\{ C\epsilon_o S\theta_1 \alpha \right. \\ &\quad \left. - \frac{1}{2} [(1+C\theta_1) C(\alpha-\mu) - (1-C\theta_1) C(\alpha+\mu)] S\epsilon_o \right\} \\ &\quad - \left\{ M_{xo} + M_{xt} S(\alpha+\phi_x) \right\} \cdot \left\{ 2C\epsilon_o S\theta_1 S\alpha \right. \\ &\quad \left. - S\epsilon_o [(1+C\theta_1) S(\alpha-\mu) - (1-C\theta_1) S(\alpha+\mu)] \right\} \end{aligned}$$

$$\begin{aligned} \frac{T_{mz}}{M_e/r_o^3} &= - \left\{ M_{xo} + M_{xt} S(\alpha+\phi_x) \right\} \cdot \left\{ C\epsilon_o C\theta_1 + S\epsilon_o S\theta_1 C\mu \right\} \\ &\quad - \left\{ M_{yo} + M_{yt} S(\alpha+\phi_y) - M_{xy} \right\} \cdot \left\{ C\epsilon_o S\theta_1 C\alpha \right. \\ &\quad \left. - \frac{1}{2} [(1+C\theta_1) C(\alpha-\mu) - (1-C\theta_1) C(\alpha+\mu)] S\epsilon_o \right\} \end{aligned}$$

In evaluating the magnetic torques, it was noted that the torque components are functions of two time varying parameters, α and μ . Thus Equation (VI.20) was expanded about α and μ to express the magnetic torques in the desired form of Equation (VI.6). In the expansion process, torque terms affected by the magnetic moment on the solar array were modified by the coefficients in Equation (VI.9) to account for the nulling effects during eclipse. The resulting expressions of the magnetic torque were then evaluated for the parameters listed in Table VI-1.

Tables VI-4 and VI-5 summarize the results of the evaluation for the two cases considered. It is evident that large magnetic torques at zero frequency and orbital harmonics are present about the pitch axis. Torques about the roll and yaw axes are especially pronounced at orbital frequency. The differences in the magnetic torques between the two cases are mainly due to the magnetic moment of the solar array and its orientation relative to the satellite.

Frequency ω_k	Magnetic Torques ($\times 10^{-6}$ ft-lb)					
	Roll		Pitch		Yaw	
	A_{kx}	B_{kx}	A_{ky}	B_{ky}	A_{kz}	B_{kz}
0	3.1	--	16.7	--	1.6	--
ω_e	-1.7	-.61	0	0	-1.7	.30
$\omega_o - \omega_e$	-.51	-1.7	1.5	1.7	.86	1.9
ω_o	0	17.6	-11.3	-17.6	8.8	0
$\omega_o + \omega_e$	-.51	1.7	-1.5	-1.7	-.86	1.9
$2\omega_o - 2\omega_e$	0	0	.22	0	0	0
$2\omega_o - \omega_e$	-.19	.30	1.65	0	-.15	.57
$2\omega_o$	-3.1	-3.1	-27.2	0	1.6	-1.6
$2\omega_o + \omega_e$	-.80	-.30	-1.65	0	.15	.25
$2\omega_o + 2\omega_e$	0	0	-.22	0	0	0
$3\omega_o - \omega_e$.17	0	.26	0	0	-.35
$3\omega_o$	0	0	-4.8	0	0	0
$3\omega_o + \omega_e$.17	0	-.26	0	0	-.35

Table VI-4. Summary of Magnetic Torque (Case I: Sun in Orbit Plane)

Frequency ω_k	Magnetic Torques ($\times 10^{-6}$ ft-lb)					
	Roll		Pitch		Yaw	
	A_{kx}	B_{kx}	A_{ky}	B_{ky}	A_{kz}	B_{kz}
0	3.1	--	4.6	--	-1.6	--
ω_e	1.7	.61	0	.30	-1.7	.30
$\omega_o - \omega_e$.30	3.7	-.86	1.7	-1.4	0
ω_o	0	-35.4	8.8	-17.7	17.7	0
$\omega_o + \omega_e$.30	-3.1	.86	-1.7	2.0	.30
$2\omega_o - 2\omega_e$	0	0	.15	-.46	0	0
$2\omega_o - \omega_e$.30	-.30	0	0	.15	.15
$2\omega_o$	-3.1	3.1	-1.6	4.6	-1.6	-1.6
$2\omega_o + \omega_e$	-.30	.30	0	0	-.15	-.15
$2\omega_o + 2\omega_e$	0	0	-.15	.46	0	0
$3\omega_o - \omega_e$	0	0	0	0	0	0
$3\omega_o$	0	0	0	0	0	0
$3\omega_o + \omega_e$	0	0	0	0	0	0

Table VI-5. Summary of Magnetic Torques (Case II: Sun Normal to Orbit Plane)

6. Misalignment Torques

Nominally the control axes are aligned with the principal axes of inertia of the satellite with the solar array removed. In this way, the inertia matrix of the satellite contains no products of inertias other than those due to the rotating solar array. However, if there are misalignments of the control axes from the principal axes, as represented in Equation (VI.2), the inertia matrix \bar{J}_1 about the control axes becomes

$$\bar{J}_1 = \begin{bmatrix} 1 & \psi_g & -\theta_g \\ -\psi_g & 1 & \phi_g \\ \theta_g & -\phi_g & 1 \end{bmatrix}' \begin{bmatrix} J_{xx1} & -J_{xy1} & -J_{xz1} \\ -J_{yx1} & J_{yy1} & -J_{yz1} \\ -J_{zx1} & -J_{zy1} & J_{zz1} \end{bmatrix} \begin{bmatrix} 1 & \psi_g & -\theta_g \\ -\psi_g & 1 & \phi_g \\ \theta_g & -\phi_g & 1 \end{bmatrix} \quad (\text{VI.21})$$

where

J_{iil} = Moment of inertia about the i -th principal axis
($i = x, y, z$)

J_{ijl} = Products of inertia of the solar array ($i \neq j$,
 $i = x, y, z$)

and the prime denotes the matrix transpose operation. Neglecting small inertia contributions from the solar array, the products of inertia of \bar{J}_1 are

$$\begin{aligned} J_{xy} &= J_{yx} = -\psi_g (J_{xx1} - J_{yy1}) \\ J_{xz} &= J_{zx} = -\theta_g (J_{zz1} - J_{xx1}) \\ J_{yz} &= J_{zy} = -\phi_g (J_{yy1} - J_{zz1}) \end{aligned} \quad (\text{VI.22})$$

The small angle equations of motion for SAGS indicate that inertia products add a constant gravity torque on the satellite. Reproduced from the SAGS First Quarterly Report (Reference 1), the gravity torque \bar{T}_g is written

$$\bar{T}_g = \begin{bmatrix} 4 J_{yz} \\ -3 J_{xz} \\ - J_{xy} \end{bmatrix} \quad (\text{VI.23})$$

Substituting Equations (VI.22) into (VI.23) yields

$$\bar{T}_g = \begin{bmatrix} -4\phi_g (J_{yy1} - J_{zz1}) \\ 3\theta_g (J_{zz1} - J_{xx1}) \\ \psi_g (J_{xx1} - J_{yy1}) \end{bmatrix} \quad (\text{VI.24})$$

Thus the roll, pitch, and yaw components of \bar{T}_g are proportional to the small offset angles ϕ_g , θ_g , and ψ_g , respectively.

In evaluating the gravity torques, it is assumed that prior to boom extension there is a 2 degree misalignment in the roll and pitch control axes and a 5 degree misalignment in the yaw axis and that the boom is extended along the yaw control axis. Thus for the inertias listed in Table VI-1, the magnitudes of \bar{T}_g are evaluated and presented in Table VI-6. Note that the control axis misalignments result in a relatively large torque about the roll axis.

Frequency ω_k	Misalignment Torque ($\times 10^{-6}$ ft-lb)		
	Roll	Pitch	Yaw
Case I: 0	18.4	8.3	.9
Case II: 0	24.7	7.5	0

Table VI-6. Summary of Torques Due to Control Axes/Principal Axes Misalignment

7. Eccentricity Torques

An earth-oriented satellite in a non-circular orbit has a non-uniform nominal angular velocity. As a result, a time-varying torque is induced on the satellite. In this case the magnitude of the gravity gradient torques is also affected by altitude variations. However, for slightly elliptic orbits, the torque due to the latter effect is much less significant than torques due to variations in the orbit rate.

For small eccentricities, Reference VI-5 has shown that the time varying orbit rate ω_p can be approximated as

$$\omega_p \cong \omega_o [1 + 2\epsilon C(\alpha - \lambda_p)]$$

where

ϵ = Orbital eccentricity

λ_p = Angle from ascending node to perigee.

By substituting ω_p for ω_o in the derivation of the equations of motion for SAGS, the eccentricity torque \bar{T}_e can be determined to be

$$\bar{T}_e = \begin{bmatrix} T_{ex} \\ T_{ey} \\ T_{ez} \end{bmatrix} \quad (VI.25)$$

where

$$T_{ex} = 2\epsilon \omega_o^2 J_{xy1} S(\alpha - \lambda_p) + 16\epsilon \omega_o^2 J_{yz1} C(\alpha - \lambda_p)$$

$$T_{ey} = -2\epsilon \omega_o^2 J_{yy1} S(\alpha - \lambda_p) - 12\epsilon \omega_o^2 J_{xz1} C(\alpha - \lambda_p)$$

$$T_{ez} = 2\epsilon \omega_o^2 J_{yz1} S(\alpha - \lambda_p) - 4\epsilon \omega_o^2 J_{xy1} C(\alpha - \lambda_p)$$

To obtain a conservative measure of the eccentricity torque, products of inertia resulting from control axes/principal axes misalignment are assumed. Table VI-7 lists the resulting magnitudes of \bar{T}_e which were based on an orbital eccentricity of 1 percent and the misalignment offsets assumed in the preceding section ($\phi_g = \theta_g = 2^\circ$; $\psi_g = 5^\circ$). It is evident that eccentricity effects are greatest about the pitch axis because of the relatively large value of the pitch inertia, J_{yy1} .

Frequency ω_k	Eccentricity Torque ($\times 10^{-6}$ ft-lb)					
	Roll		Pitch		Yaw	
	A_{kx}	B_{kx}	A_{ky}	B_{ky}	A_{kz}	B_{kz}
Case I: ω_o	.74	.02	.33	25.7	.04	.09
Case II: ω_o	.40	0	.30	26.0	0	.05

Table VI-7. Summary of Torques Due to Orbital Eccentricity ($\lambda_p = 0$)

LIST OF SYMBOLS

J_{iil}	Principal moment of inertia of the satellite about the i -th axis ($i = x, y, z$)
J_{ijl}	Product of inertia of the satellite ($i \neq j$; $i, j = x, y, z$)
ϕ, θ, ψ	Roll, pitch and yaw attitude error angles
ϕ_g, θ_g, ψ_g	Roll, pitch and yaw control axes/principal axes misalignment angles
β	Angle measured from autumnal equinox to line of ascending nodes
α	Orbit angle measured from line of nodes to satellite position
λ_p	Angle from line of nodes to perigee
θ_i	Orbital inclination
θ_e	Eclipse half-cone angle
ϵ_o	Angle between geographic and geomagnetic north pole of dipole model
ϵ	Orbital eccentricity
ω_o	Satellite orbit rate
ω_e	Earth's spin rate

M_e	Magnetic dipole moment of earth
r_o	Radius of orbit
$\vec{\mu}_s$	Sun vector directed from earth to sun
t	Time
V_s	Solar pressure constant
M_{io}	Constant magnetic moment components of satellite ($i = x, y, z$)
M_{it}	Orbital frequency components of magnetic moments ($i = x, y, z$)
M_{xp}	Magnetic moment of solar array
ϕ_i	Phase angle for magnetic moments of rotating devices ($i = x, y, z$)
r_c	Radius of control box
r_r	Radius of sensory ring
r_t	Radius of tip mass
l_c	Length of control box
l_r	Length of sensory ring
l_t	Length of tip mass

A_p	Area of single solar panel
l_b	Boom length
d_b	Boom diameter
t_b	Boom thickness
v_b	Reflectivity constant of boom
v_c	Reflectivity constant of control box
v_r	Reflectivity constant of sensory ring
v_t	Reflectivity constant of tip mass
v_p	Reflectivity constant of solar panel
M_c	Mass of control box
M_r	Mass of sensory ring
M_t	Tip mass
M_p	Mass of single solar panel
m_g	Mass of gimbaled reaction wheel
K	In-plane thermal bending coefficient of boom
K^*	Out-of-plane thermal bending coefficient of boom
T_d	Disturbance torque

ψ_p Hinge angle of solar array

θ_p Paddle angle of solar array

REFERENCES

- VI-1. J. L. Palmer, "Dynamic Equations for the Generalized Spacecraft Simulation," TFW Interim Technical Report 8427-6004-RU000, 1 February 1965.
- VI-2. R. J. McElvain, "Effects of Solar Radiation Pressure on Satellite Attitude Control," Guidance and Control (Progress in Aeronautics and Astronautics, Vol. 8), Academic Press, New York, 1962.
- VI-3. G. S. Reiter, C. P. Rubin, R. N. Schreiner, "Thermal Bending of Gravity Gradient Booms," TFW Technical Report 9840-6007-KU000, 30 December 1964.
- VI-4. P. C. Wheeler, "Magnetic Attitude Control of Rigid, Axially Symmetric, Spinning Satellites in Circular Earth Orbits," NASA Contractor Report CR-313, October 1965.
- VI-5. A. E. Sabroff, "A Summary of Gravity Gradient Stabilization of Earth Satellites," TFW Technical Report 9990-6715-RU001, 27 July 1964.

APPENDIX VII
IMPLEMENTATION EVALUATIONS

A. INTRODUCTION

This appendix describes the implementation feasibility study of the Semi-Active Gravity Gradient System (SAGS). These investigations have evolved a detailed preliminary design of a control mechanism utilizing the SAGS concept. The resulting controller provides semi-active roll/yaw and active pitch attitude control. Roll/yaw control is achieved by operating the pitch reaction wheel with a momentum bias and by gimbaling the wheel and coupling it to the vehicle through an energy removal mechanism which provides roll and yaw damping. Active pitch control is accomplished by controlling the wheel speed about its bias level. A conical-scan horizon sensor provides pitch attitude information.

The SAGS controller assembly physically combines the reaction wheel, the horizon sensor and an energy removal mechanism (damper) into a single mechanical unit which is gimballed via a torsional flexure suspension (Figure VII-1). The development of a single mechanical unit performing all of these functions has, of course, required a great deal of attention to functional interface problems; for example, mounting the scanner optics in the reaction wheel motor imposes definite constraints upon the motor configuration and where in the spacecraft this assembly can be located. These interactions are emphasized in the following discussion.

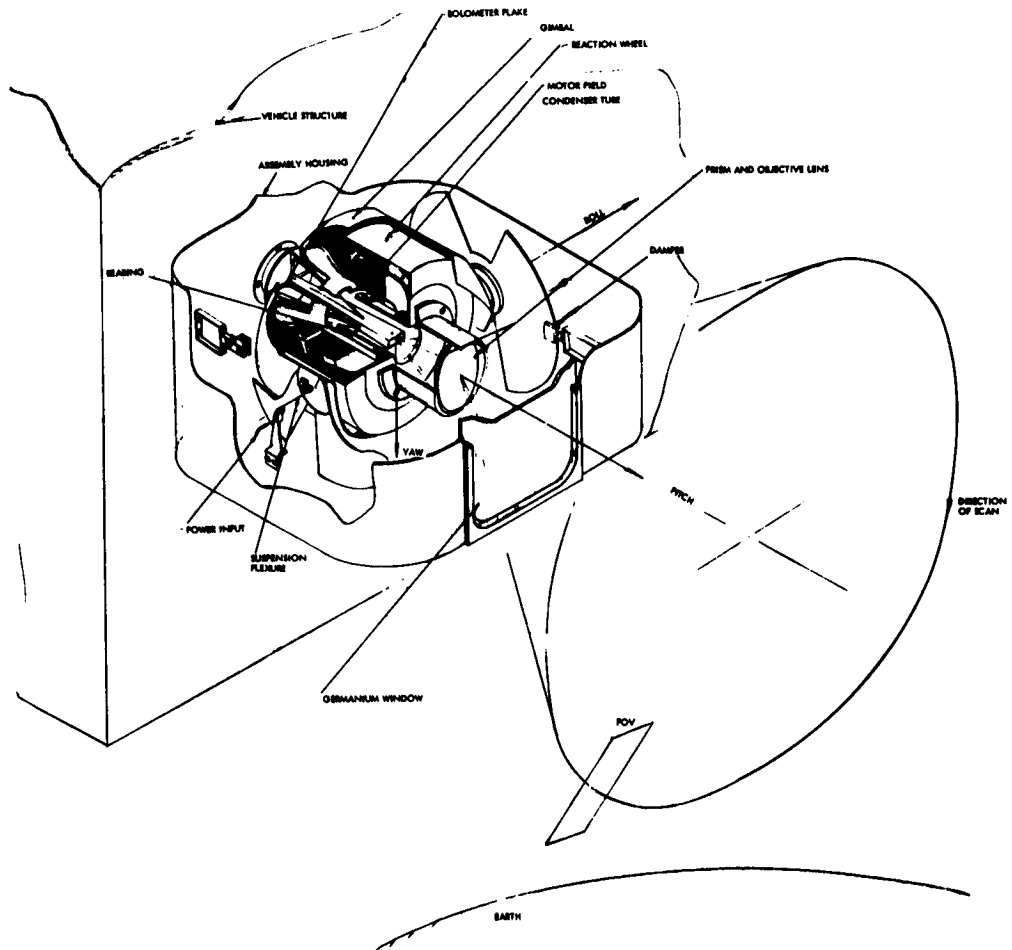


Figure VII-1 Conceptual View of SAGS Controller

The baseline configuration developed during this study is unique in that a portion of the optical system is mounted in the gimballed wheel assembly while the remainder (e.g., the bolometer flake) is affixed to the stationary case of the assembly; this approach permits optical (rather than electrical) transmission of the unprocessed error information through the gimbal system.* The wheel assembly itself is suspended from the stationary outer case via a pair of torsion wires which also serve as transmission paths for motor power. An appropriate passive caging mechanism is provided to protect the wheel assembly and its suspension during periods of abnormal excitation. Damping is afforded in the baseline design by the mechanism of magnetic hysteresis; an alternate (heavier) eddy current damper is also described. Figure VII-1 is a conceptual view of the control mechanism.

B. DESIGN SUMMARY

The controller design study presented herein was undertaken to establish mechanization feasibility and estimates of power consumption and system weight. Detailed optimization of the various mechanical components was not attempted. Furthermore, details such as circuit design were not considered inasmuch as the implementation feasibility is related primarily to the mechanical components.

The following design objectives were established:

- The controller was to physically combine the reaction wheel, the horizon sensor and the energy removal mechanism (damper) into a single mechanical unit.

* A more conventional design, with the bolometer mounted in the gimballed wheel assembly, is also presented.

- The reaction wheel was to operate at nominal speed of 1500 rpm. The reaction wheel was to have a controllable speed range of ± 500 rpm about the nominal speed. Furthermore, the reaction wheel motor acceleration or deceleration torques were to be approximately constant over the 1000 to 2000 rpm speed range.
- The horizon scanner was to be designed so as to produce reasonable levels of power input to its bolometer flake and an acceptable signal-to-noise ratio.
- The gimballed suspension was to be designed to provide a proportional spring restraint torque. A caging mechanism was required to protect the gimballed equipment.
- The design of the controller was required to permit sizable gimbal excursions (e.g., 30°).

Based upon the analytic and simulator studies presented in this report, the following parameter values were established as baseline design goals:

- Wheel bias momentum: 3.0 ft-lb-sec
- Motor torque: 5.0 in-oz
- Torsional spring constant: 10^{-4} to 10^{-3} ft-lb/rad
- Proportional damper coefficient: * 1.5 ft-lb per rad/sec
- Gimbal freedom: ± 40 deg

*This applies to the eddy current damper only. Hysteresis damper characteristics (e.g., the shape of the torque/position curve) were not established during this study. However, this lack of information had little effect upon implementation studies since the size and weight of the hysteresis damper do not depend significantly upon the desired performance characteristics.

All these objectives were fulfilled by the designs indicated in Figures VII-2 and VII-3. These configurations differ primarily in the earth horizon sensor configuration and the damping mechanism (hysteresis in Figure VII-2 and eddy current in Figure VII-3). The horizon sensing systems differ in the location of the infrared sensing element; the design of Figure VII-2 attaches the earth energy sensing element (condenser tube and bolometer flake) to the main housing while that of Figure VII-3 features an immersed bolometer mounted in the gimballed wheel assembly. These particular configurations resulted from detailed consideration of the incoming radiance energy and the desire to eliminate any mechanical restraint which might occur with cabling through the suspension.

The leads which might otherwise be required to transmit power to the motor have been eliminated by utilizing the torsion wires in this capacity. This approach compromises the flexure design somewhat in terms of the strain energy margin and the spring constant. Both configurations use a beryllium-copper flexure which produces suitable small spring constants and an acceptably large strain fatigue margin, while providing adequate power transmission characteristics. In addition to the gimbal stops, ring snubbers are provided to limit vibrational excitation of the torsion wires during boost.

The salient characteristics of the control assembly are summarized in the following table. Detailed design considerations are presented in the following sections of this appendix.

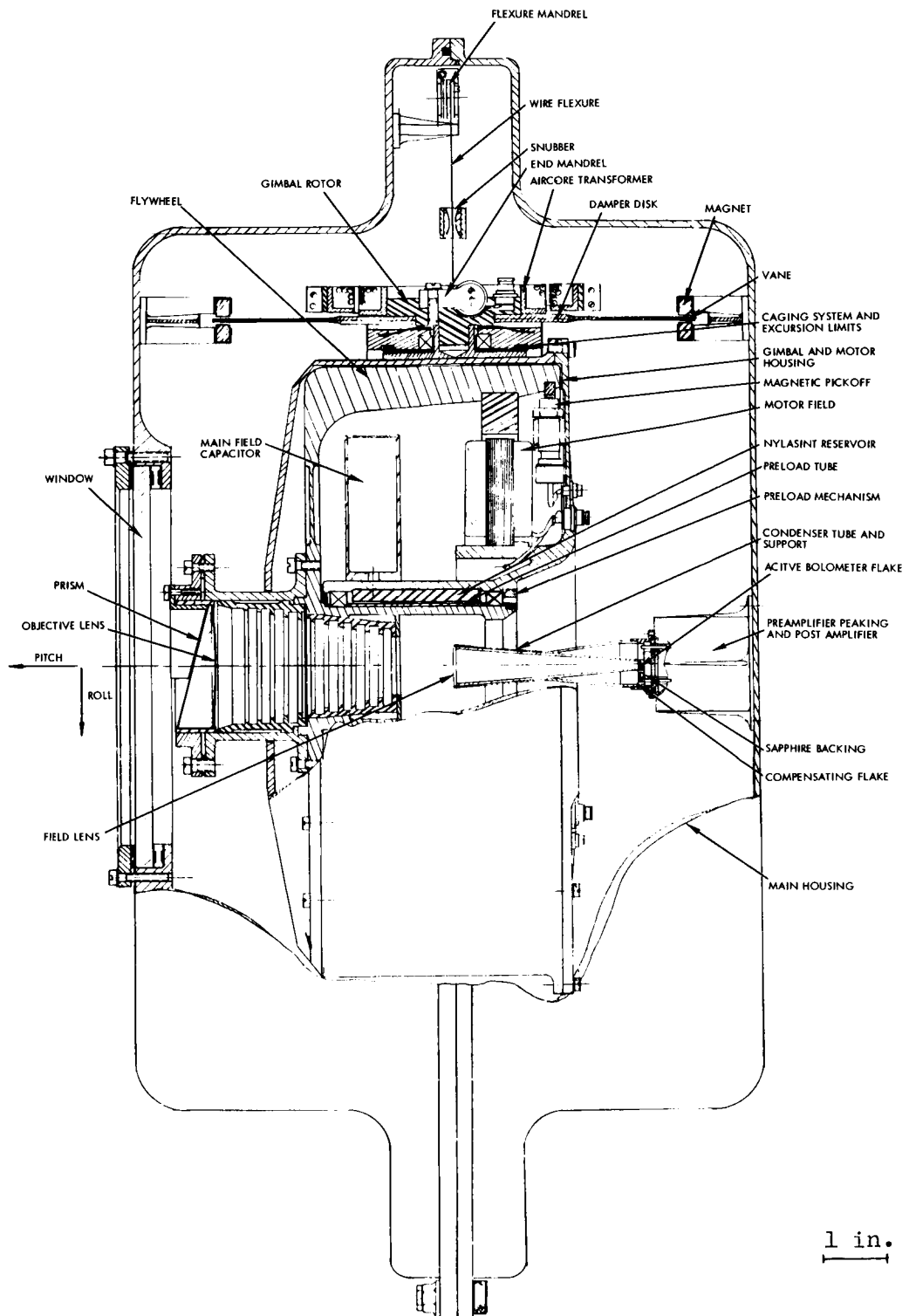


Figure VII-2 Controller Design with Hysteresis Damper and Case-Mounted Bolometer

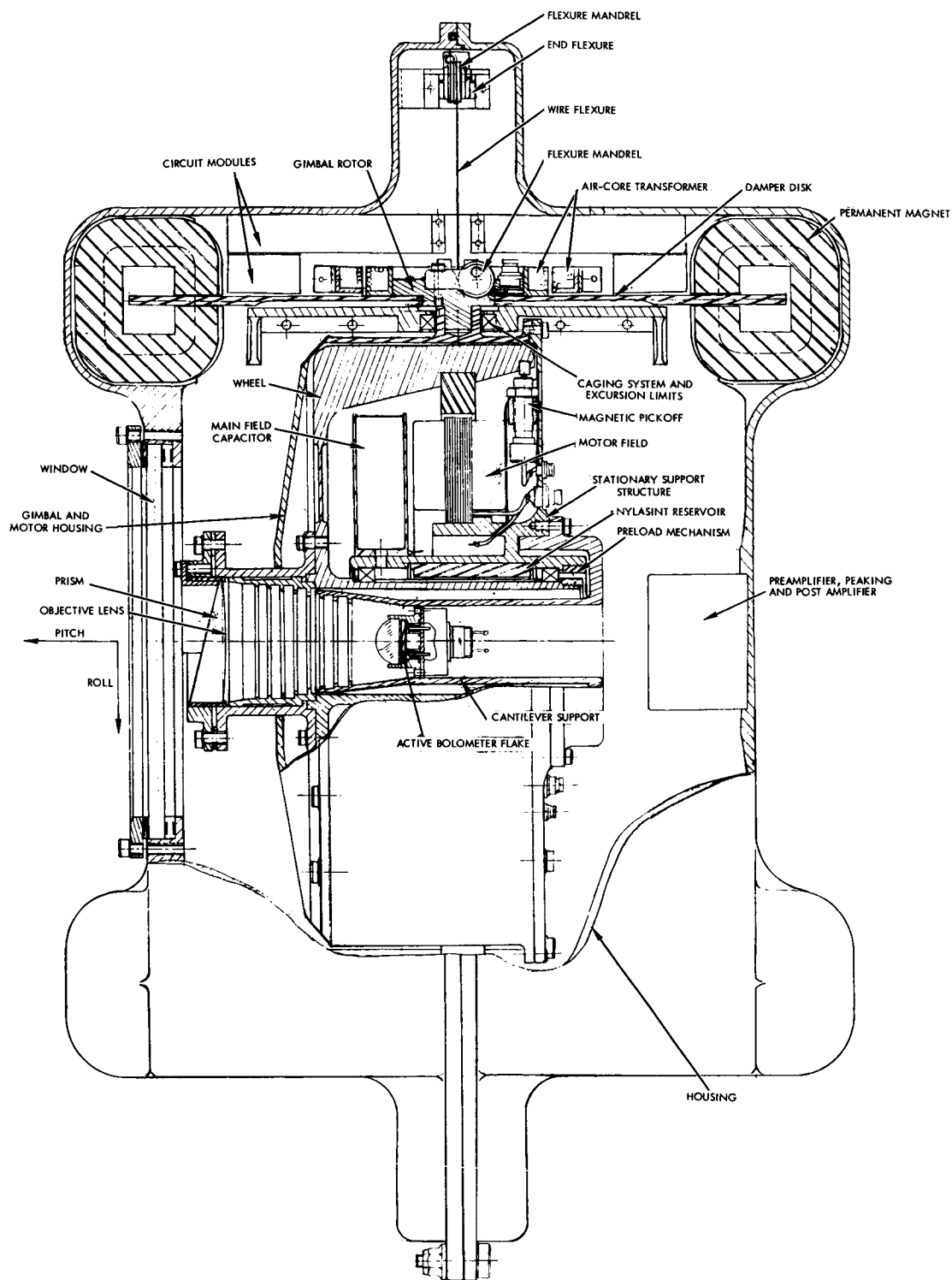


Figure VII-3 Controller Design with Eddy Current Damper and Wheel-Mounted Bolometer

Performance Characteristic	Value
<u>Power Consumption</u>	
Motor Power:	
Maximum	32 watts
Nominal	5 watts
Control Circuitry:	
Maximum	14 watts
Nominal	9 watts
<u>Controller Dimensions</u>	13" x 10" x 10"
<u>Controller Weight</u>	
Eddy Current Mechanical Configuration (Total)	28.5 lbs
Hysteresis Mechanical Configuration (Total)	22.5 lbs
Housing (including window)	8 lbs
Electronics	4 lbs
<u>Reaction Wheel Characteristics</u>	
Nominal Torque	5.5 in-oz
Nominal Momentum	3 ft-lb-sec
Controllable Speed Range	1500 \pm 500 rpm
<u>Horizon Scanner Characteristics</u>	
Bolometer input power:	
Immersed Bolometer	9.4×10^{-6} watts
Condenser tube and flake	5.05×10^{-6} watts
<u>Gimbal Characteristics</u>	
Moments of Inertia	
I _x	.0265 slug-ft ²
I _y	.043 slug-ft ²
I _z	.027 slug-ft ²

Table VII-1 Summary of Controller Performance Characteristics

C. MOTOR/REACTION WHEEL DESIGN

The motor assembly employed in this design is an inside-out, two-phase (400 ~), induction machine, with the squirrel cage rotor assembled as part of the rotating inertia wheel. Single-phase, on-off power is provided (via the torsion wire suspension) as demanded by the control electronics, with the necessary phase-shifting provided by two capacitors, one in series and the other shunting the winding; the minimum voltage-pulse duration is 50 milliseconds. A channel (with the axis of wheel rotation as its centerline) is provided through the motor/wheel assembly; elements of the horizon sensing system are mounted in this space.

The reaction wheel is constructed almost entirely of aluminum alloy materials.* The two thin section ultra-precision radial bearings are of symmetrical deep groove design with one integral shield facing outwards towards the sides of the assembly. Alternate balls are slightly undersized and serve as idler type spacers for the load carrying balls. Such a design tends to reduce the internal sliding friction. The bearing friction is estimated at 0.5 oz-in. Each bearing is rated at 680 lb load capacity and a life of over 5 years at the expected speeds. The bearing size was dictated by the horizon scanner dimensions. For other horizon scanner assembly configurations (for example as indicated in Figure VII-3) smaller diameter bearings can be selected. Axial preload of the bearings is accomplished as shown in Figure VII-2 to prevent vibration impacts. Bearings are normally oil lubricated, with lubricant retention within the bearing promoted by a porous Nylasint oil reservoir

*This use of aluminum alloy (rather than stainless steel) in the rotor of the wheel does not represent an optimum design. The aluminum alloy rotor in the present design is explained in the footnote of page 43 (Volume I).

(which tends to equalize the oil vapor partial pressure within the assembly). The wheel itself is so designed that when in a severe vibration environment it deflects sufficiently to gap the existing clearance space between the outer wheel surface and the gimbal structure, thus limiting the load transmission to the shaft and bearings. The stationary parts are as light as they can be made while retaining the ability to support the wheel and the stator assembly with good design margin. They also provide a heat sink surface to remove heat from the unit by radiation to the controller housing.

Table VII-2 summarizes the performance characteristics of the motor assembly shown in Figures VII-2 and VII-3.

Motor Characteristic	Value
Torque level:	
• Acceleration torque at 1000 rpm	6 in-oz
• Acceleration torque at 2000 rpm	4.5 in-oz
• Deceleration torque at 1000 rpm	6 in-oz
• Deceleration torque at 2000 rpm	6 in-oz
Power Consumption:	
• Power required for continuous acceleration (1000 to 2000 rpm)	28 watts
• Power required for continuous deceleration (2000 to 1000 rpm)	32 watts
• Average power required to maintain bias speed (1500 rpm)	5 watts
Wheel momentum at 1500 rpm	3 ft-lb-sec
Friction and windage at 1500 rpm	1 in-oz
Synchronous speed	2500 rpm
Weight (including wheel-mounted optical components)	14 lb

Table VII-2 Reaction Wheel Motor Characteristics

D. SUSPENSION SYSTEM AND HOUSING DESIGN

The controller housing shown in Figures VII-2 and VII-3 is a two-piece aluminum webbed structure, the interior of which is filled with helium to a pressure of 0.15 atmosphere. The necessary scanner field of view is afforded by a large (6" x 8") germanium window; an "O" ring seal insures pressure maintenance. The housing as designed weighs 8 lbs (including the window). A reduction of approximately 3 lbs can be achieved by using magnesium, but at the expense of fabrication simplicity.

The suspension system serves to support the gimballed wheel assembly in the housing and, further, to provide the required torsional spring restraint and the necessary transmission paths for motor power. This assembly must also protect itself (and the suspended wheel assembly) from damage during periods of abnormal excitation (e.g., boost), and must be compatible with the damping mechanism. These design requirements have been met by evolving a suspension system consisting of a gimbal caging mechanism and torsion wire flexures.

1. Caging Mechanism

The controller has two caging mechanisms symmetrically located on each side of the gimbal. Each mechanism (Figure VII-4) consists of rotational and axial stops, one stationary support member, a rotor, a wave spring, a set of finger springs, and a bearing.

The combined rotational and axial stops are attached to the gimbal. The rotation of the gimbal is limited (to $\pm 35^\circ$) by the

protruding arc sectors when in contact with the end of the radial recess in the stationary support member. A surface protected with anodized aluminum is provided to absorb the shocks associated with limiting.

The axial translation induced by shock and vibration is checked by both the finger springs and the flat portion of the rotational stop. The axial clearances between the finger springs and the rotor (.007") and between the stationary member and the rotational stop (.015") and are such that the spring action will occur prior to the hard stop.

Lateral displacements are limited by the relatively wide but thin wave spring. Here again the shock and vibrational energies will be partially dissipated by the contact friction occurring between the inner lobes of the wave spring and the gimbal shaft (with which it is always in contact), and between the outer lobes and the inner bearing race. The approximate clearance between the bearing and the lobes of the spring is .020". This, as well as the axial clearances, was chosen to allow normal operation of the system when its transverse (pitch and yaw) rotations do not exceed 0.25 degrees of arc. This angular displacement is approximately twice the transverse rotations expected under normal operating conditions. It is well to note that the choice of clearances greatly influences the design of the flexures.

During in-orbit operation the bearing has no effect upon the performance of the controller. However, during ground handling and boost the bearing action is desirable.

For ease of assembly the rotor may be detached from the gimbal shaft (Figure VII-2). Notice that the rotor provides support for the damper disc, the flexure mandrel, the electrical power connector and the air-core transformer.

2. Wire Flexure Mechanism

The wire flexure mechanism is shown on Figure VII-4. It consists of two identical torsion wires 3 inches in length with a diameter of 0.013 in. The wire material chosen is 3/4 HT highly heated treated beryllium-copper alloy. This choice of material represents a compromise between the desirability of high stress capabilities and low electrical resistivity, inasmuch as the flexures transmit power to the gimballed motor. The proposed method of attachment for each flexure is to wrap the wire around a mandrel and fix it to a retaining screw. This method of attachment allows utilization of approximately 80% of the yield stress for the purposes of the preload if so desired. End flexures (cantilever springs) provide for attachment of the outboard ends of each torsion wire and the means to apply preload to the wire. The end flexures must be fairly pliant to assure that as the wheel assembly is displaced during handling, or as the wire length changes due to the thermal cycling, the load on the torsion wire remains relatively constant.

The significant characteristic of the flexure wire suspension is its lateral stiffness. Its importance lies in the effects it has on the weight and/or performance of the damping mechanism (see Section E) and the caging mechanism design. For these reasons this

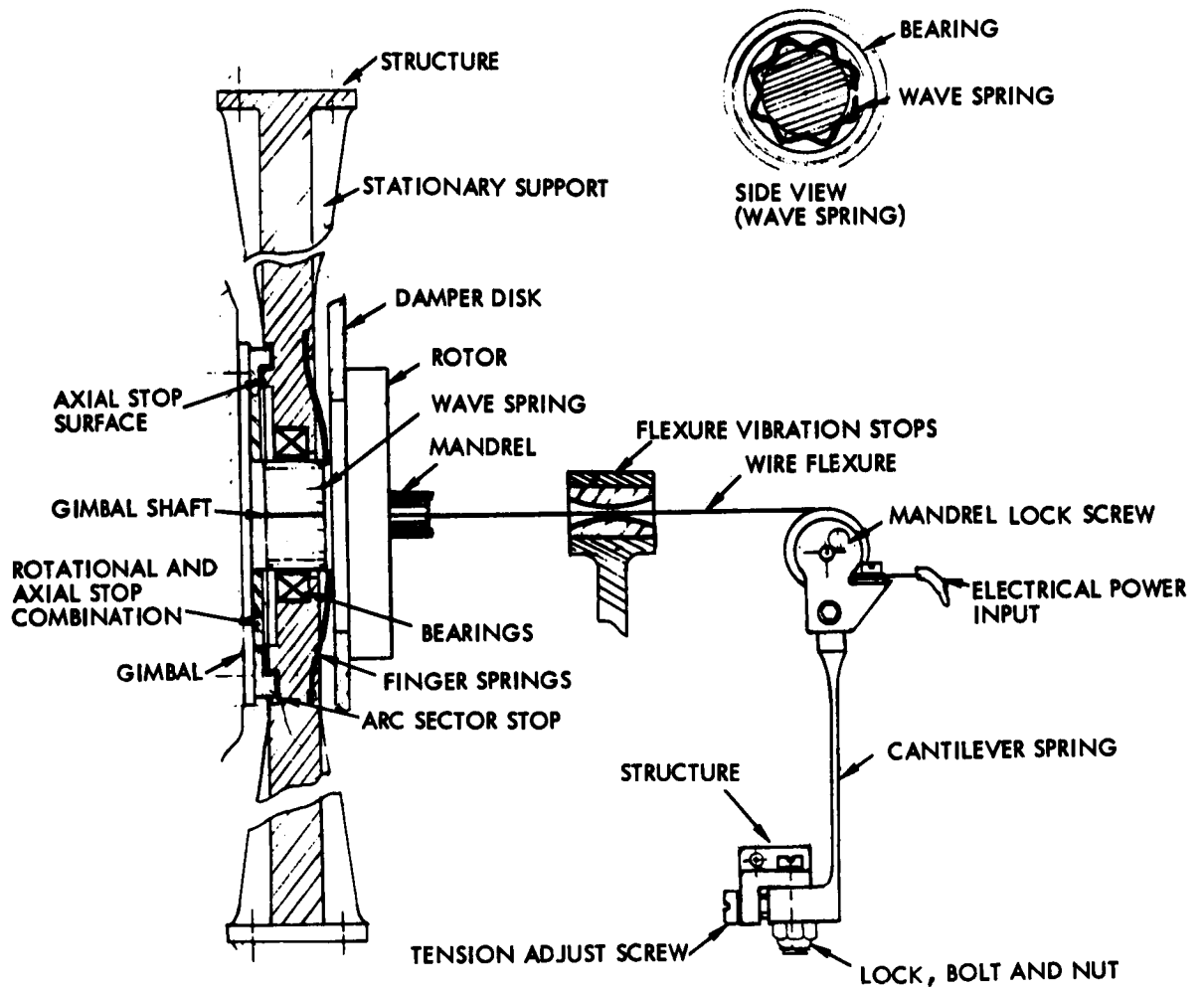


Figure VII-4 Suspension System

particular design is intended to achieve highest possible transverse stiffness without impairing the reasonable stress margin allowance from the viewpoint of wire fatigue.

a. Flexure Analysis

The choice of the physical characteristics of the torsional spring flexure is based on the analytical evaluation summarized in Table VIII-3. It appears that the dominant design constraint is the requirement to transmit power to the reaction wheel. The first choice for the spring material was that of the highly heat-treated 302 alloy steel. This steel is characterized by high ultimate strength and the high stress value of its elastic limit (280,000 psi). Stress evaluation produced a fatigue stress margin allowance of approximately 2.6 when not confronted with electrical power transmission. However, a simple thermal analysis indicated this flexure's inability to carry current. Its surface temperature could not be exactly determined because of the large variation of resistivity with temperature but was approximated to within a region of 130 to 190°F rise.

The beryllium-copper flexure exhibits a fatigue margin of approximately 1.92, somewhat less than that of the steel alloy. However, for the problem at hand, the beryllium alloy is far superior to the previous choice inasmuch as it can satisfy all of the imposed constraints. The indicated thermal analysis assumes no heat transfer from the wire by conduction or convection. This may not be a completely valid assumption and one may imply slight conservatism of the results.

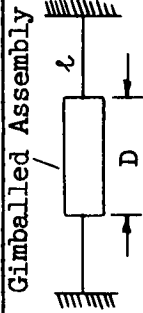
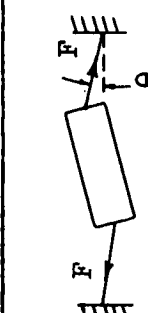
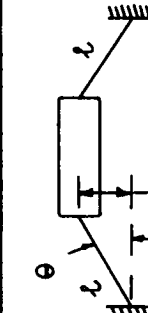
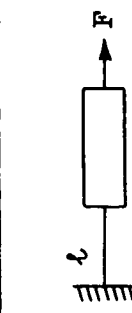
Description	Model	Expression	Remarks
Wire diameter (d)		$K_{TT} l \frac{1}{4}$ $d = 2 \left(\frac{l}{\pi G} \right) = 0.013 \text{ in.}$	K_{TT} = Torsional spring const. K_{TT} = 1.2×10^{-2} lb-in/rad G = Shear modulus = 6.5×10^6 psi l = Spring length = 3.0 inch
Transverse Rotational stiffness, K_{TR}		$K_{TR} = DF(1 + D/2l)$ $= 250 \text{ lb-in/rad}$	F = Preload = 8.0 lbs D = Length stiff member = 11.0 inches
Transverse Translation stiffness, K_{TT}		$\frac{F}{\Delta} = K_{TT} = \frac{2F}{l}$ $= \frac{16}{3} = \frac{5.3 \text{ lbs}}{\text{inch}}$	$\Delta = \frac{\theta}{l}$
Axial Stiffness		$K_A = \frac{EA}{l} = \frac{740}{l} \text{ lbs/in.}$	A = Cross-section of flexure = 1.31×10^{-4} in ² E = Young's modulus = 17×10^6 psi

Table VII-3

SUMMARY OF WIRE FLEXURE ANALYSIS

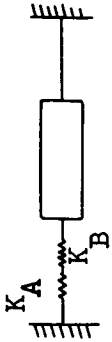
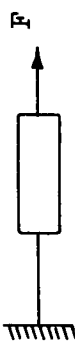
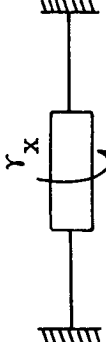

Description	Model	Expression	Remarks
Equivalent Axial stiffness with cantilever beam, K_{Ae}		$K_{Ae} = \frac{K_A K_B}{K_A + K_B}$ $= 88.0 \frac{\text{lb}}{\text{in.}}$	$K_B = 100 \text{ lb/in}$ = Cantilever beam const.
Axial stress due to preload F, σ_A		$\sigma_A = \frac{F}{A} = 61,000 \text{ psi}$	
Torsional stress, σ_T		$\sigma_T = \frac{d}{2} \frac{G \gamma_x}{l}$ $= 9,900 \text{ psi}$	$\gamma_x = \text{Flexure defl.}$ $\leq .7 \text{ rad}$
Expected stress due to temperature variation $\Delta T = 880^\circ, \sigma_{\Delta T}$		$\sigma_{\Delta T} = \frac{\alpha \Delta T K_{Ae}}{A}$ $= 1600 \text{ psi}$	$\alpha = 9.2 \times 10^{-6} \text{ (in/in)/}^\circ\text{F}$

Table VII-3 (Cont'd)

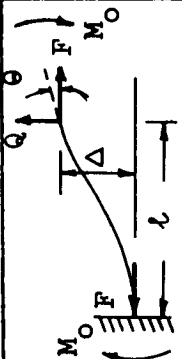

Description	Model	Expression	Remarks
Expected stress due to axial deflections allowed in the caging mechanism	—	$\sigma_{\delta} = \frac{\delta K A \epsilon}{A}$ $= 10,000 \text{ psi}$	δ = Max. axial deflection = 15×10^{-3} inches
Stress due to bending		$\sigma_B = \frac{M_0 d}{2I} \approx \frac{F \delta d}{2\lambda I}$ $= 850 \text{ psi}$	Approx. holds for $l \lambda \gg 10$ $\lambda = \left(\frac{F}{EI}\right)^{1/2} = 12.9$ $I = \frac{\pi d^4}{32} = 2.82 \times 10^{-9}$ θ = Transverse rotational angle $= 4.36 \times 10^{-3}$ radians
Power dissipation of wire	—	$P_W = I_W^2 R$ $= \left(\frac{P_M}{V_M (PF)}\right)^2 \frac{\rho l}{A}$ $= 2.23 \times 10^{-2} \text{ watts}$	P_M = Power to motor = 30 watts V_M = Voltage input to motor = 120 volts (PF) = Power factor = .5 ρ = Resistivity = 3.9×10^{-6} ohm-in
Heat Flow in wire		$\dot{Q} = 3.1416 P_W$ $= 0.076 \frac{\text{BTU}}{\text{hr}}$	

Table VII-3 (Cont'd)

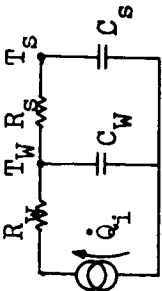
Description	Model	Expression	Remarks
Resistance to heat flow of surroundings (due to heat transfer by radiation)	<p>Heat Transfer Model</p>  <p> $C_S \gg C_W$ $C_S \rightarrow \infty$ $R_W \approx 0$ </p>	$\frac{\Delta T_F}{QR} = \left[\frac{4K_{SB} \epsilon \left(\frac{T_S + T_W}{2} \right)^3}{A_{SW}} \right]^{-1} \frac{(HR)(\text{O}^\circ\text{F})}{\text{BTU}}$ $R_S = 180 \frac{(HR)(\text{O}^\circ\text{F})}{\text{BTU}}$	$K_{SB} = 1.73 \times 10^{-9} \text{ BTU/FT}^2 \times \text{HR}(\text{deg R})$ $\epsilon = \text{Emissivity} = .8$ $T_S = \text{Temperature of surroundings} = 100^\circ\text{F}$ $T_W = \text{Surface temperature of wire} = 120^\circ\text{F}$ $A_{SW} = \text{Surface area of wire} = 8.5 \times 10^4 \text{ ft}^2$
Heat Capacitance of wire, C_W	$R C_S \dot{T}_W + T_W = QR_S + T_S$ $(\Delta T)_W = T_W - T_S$	$C_W = C_P W = 11.7 \times 10^{-6} \frac{\text{BTU}}{\text{LB}}$ $W = \text{Weight of wire} = .117 \times 10^{-3} \text{ lbs}$	$C_P = \text{Specific heat} = .1 \frac{\text{BTU}}{\text{lb}^\circ\text{F}}$ $W = \text{Weight of wire} = .117 \times 10^{-3} \text{ lbs}$
Wire temperature rise, ΔT_W		$\Delta T_W = QR_S [1 - e^{-t/\tau}] (\text{O}^\circ\text{F})$ $= 13.7 [1 - e^{-.132t}] (\text{O}^\circ\text{F})$ $\Delta T_{MAX} = 13.7^\circ\text{F}$	$\tau = C_W R = 7.6 \text{ sec}$ $t = \text{time (sec)}$

Table VII-3 (Cont'd)

Of interest is the relation of the flexure spring constant and its temperature rise due to current flow. It appears that the flexure spring constant is roughly inversely proportional to the temperature (ΔT_w) rise. Therefore, a design giving an order of magnitude decrease in the torsional spring constant would result in a wire temperature rise of 130^oF. For this reason the maximum spring constant specified in the performance analyses has been chosen here.

b. Alternate Approaches

In view of the stringent suspension requirements, electro-magnetic and magnetic suspensions systems were not considered. Investigated, however, were various types of mechanical flexures. In particular, blade type flexures and a TRW-designed compensating flexure were evaluated. A summary of this work is given in Table VII-4 in terms of a comparison between blade and wire flexures.

E. DAMPER DESIGN CONSIDERATIONS

Three types of damping systems were considered: a magnetic hysteresis, an eddy current, and (very briefly) a simple viscous fluid damper.

The magnetic hysteresis damper consists of two pairs of permanent magnet assemblies and a magnetic vane (Figure VII-2). Each such assembly is symmetrically located on two sides of the gimbal axis. A determination of the performance of the SAGS control system with a hysteresis damper was not completed during this study.

Item	Wire	Blade
Overall Simplicity	Very simple	Relatively complex
Fabrication	No special processes	Protection of blade during assembly and special machine processes are required.
Spring constant adjustment	Simple	Difficult
Environmental capabilities	Good	Good
Electrical transmission	Simple	Complex
Caging protection	Can be protected	Difficult to protect against tension load
Translational stiffness	Depends on pre-load; is generally less than blade stiffness	Good for small rotations
Angular displacement	Large displacements are achievable	Normally limited to small displacements

Table VII-4 Wire and Blade Comparison

Therefore, the hysteresis damping system was sized by determining the damper torque level required to remove the same amount of energy per gimbal oscillation cycle as removed by a proportional damper with a damping coefficient of 1.5 ft-lb per rad/sec; a sinusoidal oscillation of $\pm 5^\circ$ at orbital frequency was assumed. This resulted in a hysteresis damper torque requirement of approximately 10^{-4} ft-lb. The damper consists of ALNICO VIII magnets with an outer pole piece and an inner pole piece both made of Armico iron.

The vane consists of a sector of an annulus with an outer radius of 3.65 inches and an inner radius of 3.45 inches and a thickness of 3×10^{-3} inches. The vane material is 3.5% chrome steel. The vane is supported by an aluminum (or any other non-magnetic material) structure concentric with the axis of the gimbal. The magnet assemblies straddle the vane with a .060 inch spacing between the magnets and the vane. The production of the required damping torque occurs as a result of local magnetization polarity changes from north to south and back to north in the vane element as it moves relative to the magnets. A conceptual configuration of the hysteresis damper is shown on Figure VII-5. The weight of the actual damper components is negligible. However, the extremely small dimensions of the vane require reasonable structural support. The weight of the supporting structure is approximately 1.2 lbs.*

An alternate damping mechanism is employed in the controller design of Figure VII-3. Two identical eddy current damper assemblies are located symmetrically with respect to the gimbal axis. Each assembly is comprised of two magnetic sources, fabricated from CAST-ALNICO 5-7 (chosen for its very high "BH" product), and a copper disc or vane. The area of each pole piece is 0.75 inch^2 . The shape of each magnet is that of a circular sector subtending an angle of 17.5° . The center of each pole piece is located 4.0 inches from the gimbal axis. The thickness of the disc and the width of the gap are 0.123 in. and 0.170 in., respectively, with a disc

*The detailed design of the damper will be affected significantly not only by the torque level required, but by the shape desired for the hysteresis characteristic (a factor which has not been determined). However, the weight of the unit will be essentially independent of these detailed aspects of the design.

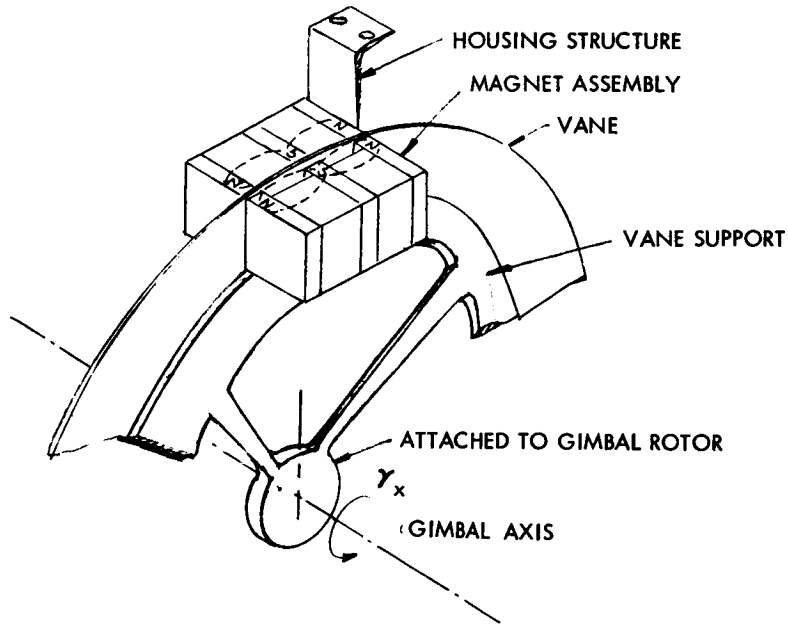


Figure VII-5 Conceptual View of Hysteresis Damper

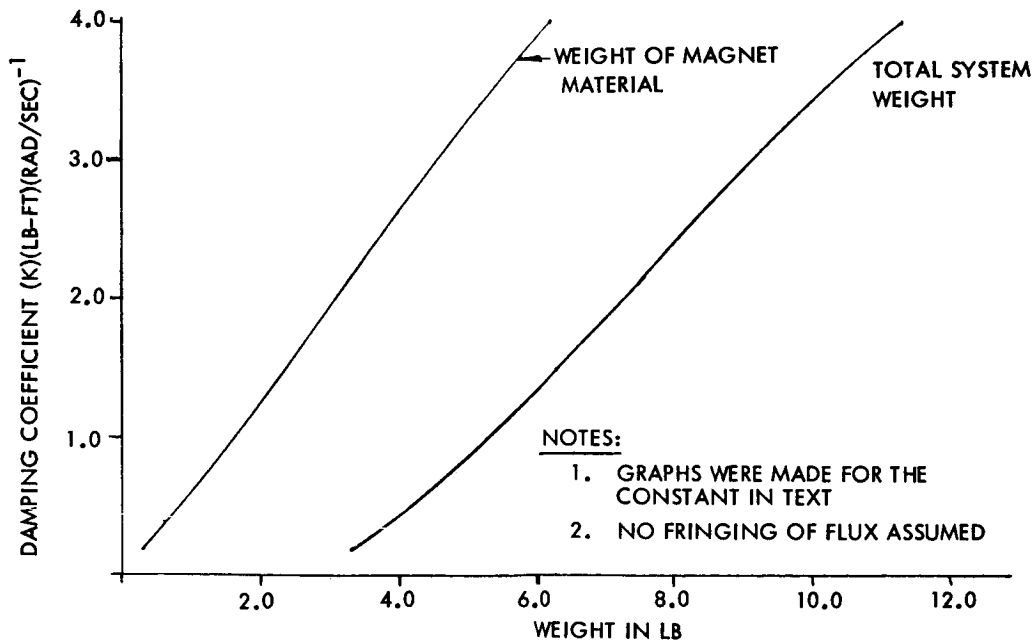


Figure VII-6 Eddy Current Damper Weight as a Function of Damping Coefficient

diameter of 10 inches. The weight of the damping system (with an assumed 45% magnetic flux fringing) is 7.4 lbs; with fringing neglected the weight of the damper becomes 6.3 lbs. At first glance it would appear that a weight penalty is incurred by the choice of copper for the vane material; however, the use of copper results in smaller pole pieces than would be required with, for example, aluminum. As a matter of fact an aluminum disc would require a 40% increase in the size of the poles for maintenance of the same level of performance.

The shape of the pole piece area has only a slight effect on the damping constant. This may be observed by inspection of the torque expressions given in Table VII-5 for circular sector, rectangular, and circular pole shapes. The advantage of the circular sector pole piece is that, for a given disc diameter, one can locate a larger pole area at a longer distance from the center of the disc.

The permissible air gap width is a function of the outer diameter of the gimballed assembly, the diameter of the conducting disc and the transverse rotational motion of the gimbal. Note that the air gap has an important influence upon the length of the permanent magnet pole pieces and thus upon the total weight of the damping mechanism. Figure VII-6 shows the relation of the damping constant and the weight of damper system, with the distance from the gimbal axis to the center of each pole piece fixed at four inches.*

*It should be noted that the primary advantage of the eddy current damper (indeed, of any proportional velocity-dependent damper) is the analytic predictability of its performance. SAGS performance characteristics with proportional damping have been established in detail during this study.

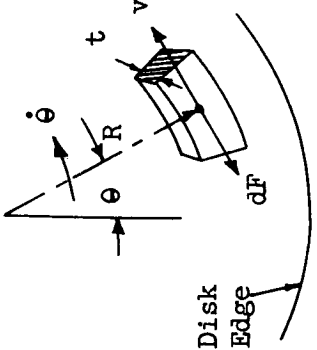
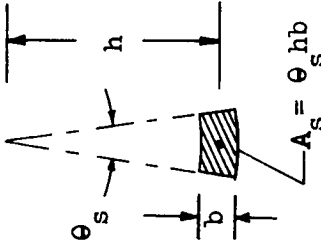
Item	Model	Expression	Remarks
Torque on conductor volume element	 <p>Disk Edge</p> <p>(\vec{B} into page)</p>	$dF = \frac{B^2 \dot{\theta} t R^3 dR \theta}{G \rho}$ $= \frac{B^2 \dot{\theta} t R^3 dR \theta}{2.2}$ <p>B=1.11 webers/m² t=Thickness of disk =3.13x10⁻³m ρ=1.75x10⁻⁸ Ohm-meters T=Newton-meters</p>	See Ref. VII-1, G is a shape factor and depends on the path of the eddy currents. Its approximate value is .91π if the disk edge is no closer to the pole piece than twice the diagonal of the pole.
Torque on conductor (circular sector pole piece)	 <p>$A_s = \theta_s h b$</p>	$T = \frac{B^2 \dot{\theta} A_s h^2}{\rho} \left[\frac{1}{2.2} + \frac{1}{8} \left(\frac{b}{h} \right)^2 \right]$	

Table VII-5

SUMMARY OF DAMPER SYSTEM ANALYSIS

Item	Model	Expression	Remarks
Torque on conductor, (rectangular pole piece)	—	$T = \frac{B_s^2 \theta t A_s h^2}{\rho} \left[\frac{1}{2.2} + \frac{1}{24} \left(\frac{b}{h} \right)^2 \right]$ <p>$A_s = ba$, a = width</p>	
Torque on conductor (circular pole piece)	—	$T = \frac{B_s^2 \theta t A_s h^2}{\rho} \left\{ \frac{1}{2.2} + \left(\frac{b}{h} \right) \left[\frac{1}{32} \left(\frac{b}{h} \right) - \frac{2}{3\pi} \right] \right\}$	
Area of one pole piece	—	$A_s = \theta h b = \left(\frac{2.2 \text{ c.p.}}{\text{th } B_s} \right) (39.3)^2$ <p>= .75 inch²</p>	<p>c = .51 (Newton-meter) / (rad/sec)</p> <p>h = 10.2 x 10⁻² m = 4 inch</p> <p>t = 3.13 x 10⁻³ m = .123 inch</p> <p>$\theta_s = 17.5^\circ$</p> <p>b = .612</p>
Length of magnet	—	$l_m = \frac{B_s}{\mu H} = .074 \text{ m} = 2.9 \text{ inch}$ <p>Considering fringing</p> $l'_m = (2.9)(1.45) = 4.27 \text{ inch}$	<p>$\delta = 4.32 \text{ meters} \times 10^{-3}$</p> <p>= .170 inch</p> <p>H = 650 x 10³ praerstedts</p> <p>$\mu = 10^{-7}$</p>

Table VII-5 (Cont'd)

A third damping mechanism considered is that of viscous (fluid) shear. The envisioned fluid viscous damper is a unit consisting of a 2.4 in radius disc rotating in a viscous fluid. The fluid is contained within a cylindrical assembly attached to the housing and the disc is attached to the gimbal rotor. The necessary clearance between the shaft and the cylindrical container wall is .02" for a 0.7 inch gimbal rotor diameter. The interior width of the assembly is essentially equal to the air gap of the eddy current damper (≈ 0.17 in.). The weight of the unit including the fluid is approximately 3.0 lbs (for a damping coefficient of 1.5 ft-lb per rad/sec) so that from the viewpoint of weight the fluid damper is preferable to the eddy current mechanization. However, the viscous damper is incompatible with the suspension concept utilized in this design study owing to the clearances ($\approx .02$ ") required by lateral deflections of the gimballed reaction wheel assembly. Even with labyrinth seals excessive leakage will occur. Calculations indicate that under the best of circumstances the leakage mass rate is approximately 1 gram in 14.3 days. This means that the damper cavities would be empty in approximately 1.3 years. Unless a shaft seal can be adopted this fluid damper must be discarded from consideration for this application.

An alternate fluid damping configuration might be one in which the entire gimballed reaction wheel is "floated" in its housing. However, this concept still requires seals where the horizon sensor telescope (which is rotating) protrudes from the motor case. Moreover, the fluid employed in such a device must have good transmission characteristics in the wavelengths employed by the horizon sensor. Finally, the weight of the required fluid could be excessive (e.g., 4 lbs).

F. HORIZON SENSING SYSTEM DESIGN

The horizon sensing system employed for both controller designs utilizes the conical scan configuration. The scan cone angle (σ) chosen is 50 degrees based upon the orbital altitude and the vehicle configuration chosen (see SAGS First Quarterly Report). The instantaneous field of view is 14.1° by 3.5° , and the prism angle is 12.8° . Associated with the sensing system is a bolometer detector which senses the difference between the radiance of the earth and space. The indicated attitude error depends upon where in the scan cycle the earth radiation pulse (if any) occurs, as indicated by the four reference pulses generated by the magnetic pickoff. Either "sin θ " or "sin 2θ " processing is possible with the available information. Notice that pitch attitude error information is available only when the scan cone intersects the earth. The present system provides pitch information for roll errors well in excess of those encountered during fine control.

The optical prism is directly attached to the rotating reaction wheel. The bolometer can be either a part of the gimballed wheel assembly (Figure VII-3) or may be attached to the stationary portion of the unit (Figure VII-2). In either case it is desirable for the bolometer to collect the incoming energy from all parts of the objective lens even though the latter can be off the optical axis (e.g., by 10° to 20°) due to gimbal deflections (in the configuration of Figure VII-2).

Two optical systems have been developed in this study; both utilize an optical window, scanning prism, and an objective lens, all made of germanium. The configurations differ primarily in the

location of the sensing element; in one case (Figure VII-2) it is mounted on the stationary housing, while in the other (Figure VII-3) it is part of the gimballed wheel assembly. The major design constraints are the need for efficient gathering of the incoming radiant energy and the desire for no torque restraint due to sensor electrical leads.

1. The Cone Channel Sensing System

A key feature of the configuration of Figure VII-2 is the energy collection cone, which permits "bending" of the optical axis. Such conical radiation channels have been exploited for some time (Reference VII-2). The tube used for energy transmission (which has a rectangular cross-section) may be fabricated from metal stock or by electro-forming (depending upon the tube dimensions). The inner surface of the cone is coated with a material possessing a high degree of reflectivity at the wavelengths of interest. The principal advantages of such a tube is its simplicity, its non-image forming characteristic, and the resulting uniform distribution of energy over the surface of the detector placed at the exit of the tube. Furthermore, a well designed detector tube has a response that is essentially uniform for a wide range of entrance angles, thus permitting a significant "bend" in the optical axis (at the cone entrance). Analyses indicate that gimbal deflections of 20° decrease the efficiency of this optical system by less than five percent. Since a 17° deviation of the optical axis (wheel spin axis) from the orbit plane normal is sufficient to remove the scan cone from the earth, the above range is certainly more than adequate.

The design of the cone is fully discussed in Reference VII-2 and for this discussion it is sufficient to note the design results. From Figure VII-2 it may be noted that the objective lens concentrates the incoming energy onto a field lens at the entrance of the tube. The focal length and the diameter of the objective lens are 3.6 and 1.87 inches respectively. The field lens focal length is also 3.6 inches. The height and the width of the tube entrance are designed to result in FOV angles of 14.1° and 3.46° , when coupled with the prism gain of 2.4. Hence, the height (parallel to the roll axis) is 0.406 inches and the width is 0.106 inches. The exit of the tube ideally requires a bolometer flake which is 2.50 mm by .675 mm. (Based upon discussions with the Barnes Engineering Company, it appears that such a unit can be obtained on special order.) The time constant of such a bolometer flake may be expected to be on the order of 1.1 milliseconds and its responsivity is $100 \frac{\text{volts} \cdot *}{\text{watts}}$.

Of considerable interest is the optical efficiency of this unique horizon sensing system, and the resulting power presented to the bolometer flake.

The radiance N for a 200°K earth within the CO_2 band (14.5 to 16 microns) is:

$$N = 2.02 \times 10^{-4} \frac{\text{watts}}{\text{cm}^2 \text{ steradian}}$$

*The reference flake is provided to allow nulling (via a bridge circuit) of such environmental effects as the ambient temperature.

The irradiance is

$$H = N \Omega = (2.02 \times 10^{-4})(1.49) \times 10^{-2} = 3.01 \times 10^{-6} \frac{\text{watts}}{\text{cm}^2}$$

where Ω is the solid angle formed by the effective field of view of the cone channel. The power input to the system (prior to any attenuation) is:

$$P = HA (3.01 \times 10^{-6})(18.3) = 55 \times 10^{-6} \text{ watts}$$

where A is the area of the objective lens in square centimeters.

The energy transmission efficiency is

$$\xi_T = (W)(OB)(P)(F_1)(F_2)(T)(FI) = .092$$

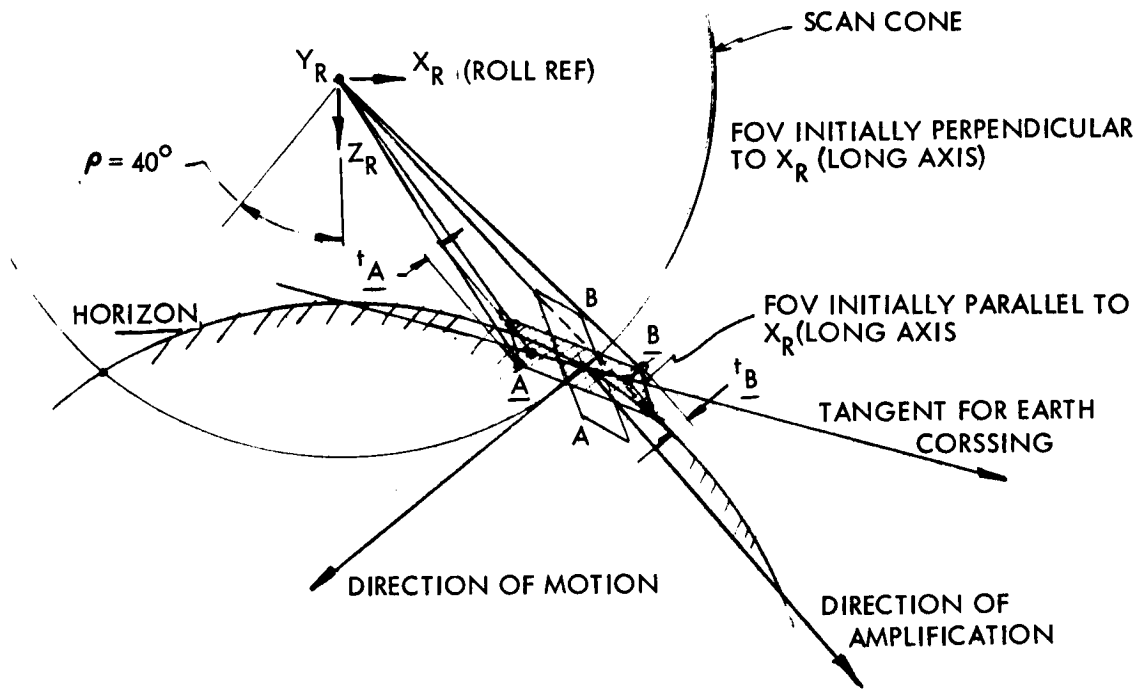
where

- W = (window efficiency) = .9
- OB = (obliquity factor) = .47
- P = (prism efficiency) = .9
- F₁ = (objective lens efficiency) = .9
- F₂ = (field lens efficiency) = .9
- T = (tube efficiency) = .6
- FI = (filter loss) = .5

Hence, the power transmitted to the flake is

$$P_f = P\xi_T = (55 \times 10^{-6})(.092) = 5.05 \times 10^{-6} \text{ watts}$$

Basing the frequency band on a null crossing time of $.19 \times 10^{-3}$ sec (Figure VII-7) the calculated signal-to-noise ratio is approximately 225 to 1.



NOTES:

1. $t_A + t_B = 3.2^\circ \cong 0.19 \times 10^{-3} \text{ SEC}$
2. $t_A + t_B = 9.1^\circ \cong 0.55 \times 10^{-3} \text{ SEC}$

Figure VII-7 Field-of-View Geometry

2. The Immersed Bolometer Sensing System

This configuration (Figure VII-3) is more conventional than the one preceding. An immersed bolometer is located in the focal plane of objective lens and is part of the gimballed reaction wheel assembly. The lens has a focal length and a diameter of 2.7 and 1.87 inch respectively. In this system the apparent size of the bolometer flake establishes the field of view of the system. Hence, the actual bolometer flake dimensions must be approximately 2.0 mm by 0.5 mm. The time constant of such a bolometer is on the order of two milliseconds. The electrical output signal from the bolometer may be routed (after preamplification): (i) via the air core transformers; (ii) it may be frequency modulated and routed via the flexure wire and then a transformer to the signal processing circuitry, or (iii) it may be routed (prior to preamplification) via hardwires appropriately arranged to produce minimum restraint torques on the suspended assembly.*

The efficiency of this optical system is greater than that of the alternate design, resulting in a bolometer input power level of approximately 9.4×10^{-6} watts and a signal-to-noise ratio of 610 to 1.** Notice, however, that this estimate does not account for any reduction in the signal-to-noise ratio which may be introduced during transmission of the bolometer output signal to the housing. Of course, this consideration does not apply to the preceding design.

*The continuous power required for preamplification at the bolometer output could be provided, for instance, by a small battery which would be recharged from the motor input voltage.

**In both cases the signal-to-noise ratio does not include electrical effects (e.g., amplifier noise).

G. SIGNAL PROCESSING AND CONTROL ELECTRONICS

The block diagram of the necessary electronic circuitry is shown on Figure VII-8. The electronics assembly consists of three functional units; namely, (i) the sun rejection and the earth signal reconstruction circuitry, (ii) the earth pulse width discrimination and computation circuitry, and finally, (iii) the reaction wheel assembly control and drive electronics.

The sun pulse rejection and the signal reconstruction processing problem has been solved previously (for example, see Reference VII-3). Here it is sufficient to mention that the circuitry essentially ignores sun pulses via a pulse width discrimination technique and converts the earth signal to a straight-sided pulse which then can be used for computation of the vehicle attitudes. This technique eliminates the employment of sun shades and is realized by peaking out the bolometer thermal time constant prior to post amplification. Carrying the resulting broadband signal to a high level limiting stage and then applying the necessary noise limiting filter essentially ignores the sun except for those orbits where the sun pulse appears at or near the horizon. Under this condition the resulting error is still tolerable. If the clipping level E_c is made sufficiently greater than the threshold level E_T and the cutoff frequency of the low pass filter is judiciously chosen the sun pulse will never pass through the threshold detector. An appropriate choice of the ratio E_c/E_T also minimizes the effect of the delay introduced by the filter when the scan speed varies due to pitch attitude control activities.

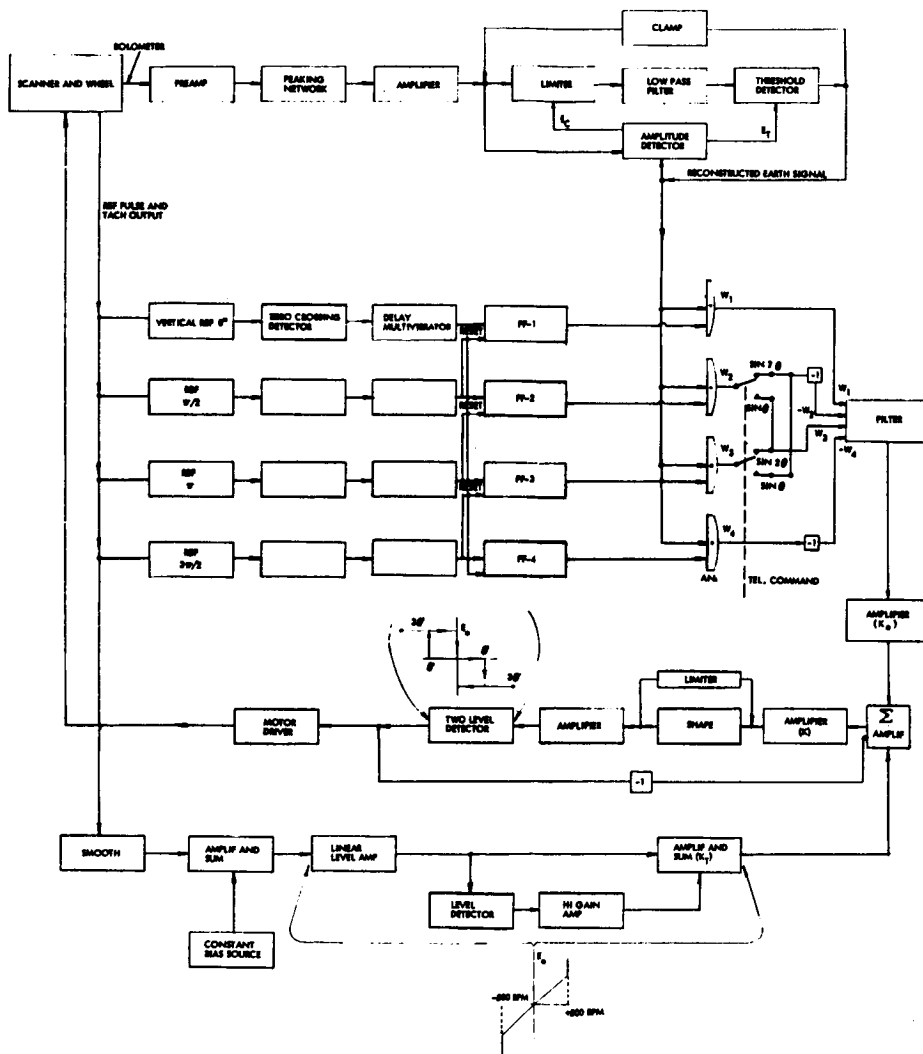


Figure VII-8 Signal Processing and Control Electronics

The indicated computation circuitry consists of reference pulse conditioning and AND" gating of these signals in conjunction with the reconstructed earth signal. This scheme allows determination of the earth pulse width (W_1) occurring in each quadrant of the scan cone. For clarity consider the case of a planar scan ($\sigma = 90^\circ$). Representing the scan locus by a unit circle, the portion of the scan cycle during which the field of view intersects the earth is represented by a circular sector of an appropriate angular width. For no pitch error this sector is bisected by a vertical reference axis, established with respect to the body of the wheel-scanner assembly by a pulse from the magnetic pickoff. Four such signals dividing the scan cone into four quadrants are available. As the vehicle rotates about the pitch axis, the earth pulse angle also rotates with respect to the vertical reference axis. The angle defining this motion relative to the reference vertical is a measure of the pitch error. Two possible processing schemes are provided: "sin2 θ " and "sin θ " processing. (Either can be selected via ground command if such a capability is desired.) For "sin θ " processing the pulse sector components of the quadrants I and II are weighed positively while those in quadrants III and IV are negatively weighed; "sin2 θ " processing is achieved by interchanging the weighting of the pulse components in quadrants II and III.

As previously mentioned the reference pulses are derived from the magnetic pickoff. The motor speed variations will result in the offsets of both the width and the position of the earth reconstructed pulse with respect to the reference. To compensate for these offsets the magnetic pickoff reference pulses are appropriately

delayed. This delay is provided by the indicated multivibrator circuits and is equal to the average of the leading and the trailing edge of the earth pulse. Because both the amplitude and the width of the pulse from the vertical reference magnetic pickoff are linearly related to the scanner speed, special care is exercised in the reference pulse circuitry. The technique chosen for minimizing the effect of magnetic pickoff waveform changes is to mechanically shorten the rotating tooth as much as possible. Electronically, the pickoff output pulse is processed by a "zero crossing detector" with built-in hysteresis. The trailing edge of the detector output always occurs at zero voltage level and, hence, is coincident with the same mechanical position of the scanner regardless of the scanner speed. This processed reference signal sets the flip-flop circuit and then is "AND" gated with the reconstructed earth pulse. Each flip flop is reset by the reference pulse occurring 90° after the one with which it was set (Figure VII-8). The resulting outputs of the "AND" gates are appropriately weighed and filtered. The pitch error signal so derived is introduced to the reaction wheel assembly control and the drive circuitry.

The reaction wheel assembly control circuitry includes a pulse modulator with a small deadband and nonlinear bias tachometer feedback loop (Figure VII-8). These elements provide pitch attitude control and inhibit the wheel speed to within the 1000 to 2000 rpm speed range selected for proper scanner operation and bias momentum maintenance. Motor speed information can be derived by processing the reference pulses used in scanner signal processing. The design and performance of the reaction wheel control system is described in detail in Appendix III.

It is anticipated that implementation of the above circuits described will involve microcircuitry with the exception of the motor driver. The weight and the nominal circuit power requirements are estimated as 4 lbs and 9 watts, respectively. Detailed circuit design is beyond the scope of the present study.

REFERENCES

- VII-1 A. D. Moore, Eddy Currents Induced in Disks," AIEE Transactions, 66, 1, 1947.
- VII-2 D. E. Williamson, "Cone Channel Condenser Optics," Journal of the Optical Society of America, 42, 10, Oct. 1952.
- VII-3 "Design Study Report for Nimbus Horizon Scanner," (Contract No. NAS 5-3696), ITHACO Inc., 1964.

"The aeronautical and space activities of the United States shall be conducted so as to contribute . . . to the expansion of human knowledge of phenomena in the atmosphere and space. The Administration shall provide for the widest practicable and appropriate dissemination of information concerning its activities and the results thereof."

—NATIONAL AERONAUTICS AND SPACE ACT OF 1958

NASA SCIENTIFIC AND TECHNICAL PUBLICATIONS

TECHNICAL REPORTS: Scientific and technical information considered important, complete, and a lasting contribution to existing knowledge.

TECHNICAL NOTES: Information less broad in scope but nevertheless of importance as a contribution to existing knowledge.

TECHNICAL MEMORANDUMS: Information receiving limited distribution because of preliminary data, security classification, or other reasons.

CONTRACTOR REPORTS: Technical information generated in connection with a NASA contract or grant and released under NASA auspices.

TECHNICAL TRANSLATIONS: Information published in a foreign language considered to merit NASA distribution in English.

SPECIAL PUBLICATIONS: Information derived from or of value to NASA activities. Publications include conference proceedings, monographs, data compilations, handbooks, sourcebooks, and special bibliographies.

TECHNOLOGY UTILIZATION PUBLICATIONS: Information on technology used by NASA that may be of particular interest in commercial and other nonaerospace applications. Publications include Tech Briefs; Technology Utilization Reports and Notes; and Technology Surveys.

Details on the availability of these publications may be obtained from:

SCIENTIFIC AND TECHNICAL INFORMATION DIVISION
NATIONAL AERONAUTICS AND SPACE ADMINISTRATION

Washington, D.C. 20546